Effects of Reflected Waves on Energy Dissipation in Breaking Waves

by

Xiaohui Zhou

Submitted to the Department of Civil and Environmental Engineering
in partial fulfillment of the requirements for the degree of

Master of Science in Civil and Environmental Engineering

at the

MASSACHUSETTS INSTITUTE OF TECHNOLOGY

May 1999

Eng.

Author.....
Department of Civil and Environmental Engineering
May 21, 1999

Certified by.....
Ole Secher Madsen
Professor, Civil and Environmental Engineering
Thesis Supervisor

Accepted by.....
Andrew J. Whittle
Chairman, Departmental Committee on Graduate Studies

Effects of Reflected Waves on Energy Dissipation in Breaking Waves

by

Xiaohui Zhou

Submitted to the Department of Civil and Environmental Engineering
on May 21, 1999, in partial fulfillment of the
requirements for the degree of
Master of Science in Civil and Environmental Engineering

Abstract

This thesis presents the results of a laboratory study of the effects of reflected waves on the energy dissipation in breaking waves. These experiments were conducted in a 28-meter-long, 76-cm-wide and 85-cm-high wave flume in the Ralph M. Parsons Laboratory at MIT. At one end of flume, a piston-type wave maker generates periodic waves normally incident on a gently sloping beach (1 on 30) with a reflective (vertical or sloping) structure located 17.8 m away from the wave maker. A wave gauge and a SonTek Acoustic Doppler Velocimeter are used to measure surface displacement and velocities, respectively, from which the incident and reflected wave characteristics are resolved. The no-structure experiments provide baseline data on incident wave energy dissipation. The vertical-wall and sloping-wall experiments are used to compare with the no-structure experiments and examine potential influence on wave energy dissipation from the presence of highly reflecting seawalls.

Through comparison of these experimental results, we conclude that the reflected wave is not affected by the seawall, i.e., the reflected waves do not appear to lose energy as they travel seaward from the seawall whether they pass through a surf zone or not on their way. The break point may not be in agreement depending on the definition of breaking criterion, but the general behavior of the first harmonic incident wave height, non-dimensionalized by the total water depth, is very similar. This non-dimensional incident wave height reaches a maximum of about 0.53 at the break point, decays rapidly immediately after breaking, then remains nearly constant at about 0.34. The initial decay distance right after breaking is tentatively adopted as 6 times the depth at breaking. This two-part decay behavior is not in agreement with the model (Brown, 1996) in which the incident wave height is assumed to vary linearly with the water depth immediately after breaking. However, the incident wave's attenuation is the same in experiments with and without a highly reflecting structure. The experiments showed remarkable agreement between the measured and the predicted wave set-up/set-down and return current (Svendsen and Jonsson, 1976). A transition region is also found between the break point and the undertow.

Thesis Supervisor: Ole Secher Madsen
Title: Professor, Department of Civil and Environmental Engineering

Acknowledgments

This research was supported by the U.S. Army Research Office (AASERT) and NOAA's Sea Grant College Program.

I am especially grateful to my advisor and mentor, Professor Ole Secher Madsen. His inspiration, advice and deep insight into the problem has always been a great help during the investigation. I would like to thank him from the bottom of my heart.

Additionally, I would like to thank other students I worked with while in the lab. Robert Meyer taught me how to run the wave maker, calibrate the wave gauge and collect raw data. Jie Yu helped me understand some aspects of the wave theories. The family of Ling Tang shared their joy and happiness with me.

Most of all, I thank my wife, Bing, for her love, encouragement and support. Without her, I could not have gone through the most difficult period of time at MIT.

Contents

List of Figures

Chapter 1

Introduction

1.1 Background

Over the past years the coasts of the United States have been devastated by several severe storms, e.g., Storm Keith in 1988, Hurricane Bob in 1991, Hurricane Bertha in 1996 and Hurricane Mitch in 1998. All of these storms have caused millions of dollars of damage to coastal properties and raised public awareness of the danger associated with storm wave attack on beaches. It was reported recently (February 1999) that President Clinton was seeking one billion dollars to fix the damage from hurricanes.

In many coastal areas people constructed coastal protection works, such as seawalls, ripraps, and breakwaters. There has existed for a long time a controversy about seawalls. On one hand, seawalls can protect valuable coastal properties and are expected to reduce beach erosion. On the other hand, the reflected waves emanating from the seawalls might dramatically alter the size and nature of the waves in the surf zone, e.g., the breaking point and energy dissipation pattern, thus influencing near-shore sediment transport, beach profile evolution and coastal erosion in the long run. These walls themselves, usually expensive to build, are often subject to severe scour at their toes that can cause

failure. The static and dynamic pressure from waves, currents and changes in water level must also be taken into account in the design of seawalls. Hence, it is of engineering importance to understand seawall-effects on near-shore sediment transport and beach erosion.

With the above motivation a laboratory experimental study of the effects of seawalls on coastal erosion was carried out at the Ralph M. Parsons Laboratory in Massachusetts Institute of Technology in 1993. The results of this study, completed in 1995 (Moody and Madsen, 1995), showed a negligible effect of seawalls on erosion in front of them including negligible scour at the toe of the seawall. These results were corroborated by the field observations of Kraus and McDougal (1996). Furthermore, Kraus and McDougal as well as McDougal et al. (1996) concluded that the long held belief that reflection of waves by the seawall was the cause of increased erosion in front of the wall appeared to be incorrect.

However, these conclusions were based on experiments in which waves were normally incident to the beach. Because waves are generally obliquely incident to a beach and generate a longshore current which is absent for the normal incidence, the above conclusion of negligible seawall-effects on erosion due to normally incident waves is of limited value. To conclusively evaluate seawall-effects, we must consider both theoretically and experimentally the conditions corresponding to obliquely incident waves. Two major factors contribute to sediment transport along beaches: one is the wave that stirs up sediments and the other is the wave-induced longshore current advecting the

sediment in the shore-parallel direction. Therefore, the understanding of hydrodynamics of waves and wave-induced longshore currents on seawall-protected beaches becomes the prerequisite to quantify longshore sediment transport. While Longuet-Higgins (1970) identified the basic equation governing wave-induced longshore currents along a gently sloping beach without reflected waves, little work appears to have been done for wave-induced longshore currents along a beach whose landward boundary consists of a reflective seawall. To develop such a model is the ultimate objective of a project currently going on at Ralph M. Parsons Laboratory. The theoretical considerations in the development of a longshore current model in the presence of a reflecting seawall are presented in section 1.2. The research reported here focuses on the effects of reflected waves on the energy dissipation in breaking waves, and should be regarded as the first step in the development of a longshore sediment transport model, which allows and accounts for the presence of reflective structures along the coastline.

1.2 Theoretical analysis

Suppose the wave motion is described by linear long wave theory and waves propagate over an infinite straight gently sloping beach with parallel bottom contours towards a shore-parallel reflective structure (seawall) located along $x = x_w$ (See Figure 1-1), the incident wave is expressed by its surface profile

$$\eta_i = a_i \cos(\psi_i - \omega t) \tag{1.1}$$

in which $a_i = a_i(x)$ is the incident wave amplitude, $\omega = 2\pi / T$ is the radian frequency, T is the wave period, and ψ_i is the phase function. ω and h are related through the dispersion relationship

$$\omega^2 = gk \tanh kh \tag{1.2}$$

where $k = k(x)$ is the local wave number and $h = h(x)$ is the local water depth. In shallow water, where $kh << 1$ and $\tanh kh \cong kh$, equation (1.2) reduces to

$$k = \frac{\omega}{\sqrt{gh}} \tag{1.3}$$

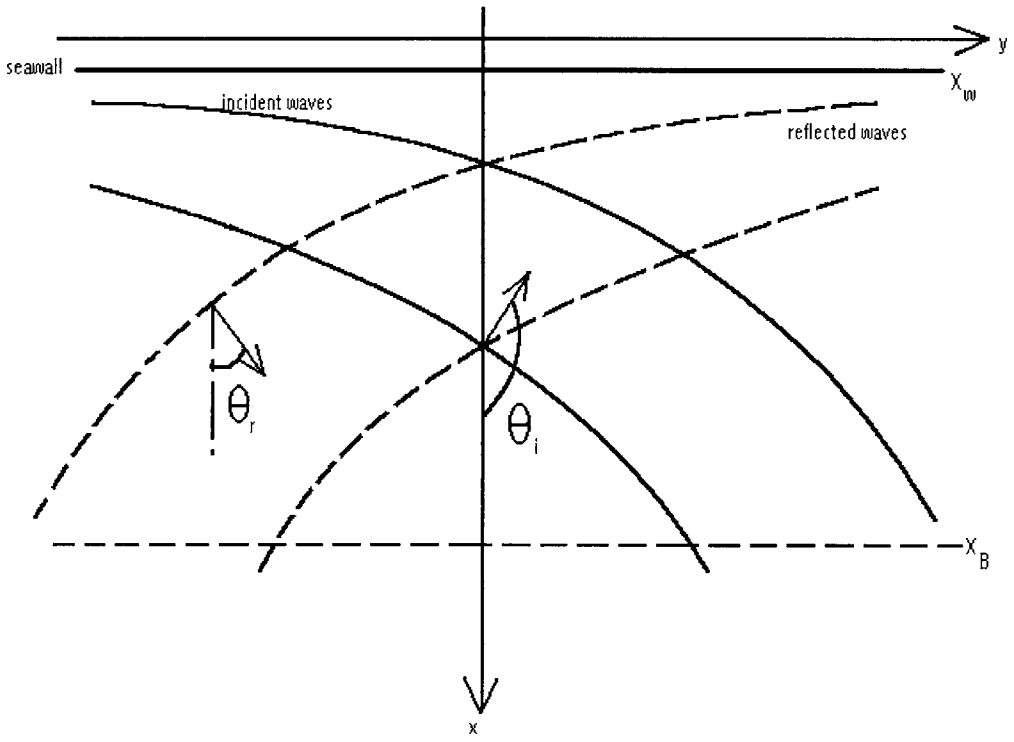

Figure 1-1 Definition for theoretical analysis

Therefore, horizontal velocity vector is expressed as

$$[u_i, v_i] = \sqrt{\frac{g}{h}}\eta_i[\cos\theta_i, \sin\theta_i] \tag{1.4}$$

and phase function is then

$$\psi_i = \int_{x_w}^{x} \frac{\omega}{\sqrt{gh}} \cos\theta_i dx + \frac{\omega}{\sqrt{gh}} \sin\theta_i y \tag{1.5}$$

where g is gravity and θ_i is the angle of incidence, measured from the x-axis and governed by Snells Law, i.e.,

$$k \sin\theta_i = \frac{\omega}{\sqrt{gh}} \sin\theta_i = const \tag{1.6}$$

The reflected wave has an angle of incidence

$$\theta_r = \pi - \theta_i \tag{1.7}$$

which immediately gives us

$$\cos\theta_r = -\cos\theta_i \,;\; \sin\theta_r = \sin\theta_i \tag{1.8}$$

The reflected wave characteristics can be written as

$$\eta_r = a_r \cos(\psi_r - \omega t) \tag{1.9}$$

and reflected horizontal velocity vector is

$$[u_r, v_r] = \sqrt{\frac{g}{h}} \eta_r [-\cos\theta_i, \sin\theta_i] \tag{1.10}$$

with the phase function

$$\psi_r = -\int_{x_w}^{x} \frac{\omega}{\sqrt{gh}} \cos\theta_i dx + \frac{\omega}{\sqrt{gh}} \sin\theta_i y + \psi_{rw} \tag{1.11}$$

in which the phase angle ψ_{rw} represents a potential phase shift associated with the wave reflection from the seawall located at $x = x_w$.

With the above expressions for the incident and reflected wave components, the shore-parallel component of the radiation stress, defined by Longuet-Higgins (1970)

$$S_{xy} = \frac{1}{T}\int_0^T dt \int_{-h}^{\eta} \rho(u_i + u_r)(v_i + v_r)dz \tag{1.12}$$

with ρ denoting the fluid density, is given by

$$S_{xy} = (S_{xy})_i + (S_{xy})_r = (S_{xy})_i(1 - R^2) \tag{1.13}$$

in which $(S_{xy})_i$ and $(S_{xy})_r$ are radiation stresses associated with the incident and reflected waves, respectively, and $R = R(x) = a_r/a_i$ is the local reflection coefficient.

The radiation stress, S_{xy}, as shown by Longuet-Higgins (1972), is related to the energy flux in the shore-normal direction associated with the wave motion for the conditions discussed here. The energy flux in the shore-normal direction, combined with (1.4) and (1.10), is given by

$$E_{fx} = E_f \cos\theta_i = \frac{1}{T}\int_0^T \rho g(\eta_i + \eta_r)(u_i + u_r)dz = (E_{fx})_i + (E_{fx})_r \tag{1.14}$$

where, by use of (1.4) and (1.6),

$$(E_{fx})_i = \frac{1}{T}\int_0^T dt \int_{-h}^{\eta} \rho g \eta_i u_i dz = \frac{1}{T}\int_0^T dt \int_{-h}^{\eta} \rho v_i u_i \frac{\sqrt{gh}}{\sin\theta_i} dz = (S_{xy})_i \frac{\sqrt{gh}}{\sin\theta_i} \tag{1.15}$$

in which $\dfrac{\sqrt{gh}}{\sin\theta_i}$ is treated as constant, by virtue of Snells Law (1.6).

Thus, the local net radiation stress is given by

$$S_{xy} = (S_{xy})_i + (S_{xy})_r = (E_{fi} - E_{fr})\cos\theta_i \frac{\sin\theta_i}{\sqrt{gh}} \tag{1.16}$$

in which

$$E_{fi} = \frac{1}{2}\rho g a_i^{\,2}\sqrt{gh} = \frac{1}{R^2}E_{fr} \tag{1.17}$$

With these general expressions for the radiation stress, expressed in terms of wave energy flux, we obtain from (1.16), for a wave field consisting of an incident and reflected wave, the net driving force on a shore parallel slice of fluid

$$\frac{\partial S_{xy}}{\partial x} = [\frac{\partial}{\partial x}(E_{fi}\cos\theta_i) - \frac{\partial}{\partial x}(E_{fr}\cos\theta_i)]\frac{\sin\theta_i}{\sqrt{gh}} \tag{1.18}$$

This driving force is balanced by a mean bottom shear stress, τ_{by}, due to the combined action of waves and longshore currents, v_c. Following Longuet-Higgins (1970) this bottom shear may be written as

$$\tau_{by} = \frac{2}{\pi}\rho C u_{bm} v_c \tag{1.19}$$

where C is a friction factor and u_{bm} is the maximum near-bottom wave orbital velocity in the shore-normal direction. Equation (1.19) is obtained under the assumptions that the wave orbital velocity is exclusively in the shore-normal direction, i.e., $\theta_i = \pi$ and dominates the current, i.e., $v_c/u_{bm} << 1$. From (1.4) and (1.10) we obtain

$$u_{bm} = |u_i + u_r| = \sqrt{\frac{g}{h}}[a_i^2 + a_r^2 - 2a_i a_r \cos(2\int_{x_w}^{x}\frac{\omega}{\sqrt{gh}}dx + \psi_{rw})]^{\frac{1}{2}}|\cos\theta_i| \tag{1.20}$$

which shows the variation of velocity characteristic of a partially standing wave for which the surface amplitude is given by (1.1) and (1.9) as

$$a = |\eta_i + \eta_r| = (a_i^2 + a_r^2 + 2a_i a_r \cos(2\int_{x_w}^{x}\frac{\omega}{\sqrt{gh}}dx + \psi_{rw}))^{1/2} \tag{1.21}$$

i.e., the orbital velocity is a maximum under a node where the surface amplitude is minimum and vice versa under antinodes.

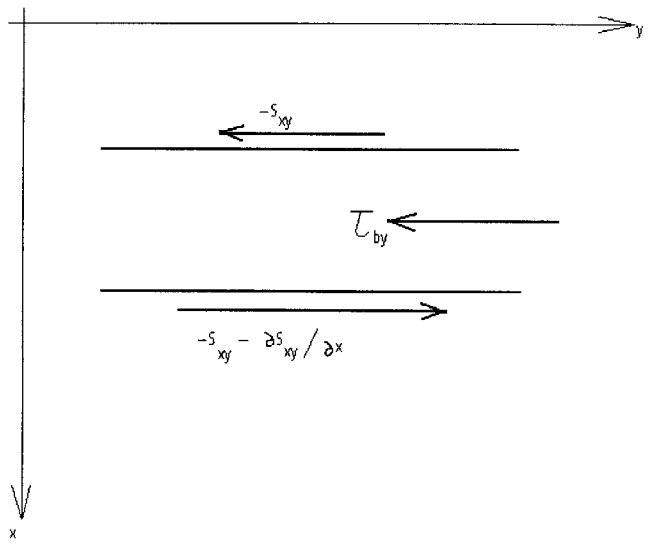

Figure 1-2 Along-shore force balance in the surf zone

Considering, for simplicity, only the driving force associated with the radiation stress and the resistance offered by the bottom shear stress, i.e., neglecting turbulent lateral shear forces, the basic momentum balance in the longshore direction, shown in Figure 1-2, becomes

$$\frac{\partial S_{xy}}{\partial x} + \tau_{by} = 0 \tag{1.22}$$

with S_{xy} given by (1.17) and (1.18), τ_{by} given by (1.19) and (1.20).

Outside the surf zone, $x > x_B$, i.e., in the absence of wave breaking, the dissipation of wave energy is negligibly small such that shore-normal energy fluxes of incident and reflected waves are constant,

$$\frac{\partial}{\partial x}(E_{fi}\cos\theta_i) = \frac{\partial}{\partial x}(E_{fr}\cos\theta_i) = 0 \text{ for } x > x_B \tag{1.23}$$

and the driving force for longshore currents vanishes, resulting in $v_c = 0$ for $x > x_B$ by use of (1.22) and (1.19).

Inside the surf zone, $x < x_B$, wave breaking dissipates energy and therefore produces a longshore current driving force as shore-normal energy fluxes now vary with x. In the presence of a reflective seawall we do not have any model from which we can obtain the variation in driving stress across the surf zone. Several models for the rate of dissipation of wave energy for a progressive breaking wave, in the absence of reflected waves, have been advanced, e.g., Battjes and Janssen (1978) and Dally et al. (1985). Recently, McDougal (1996) modified the Dally et al. dissipation model to take reflected waves into account. However, the dissipation was treated as if it were exclusively associated with the incident wave. This effectively amounts to neglecting the contribution of the reflected wave to the radiation stress gradient in (1.18), an assumption also made by Brown (1996) who further assumed the incident wave to behave as if it were alone.

Missing in the above analysis is the crucial information on the variation of incident and reflected wave amplitudes across the surf zone. To obtain this information is the objective of this study, and with this information available from our experimental investigation, we

can formulate a longshore current model, which explicitly accounts for the effect of a reflecting seawall located within the surf zone.

1.3 Experimental study

The preceding theoretical considerations have shown that the amplitude variations of incident and reflected waves inside the surf zone need to be quantified in order to evaluate incident and reflected wave energy flux terms given by (1.17) and appearing in the expression for the radiation stress gradient (1.18). After this is established we can attempt a rational prediction of wave-induced longshore currents in the presence of seawalls located in the surf zone. To achieve the objective of this research project, laboratory experiments are performed to determine the changes in the wave characteristics across a gently sloped surf zone bounded by a reflective structure. To be extracted from this information is the rate of energy dissipation experienced by incident as well as reflected waves as a function of location within the surf zone, incident wave characteristics and reflective properties of the seawall. Based on the experimental determination of energy losses of incident and reflected waves, we will verify and/or modify the model developed by Madsen and Brown (1996) for wave-induced longshore currents along seawall protected beaches as a function of the seawall's reflective characteristics and its location within the surf zone.

Periodic waves normally incident on a gently sloping beach (1 on 30) are generated in the large wave flume in the Ralph M. Parsons Laboratory. Since the angle of incidence of obliquely incident waves is generally small, when they reach breaking and beyond,

normal incidence is considered a realistic simplification of actual conditions in a surf zone.

Surface profiles are measured along the flume starting from the constant depth portion and continuing up to the slope through the surf zone. By fitting the theoretical variation of the wave amplitude variation to the observations, the variation of incident and reflected wave amplitudes along the flume and across the surf zone are determined. This variation is, in turn, used to obtain an estimate and a model for the wave-associated driving force for longshore currents as a function of location and reflective characteristics of the seawall.

In addition to water surface displacement measurements, velocities are measured using a SonTek ADV - Acoustic Doppler Velocimeter. The information on the variation of the velocity signal plus the surface profile information are used together to extract incident and reflect wave components. The theoretical development necessary to use this experimental procedure is presented in Chapter 2, along with a detailed description of the experimental set-up and methodology.

Experimental results without a seawall on the beach are performed in order to obtain baseline data on incident wave energy dissipation in the absence of a reflective structure, are presented in Chapter 3. Subsequent chapters present experimental results for which seawalls are either vertical (Chapter 4) or sloped (Chapter 5). The conclusions of our study are presented in Chapter 6.

Chapter 2

Experimental Setup and Data Analysis

2.1 Experimental setup

All the experimental work was carried out in the Ralph M. Parsons Laboratory at the Massachusetts Institute of Technology. The main setup was a large wave flume equipped with a piston-type servo-controlled wave maker. Additional equipment included wave gauges to record surface displacement, SonTek Acoustic Doppler Velocimeter (ADV) to measure velocities, computers to acquire and process data and an HP oscilloscope to monitor any possible zero position drift of wave gauge signals. Figure 2-1 shows a schematic view of the experimental installation. We will describe in more details each part of this system in the following subsections.

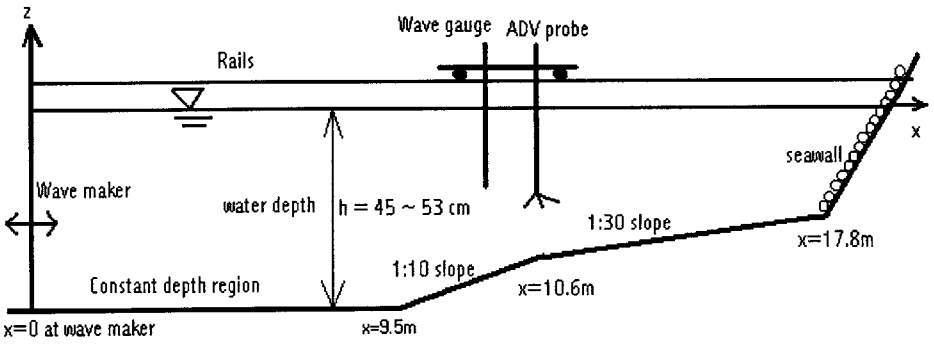

Figure 2-1 Experimental set-up (Note: The wave gauge and the ADV probe are actually in the same vertical plane.)

2.1.1 The wave flume

The wave flume is 28 m long, 76 cm wide and 85 cm high. From here on we will refer to the longitudinal axis of the channel as coordinate "x" with zero at the wave maker mean position and positive towards the beach. The beach was constructed of marine plywood and was composed of two parts, the 1 on 10 slope starting at x = 9.5 m and 1 on 30 slope starting at x = 10.6 m (See Figure 2-1). The seawall is a 2 cm thick marine plywood board with rubbles glued to its seaward side. The toe of the seawall was located at x = 17.8 m. In order for us to easily adjust the slope of the seawall, both the seawall and two supporting beams were hinged onto the beach. The water depth was measured using a 1 meter long ruler with accuracy of 1 mm. In all the experiments the water depth at constant depth region was in the range of 45 cm to 53 cm.

The whole wave tank is supported by a metal frame, which has cross bars and a pair of legs every 1.5 m. The sidewalls and the bottom of the channel consist of 6 mm thick glass panels, except at the beginning (first 3.6 m), which are not glass but metal plates. The bottom panels are reinforced by installing a central support along the channel consisting of a large I-beam supported on the metal frame itself. Every 3 m along the channel there are silicon sealer junctions of glass panels. These sealer junctions are bands of about 5 cm wide on both walls and bottom.

Along the channel, on top of the metal frame, there are two rails consisting of metal pipes 3.2 cm in outer diameter. A rigid metal trolley with wheels underneath was placed on the

rails. The measuring devices, i.e., wave gauges and ADV, were mounted on the trolley so that they could be moved with relative ease and smoothness.

At the beginning and end of the tank there are rectangular basins with smooth transitions to the width of the flume itself. The wave maker paddle and the beach isolate the channel from those basins. All the gaps between the beach, seawall, sidewalls and bottom of the tank were taped tightly to prevent leakage of water from the wave tank to the basin. In the basin behind the wave maker several pieces of 5 cm thick fibrous material are submerged in the water in order to reduce the wave agitation behind the wave maker.

2.1.2 The wave maker

The wave generating system consists of a servo-controlled, hydraulically driven, piston-type wave maker located at one end of the channel. The paddle of the wave maker moves horizontally with uniform motion over the depth. There are rubber seals on both sides and on the bottom of the paddle to reduce leakage through the gaps between the paddle and the inner channel. The system is equipped with an internal signal generator that produces sinusoidal, square and triangular monochromatic periodic signals with user-controlled frequency and amplitude. It is also possible for the wave maker to be controlled by computer-generated external signals. In our experiments only internal sinusoidal signals were used.

2.1.3 The wave gauge

The wave gauge, used to measure surface displacement, consists of a pair of thin (0.13 mm in diameter) nichrome wires (20% chromium, 80% nickel) arranged vertically, parallel to each other 4 mm apart. The wires are placed under tension using a 45×15 cm frame made of 6 mm diameter stainless steel tube, the longer leg of the frame parallel to the wires (15 cm away from them) in such a way that the frame and wires lie in a vertical plane normal to the axis of the channel. The wires and frame are mounted on a rack and pinion system that allows accurate vertical positioning using a built-in scale marked at 1mm intervals. When positioned, the pair of thin wires pierces the free surface and detects the change in total conductivity between the wires, which is a function of the length submerged in the water. The supporting frame produces very small disturbances to the surface when waves pass the gauge location. These "disturbing" wavelets are of frequencies far higher than the generated waves and therefore not interfering appreciably with the measurements. The nichrome material has the advantage of not producing an oxide film, which could affect the temporal stability of calibrations.

The wave gauge is supplied with an AC excitation voltage by a wave gauge controlling unit (resistance measuring device). The gauge responds to the changes in water surface elevation with an AC signal, which is demodulated and filtered by the controlling unit producing a DC voltage. This DC voltage follows the variation of the surface. The signal of the wave gauge is monitored with a Hewlett Packard Corporation oscilloscope model 54601A.

The output DC signals from the wave gauge controlling unit is sent to an external terminal box connected to an analog data acquisition card inside the desktop computer. The data acquisition card has adjustable analog ranges that in our case were always set within the –10 v to 10 v range. The A/D (analog to digital signal) conversion is done using a 12-bit successive approximation converter.

To obtain the water displacement vs. voltage relationship, the wave gauge calibration is the first step in a surface wave measurement. Wave gauge calibration was done before the experiment at one location, usually within the constant depth region, and once after the experiment at the same location. Performing the calibration requires a still water level. The drift of the zero observed on an oscilloscope provided information on the validity of the calibration. If in some cases (less than 10% of the experiments) drift was found unacceptable, usually ±3 mm around the original zero position, after a measurement has been done, a posteriori calibration would be used. Though the zero position shifted in such cases, the unit change in voltage still mapped to the same surface displacement change as in prior calibrations, for instance, a change of 1 v in voltage still corresponded to a change of 2 cm in surface displacement. Before running the wave maker, i.e., at still water level, we also took a 0.5 min long record at each location along the length of the flume. From the mean water surface we can tell the difference in rail elevation (due to the slight unevenness along the rails) between the calibration and other measurement locations. Therefore, those data may be used to adjust the wave gauge zero reading position at those locations.

Each time we calibrate, we have to estimate the range of water surface displacements for the wave conditions with some spare room left for reflection and higher harmonics, and place the gauge elevation in a position that will cover the whole range. The signal is amplified or reduced to map this physical surface displacement range into about 80% of the voltage range (-10 v to 10 v), and the zero voltage set for the still water level.

The calibration is aided by a computer program, which performs all tasks except physically moving the elevation of the gauge. Typically, the calibration was done with 13 points uniformly distributed, 3 cm apart, in the whole range. Each point (voltage, surface displacement) was obtained by sampling 400 times and getting the mean value for the voltage. The purpose of doing so is to average out small high frequency wavelets sometimes present due to vibrations produced by vehicles on the street outside the laboratory. Typically the standard deviation of the 400 samples was of the order of 1×10^{-2} cm. Once all points were sampled, a least squares cubic polynomial fit was performed, obtaining the coefficients of the polynomial which express surface displacement in terms of voltage. The relationship was quite linear, but the quadratic and cubic terms were still needed to keep the standard error at an acceptable level. A text file containing the coefficients was generated by the program and later was used to map voltages to actual displacement.

Typically the standard error of the cubic polynomial fit was of the order of 3×10^{-2} cm which could be interpreted as an estimate of the accuracy of each of the points in a surface displacement record. Notice that the weakest link in the measuring system is

probably the accuracy with which the operator can place the gauge at each of the calibration levels. Thus the millimeter scale on the wave gauge can be reasonably expected to be close to the standard error found.

2.1.4 The SonTek ADV

The SonTek ADV (Acoustic Doppler Velocimeter) is a versatile, high-precision instrument used to measure three dimensional (3D) water velocities. The ADV uses acoustic Doppler technology to measure 3D flow in a small sampling volume (less than 0.2 cm^3) located a fixed distance (5 cm in our experiments) from the probe (Figure 2-2). The velocity range is programmable from ±3 to ±250 cm/s. Data can be acquired at sampling rates up to 25 Hz. With no zero offset, the ADV can measure flow velocities from less than 1 mm/s to over 2.5 m/s.

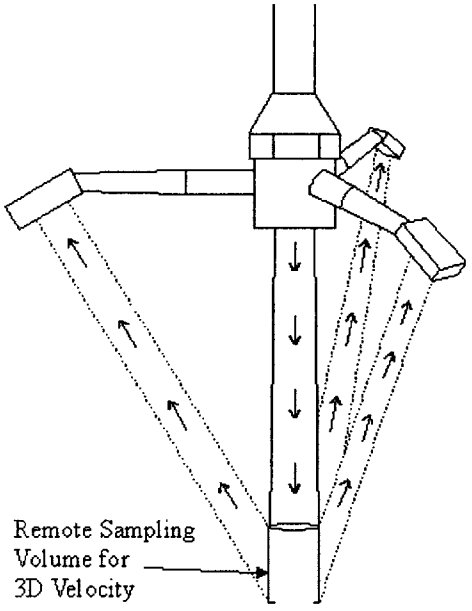

Figure 2-2 The SonTek ADV probe and sampling volume

The ADV consists of three basic elements: the probe, the signal-conditioning module, and the processor. The probe is attached to the conditioning module, which contains low-noise receiver electronics enclosed in a submersible housing. The ADV conditioning module and probe are connected to the processing module using a shielded cable about 15 m long.

2.1.4.1 The ADV probe

The precise location of the ADV sampling volume is determined by probe geometry. The distance from the tip of the probe to the sampling volume in our experimental setup is 5 cm, which is sufficient to avoid flow interference. The acoustic sensor was mounted on a rigid stem 40 cm long (See Figure 2-3). The down-looking sensor orientation is in our case ideal for measurements close to the bottom.

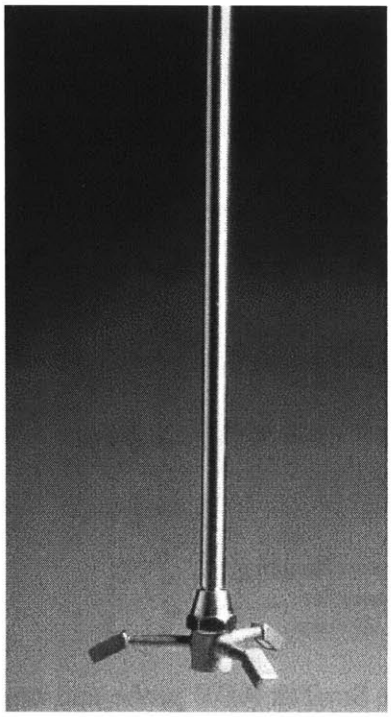

Figure 2-3 The SonTek ADV probe and mounting stem

2.1.4.2 The ADV signal-conditioning module

The ADV signal-conditioning module is a cylindrical aluminum housing that is anodized and powder coated for corrosion protection. The cable to the processing module is permanently attached using an underwater penetrator. The probe is attached to the front end-bell of the housing.

2.1.4.3 The ADV processor

The ADVLab is used with a desktop PC in the laboratory setting (the processor card is installed inside the computer). All communication and power are handled through the computer I/O (input and output) bus. Also installed in the computer is an analog data acquisition card to sample eight analog voltages, which in our case only one channel is used to measure the signal from the wave gauge. The ADV software can be used to collect, display, and record data from the ADV and analog sensors (wave gauges in our study).

2.2 Data acquisition and analysis

2.2.1 Theoretical basis for temporal analysis

Linear wave theory was used in the data analysis. In the following sections, the coordinate system is defined as follows. "x" is in the longitudinal direction along the channel and positive toward the beach. "z" is in the vertical direction with zero at the still water level and positive upward. "y" is in the transverse direction with zero at the center of the wave flume so that "x"; "y" and "z" axes abide by the right-hand rule.

The incident and reflected plane waves can be expressed locally as

$$\eta_i = a_i \cos(kx - \omega t + \varphi_i) \tag{2.1}$$

$$\eta_r = a_r \cos(kx + \omega t + \varphi_r) \tag{2.2}$$

where a is the wave amplitude, φ being phase angle, subscripts i and r standing for incident and reflected waves, ω radian frequency, and $k = k(x)$ local wave number related through dispersion relationship

$$\omega^2 = gk \tanh kh \tag{2.3}$$

where $h = h(x)$ is the local water depth. Therefore, at any time, the surface displacement at location x is

$$\eta = \eta_i + \eta_r = \cos\omega t[a_i \cos(kx + \varphi_i) + a_r \cos(kx + \varphi_r)]$$
$$+ \sin\omega t[a_i \sin(kx + \varphi_i) - a_r \sin(kx + \varphi_r)] \tag{2.4}$$

Further, by use of simple trigonometry, (2.4) can be written as

$$\eta = A_1 \cos(\omega t + \varphi_{A_1}) = \cos\omega t[A_1 \cos\varphi_{A_1}] + \sin\omega t[-A_1 \sin\varphi_{A_1}] \tag{2.5}$$

The horizontal velocities in the x direction of incident and reflected waves are expressed as

$$u_i = a_i \omega \frac{\cosh k(z+h)}{\sin kh} \cos(kx - \omega t + \varphi_i) \tag{2.6}$$

$$u_r = -a_r \omega \frac{\cosh k(z+h)}{\sin kh} \cos(kx + \omega t + \varphi_r) \tag{2.7}$$

where $h + z$ is the distance from the bottom boundary to the sampling volume of the ADV and this value can be recorded by the ADV software, and $h = h(x)$ is the local

water depth. The velocity at a certain location x and water level $h+z$ is the sum of u_i and u_r:

$$u = u_i + u_r = \omega \frac{\cosh k(z+h)}{\sin kh} \cos\omega t[a_i \cos(kx+\varphi_i) - a_r \cos(kx+\varphi_r)]$$

$$+\omega \frac{\cosh k(z+h)}{\sin kh} \sin\omega t[a_i \sin(kx+\varphi_i) + a_r \sin(kx+\varphi_r)] \qquad (2.8)$$

Similar to η, u can be rewritten as

$$u = U_1 \cos(\omega t + \varphi_{U_1}) = \cos\omega t[U_1 \cos\varphi_{U_1}] + \sin\omega t[-U_1 \sin\varphi_{U_1}] \qquad (2.9)$$

Suppose we know U_1, φ_{U_1}, A_1 and φ_{A_1}. By matching (2.4) with (2.5), and (2.8) with (2.9), i.e.,

$$A_1 \cos\varphi_{A_1} = a_i \cos(kx+\varphi_i) + a_r \cos(kx+\varphi_r) \qquad (2.10)$$

$$-A_1 \sin\varphi_{A_1} = a_i \sin(kx+\varphi_i) - a_r \sin(kx+\varphi_r) \qquad (2.11)$$

$$U_1 \cos\varphi_{U_1} = \omega_z a_i \cos(kx+\varphi_i) - \omega_z a_r \cos(kx+\varphi_r) \qquad (2.12)$$

$$-U_1 \sin\varphi_{U_1} = \omega_z a_i \sin(kx+\varphi_i) + \omega_z a_r \sin(kx+\varphi_r) \qquad (2.13)$$

with

$$\omega_z = \omega \cosh k(h+z) / \sinh kh \qquad (2.14)$$

we solve these four equations with four unknowns, i.e., a_i, a_r, φ_i and φ_r, getting

$$a_i = \frac{1}{2\omega_z}[U_1^2 + (\omega_z A_1)^2 + 2U_1\omega_z A_1 \cos(\varphi_{A_1} - \varphi_{U_1})]^{1/2} \qquad (2.15)$$

$$a_r = \frac{1}{2\omega_z}[U_1^2 + (\omega_z A_1)^2 - 2U_1\omega_z A_1 \cos(\varphi_{A_1} - \varphi_{U_1})]^{1/2} \qquad (2.16)$$

$$\cos(kx+\varphi_i) = \frac{1}{2\omega_z a_i}(\omega_z A_1 \cos\varphi_{A_1} + U_1 \cos\varphi_{U_1}) \qquad (2.17)$$

$$\sin(kx+\varphi_i)=\frac{1}{2\omega_z a_i}(-\omega_z A_1 \sin\varphi_{A_1}-U_1\sin\varphi_{U_1}) \tag{2.18}$$

$$\cos(kx+\varphi_r)=\frac{1}{2\omega_z a_r}(\omega_z A_1 \cos\varphi_{A_1}-U_1\cos\varphi_{U_1}) \tag{2.19}$$

$$\sin(kx+\varphi_r)=\frac{1}{2\omega_z a_r}(\omega_z A_1 \sin\varphi_{A_1}-U_1\sin\varphi_{U_1}) \tag{2.20}$$

The above analysis shows how we resolve the incident and reflected wave components using two pieces of information, the surface displacement and horizontal velocity, at one location x. The reflection coefficient R is defined as

$$R=a_r/a_i \tag{2.21}$$

The following subsection discusses how to resolve incident and reflected wave components from spatial analysis, i.e., from the surface displacement analysis of several points within a short distance.

2.2.2 Theoretical basis for spatial analysis

From equation (2.4) and (2.5), we obtain

$$A_1=[a_i^2+a_r^2+2a_i a_r\cos(2kx+\varphi_i+\varphi_r)]^{1/2} \tag{2.22}$$

From here on, we will use x_j, x coordinate of each location as its identification number where n is the total number of stations with $j=0,...n-1$ along the wave flume. Outside the surf zone, the variation in wave height is largely due to shoaling, bottom friction and sidewall friction. Inside the surf zone, wave breaking becomes the dominant element for wave height decay. In either zone, the incident wave height can be assumed to decay linearly within a short distance (from x_j to x_{j+k}, $k>1$ is an integer) in the direction of

wave propagation if there is no significant change in bottom profile (e.g., steep step) and no wave breaking.

$$a_i(x) = a_i(x_j) + \alpha x,\ x_j \le x \le x_{j+k} \tag{2.23}$$

where $a_i(x_j)$ is a constant from x_j to x_{j+k} and α is the decay coefficient and can be either greater or less than zero. Similarly, the reflected wave height can be expressed as

$$a_r(x) = a_r(x_j) + \beta x,\ x_j \le x \le x_{j+k} \tag{2.24}$$

where β is the decay coefficient of reflected waves. Again, reflection coefficient is defined as $R(x) = a_r(x)/a_i(x),\ x_j \le x \le x_{j+k}$.

Therefore, (2.22) can be rewritten as

$$A_1 = [(a_i(x_j)+\alpha x)^2 + (a_r(x_j)+\beta x)^2 + 2(a_i(x_j)+\alpha x)\cdot(a_r(x_j)+\beta x)\cdot\cos(2kx+\varphi_i+\varphi_r)]^{1/2} \tag{2.25}$$

In our experiments, we took measurements at such intervals that $x_{j+1} - x_j \le \frac{1}{4}\frac{2\pi}{2k} = \frac{\pi}{4k}$, a quarter of local beat length. Thus, we can use nonlinear curve fit to resolve the local incident, reflected wave components, the reflection coefficient, and the decay of the incident and reflected waves with higher accuracy.

A nonlinear least-squares data fitting by the Gauss-Newton method was used in the spatial analyses. The MATLAB function $NLINFIT(X, Y, 'MODEL', BETA0)$ finds the coefficients of the nonlinear function described in $MODEL$. $MODEL$ is a user supplied function having the form $y = f(beta, x)$. That is $MODEL$ returns the predicted values of y given initial parameter estimates, $BETA0$, and the independent variable, X.

$[BETA, R, J] = NLINFIT(X, Y, 'MODEL', BETA0)$ returns the fitted coefficients $BETA$, the residuals, R, and the Jacobian, J, for use with another MATLAB function $NLINTOOL$ to produce error estimates on predictions.

In this case, the $MODEL$ is equation (2.25), X is a vector $[x_j, x_{j+1}, ...x_{j+k}]$ in which $x_j ... x_{j+k}$ are the stations used for nonlinear curve fit, Y is the wave amplitude vector at corresponding locations $x_j ... x_{j+k}$ and is obtained from FFT. $BETA$ is the vector of coefficients $[a_i(x_j), a_r(x_j), \alpha, \beta, k, \varphi_i + \varphi_r]$ while $BETA0$ is the initial estimate of this vector. Wave number k is treated as a constant over this short distance and is obtained by solving the dispersion relationship (2.3).

One practical problem in using the above method is that lots of combinations of a_{i0}, α, a_{r0}, β, k and $\varphi_i + \varphi_r$ may locally fit the curve very well. However, most of the combinations give unreasonable results, for example, the resulting reflection coefficient is positive for some data points and negative for the others no matter what phase angle is chosen. Another problem is that $NLINFIT$ function is sensitive to the wave number k, which in this case varies over the short distance from x_j to x_{j+k}. Common to nonlinear optimization, the initial values of the parameters and steps will determine if the final result falls into a local minimum. Most important, the straight application of this method neglects the information of adjacent segments of the curve, i.e., the requirement of smooth transition of both incident and reflected wave amplitude. Given this requirement, the problem turns out to be that of constrained nonlinear optimization, which is not well

solved yet. Therefore in practice, those parameters are first estimated from the curve trend. The upper and lower envelopes are sketched on the figure of total amplitude variation, and initial estimates for the incident wave amplitude variation (a_{i0} and α) are obtained from the center line of the two envelopes. Initial estimates for the reflected wave amplitude variation (a_{r0} and β) are then obtained from the envelope variation around the center line. Taking these estimated parameters as the initial values, function *NLINFIT* is then used to do the curve fitting. Or we can also apply small adjustments to those estimated parameters and find the best least squares.

2.2.3 Data acquisition and analysis

The water surface displacement was measured by a wave gauge, while the velocities were measured by the ADV. The frame of the wave gauge and the ADV probe were placed in the same vertical plane, normal to the longitudinal axis of the channel. Thus, in the case of plane waves as ours, they actually measure at the same x location. During an experiment, the measurements were taken at each location for a period of time, typically 3 to 5 minutes. The choice of measurement locations is dependent upon the local wave number or local wavelength. The wave period is adjustable through the wave maker control panel and can be read on the HP oscilloscope. With the water depth at each location measured, we can then calculate the local wave number from the dispersion relationship equation (2.3). Those points, which divide the local wavelength into 8 pieces evenly spaced, would be chosen as measurement locations. By doing so, we can actually have 5 points within a beat length, which are enough for us to obtain the beat profile using a nonlinear curve fit.

The raw data were stored into binary files compressed in ADV format. Using the software shipped by SonTek, we were able to determine the distances both from the sampling volume to the boundary ($h + z$ in section 2.2.1) and from the ADV probe tip to the boundary, and extract the water surface displacement and velocities from the ADV files and save these data into pure text files. One of the advantages of using text files is that almost all data analyzing and scientific computing software identify or even require text file inputs. The other advantage is to simplify the transfer of the data files over network, as we do not have to encode the binary files. The computer used to record data was a Dell 486 (Intel CPU, 66MHz), too slow for use in analyzing data. We then need to do the analysis on a much faster machine on which we can run the analysis software like MATLAB and Microsoft Office 97. Saving all the data as well as the results in text file format makes it much easier and less painful to transfer files between different systems, e.g., PCs running Windows operating system and SUN SPARCS running Solaris in our study. We also used the high capacity Iomega disks (100 megabytes/disk) to store the raw ADV files as well as wave gauge calibration information for each experiment. The only apparent disadvantage of using text files, is the increase in file size. However, the huge capacity of the computers nowadays eliminates this drawback completely.

The wave surface displacement and velocity data are essentially time series equally spaced, e.g., 40 ms apart if the sampling rate is 25 Hz, so we can Fourier analyze these data to obtain frequency spectra. Some MATLAB programs were written to fulfill this task, in which fast Fourier analysis (FFT) was employed. We know that the actual wave

period was just around the wave maker period reading (with limited accuracy) from the oscilloscope. Therefore, we can find the exact frequency by choosing different number of points in the FFT such that both surface displacement and horizontal velocity frequency spectra become clear-cut and the main harmonic components reach their maximum with minimal sidelobes.

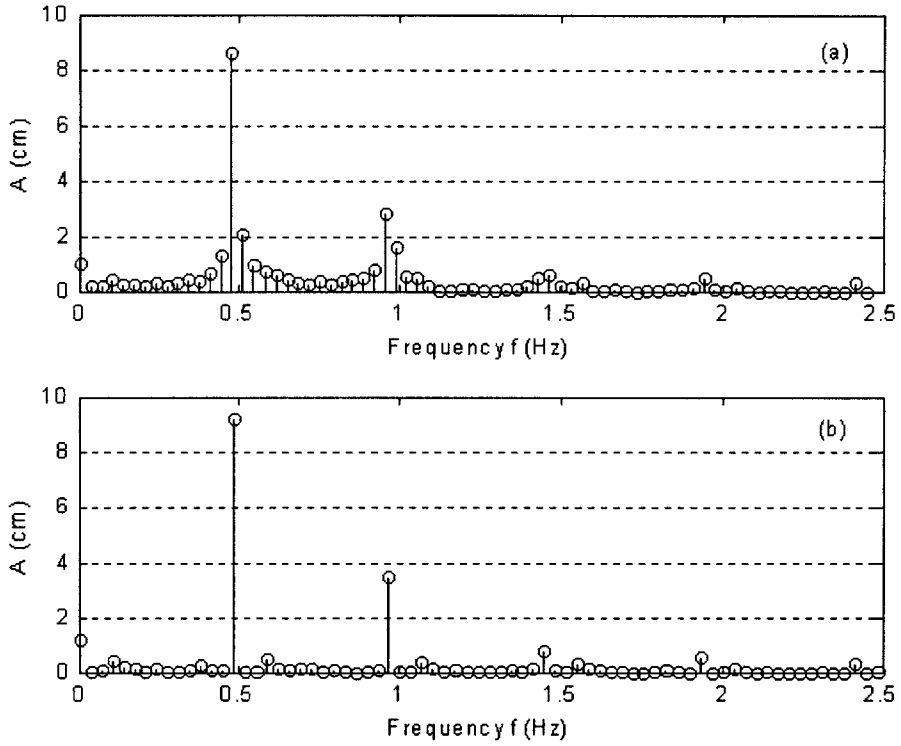

Figure 2-4 Effect of "fine-tuning" frequency output values of FFT

(a) No fine-tuning; (b) With fine-tuning

Figure 2-4 shows how fine-tuning the FFT frequency output values would affect the FFT amplitude outputs (as well as velocity outputs, which are not presented). Figure 2-4 (a) was obtained by inputting into FFT program the first 735 points of the water surface displacement measurement during an experiment, sampled with a frequency of 25 Hz,

i.e., at the interval of 40 ms. The peak value of the first harmonic component, A_1 = 8.6726 cm (with a phase angle of 148.9 degrees, not shown in the above figure), appeared at frequency f = 0.4762 Hz. While in figure 2-4 (b), the number of points in FFT was adjusted to 725, then the peak value of the first harmonic amplitude, A_1 = 9.2503 cm (phase angle = 113.7 degrees), appeared at f = 0.4828 Hz. Although the main frequency only shifted by +1.4% from 0.4762 Hz to 0.4828 Hz, the first harmonic amplitude increased by 6.7% and the phase angle decreased by 23.6%. From this typical example, we see that the number of points in FFT plays an important role in locating the wave period and extracting information (amplitudes and phases) of various harmonic components from wave records.

Given the number of points in a time series, N, and the time step Δt (related to sampling frequency $f_{sampling}$ by $f_{sampling} = 1/\Delta t$), the frequency vector outputted from FFT will be $[0,\ \Delta f,\ 2\cdot\Delta f,\ \ldots,\ (N-1)\cdot\Delta f]$ in which $\Delta f = f_{sampling}/N$. The purpose of adjusting the number N in the FFT, therefore, is to look for an optimum combination of an integer n and a frequency step Δf, such that $n\cdot\Delta f$ is close to the actual main frequency and produces a sharp peak value. In the above example of 725-point-FFT, $\Delta f = 1/(725\cdot 0.04) = 0.0345$ Hz and $n = 14$.

This way, we obtained the first and other higher harmonics using our programs. Applying the theory presented in section 2.2.1, we thus resolved the incident and reflected wave components from the time series of surface displacement and horizontal velocity. The

results on incident and reflected waves would be further used for other analysis, e.g., energy dissipation patterns of incident and reflected waves, reflection coefficients, to name a few.

The experimental results in the absence of a reflective structure, in the presence of a vertical seawall and a sloped seawall are presented in subsequent Chapters 3, 4 and 5, respectively.

Chapter 3

Experimental Results in the Absence of Seawalls

3.1 Overview of experiments

Sets of experiments with different wave periods ranging from 1.5 to 2.5 seconds were carried out in the absence of a highly reflecting structure in the surf zone to provide the baseline data of incident wave energy dissipation. In the following typical result, the wave period is 2.06 seconds and the water depth in the constant depth region is 50.0 cm. The breaking of the waves occurred visually around x = 13.1 m and the breakers can be classified as spilling type. The wave maker was run 10 minutes in order for stationarity to be established before measurements were taken. A three-minute record of both water surface displacement and velocity was taken at 77 locations from x = 5.0 m to x = 17.2 m along the wave flume. Since the wave-length shortened with the decrease of water depth, the measurements were taken 25 cm apart in the constant depth region, 20 cm apart before wave breaking and 10 cm apart after breaking, in order to obtain enough resolution within a beat length. The SonTek software was used to extract the surface displacement and velocity from the raw data, followed by the Fast Fourier Transform (introduced in Section 2.2.3) to retrieve various harmonic components. The following Section 3.2 presents 25-second segments of wave records and the corresponding

frequency spectra at five characteristic locations. Section 3.3 gives the cross-shore variation of incident and reflected wave characteristics and reflection coefficients.

3.2 Wave records and frequency spectra

Figures 3-1 and 3-2 present the segments of surface displacement records, $\eta(t)$, and horizontal velocity records, $u(t)$, at typical locations along the wave flume. Figure 3-1 (a) shows $\eta(t)$ at x = 7.0 m which is in the constant depth region of the flume. The surface profile in this region is seen to be highly nonlinear and the wave height is about H = 20.0 cm, where H is defined as the average of the vertical distances from the crest level to the trough level of n (n = 10 in the following analysis) successive waves.

$$H = \frac{1}{n}\sum_{i=1}^{n}(\eta_{\max} - \eta_{\min})_i \tag{3.1}$$

Given the constant portion's water depth h = 50.0 cm and wave period T = 2.06 s, the wave length calculated using linear theory is L = 4.20 m and the Ursell parameter, $U = HL^2/h^3$ = 28.2, indicates that the waves are highly nonlinear. The relatively sharp peaks and flat troughs can also be seen from the horizontal velocity record in Figure 3-2 (a). Figures 3-1 and 3-2 (b) are from x = 12.6 m, a location slightly before the visually determined location of breaking. The forward leaning crests are reflected in both surface and velocity records. It is noted that the records both immediately before and after breaking, shown in Figures 3-1 and 3-2 (c), are very periodic with each wave being virtually identical to its neighbors.

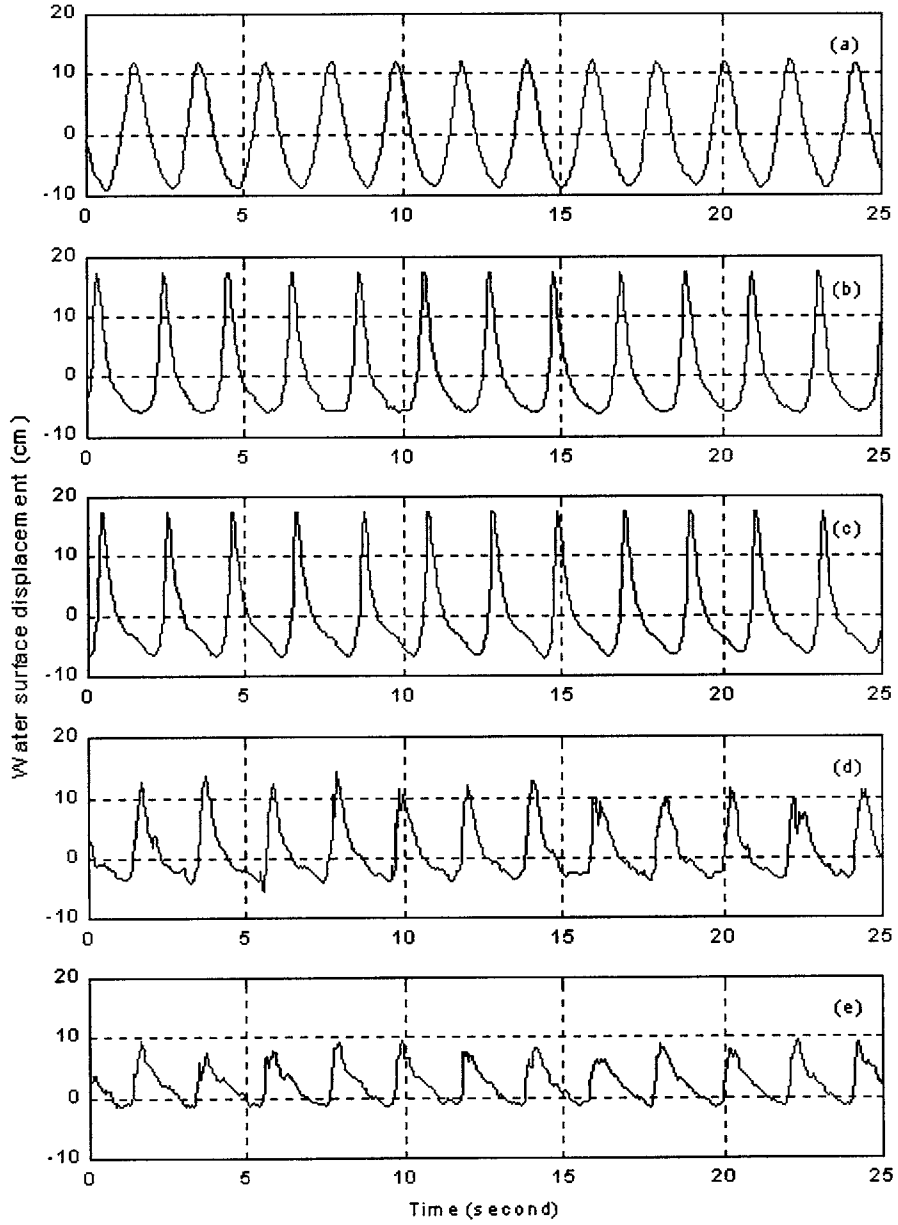

Figure 3-1 Surface displacement records taken by the wave gauge; (a) x = 7.0 m, constant depth region; (b) x = 12.6 m, right before wave breaking; (c) x = 13.4 m, right after wave breaking; (d) x = 15.0 m, breaking zone; (e) x = 17.1 m, farther away from the breaking point.

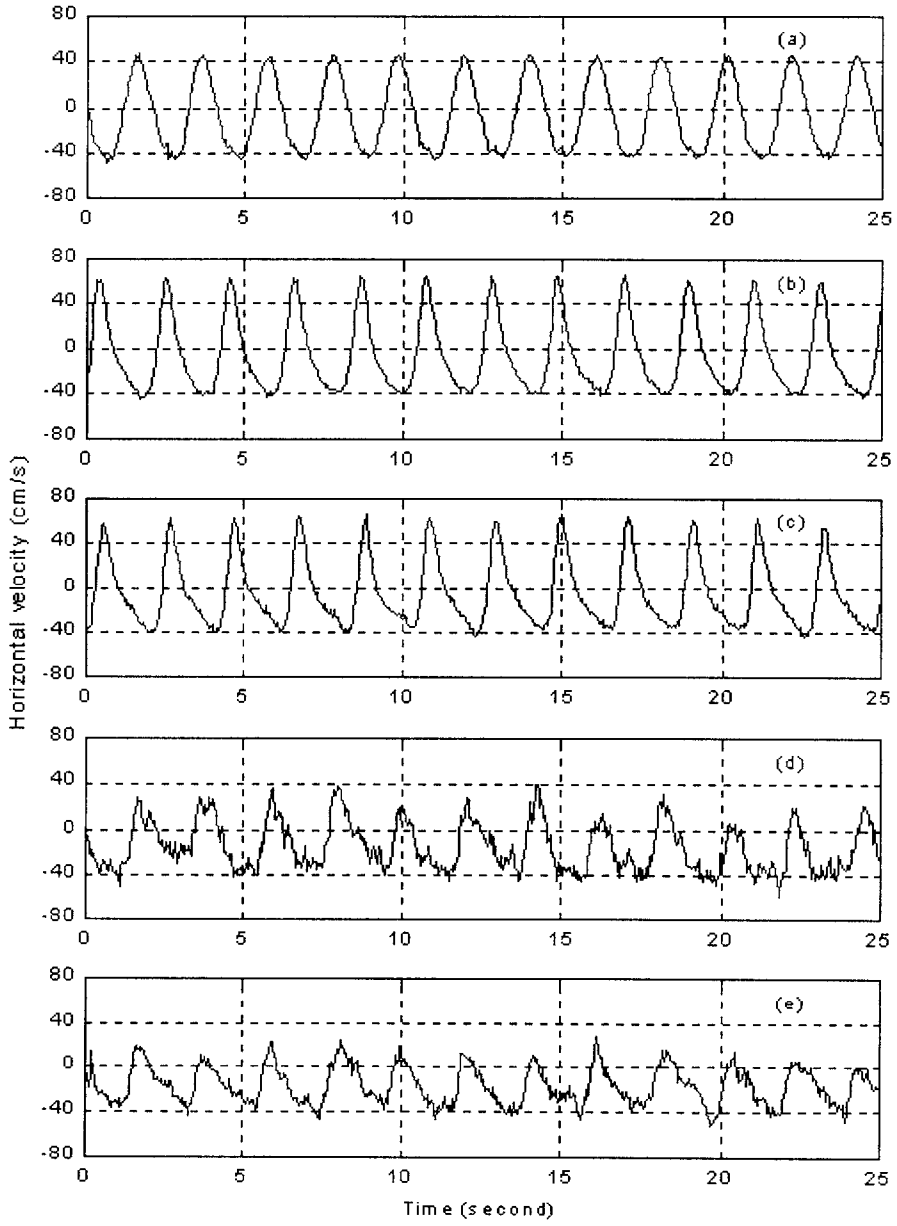

Figure 3-2 Horizontal velocity records taken by the SonTek ADV; (a) x = 7.0 m, constant depth region; (b) x = 12.6 m, right before wave breaking; (c) x = 13.4 m, right after wave breaking; (d) x = 15.0 m, breaking zone; (e) x = 17.1 m, farther away from the breaking point.

Recalling that the waves broke visually at x = 13.1 m, we see a clear positive offset of the mean of $\eta(t)$, corresponding to the wave setup, as we move into the surf zone (x = 15.0 and 17.1 m). The mean horizontal velocity in Figure 3-2 (d) and (e), however, exhibits an obvious negative shift from zero which is caused by the undertow, the strong seaward current generated by breaking waves. The wave height drops dramatically to about 10 cm at x = 17.1 m due to wave breaking whereas the horizontal velocity appears to be somewhat less affected.

The records of the broken waves demonstrate a characteristic saw-tooth-like variability from one wave to the next. The principle of wave gauge measurements discussed in Section 2.1.3 show that the change in total conductivity between the wires of the gauge is a function of the length submerged in the water, i.e., an indication of water surface level. In the surf zone, however, the total conductivity might be affected by the splashing surface water as well as air-entrainment and no longer be equivalent to the surface elevation. Despite this difficulty in measuring the actual surface profile of breaking waves with a surface piercing wave gauge, the signal recorded in the surf zone is still strongly periodic, as we have seen in Figure 3-1 (d) and (e).

The visual impression of the strong periodicity of the $\eta(t)$ and $u(t)$ records is reflected in the surface and velocity spectra obtained from these records and shown in Figures 3-3 and 3-4.

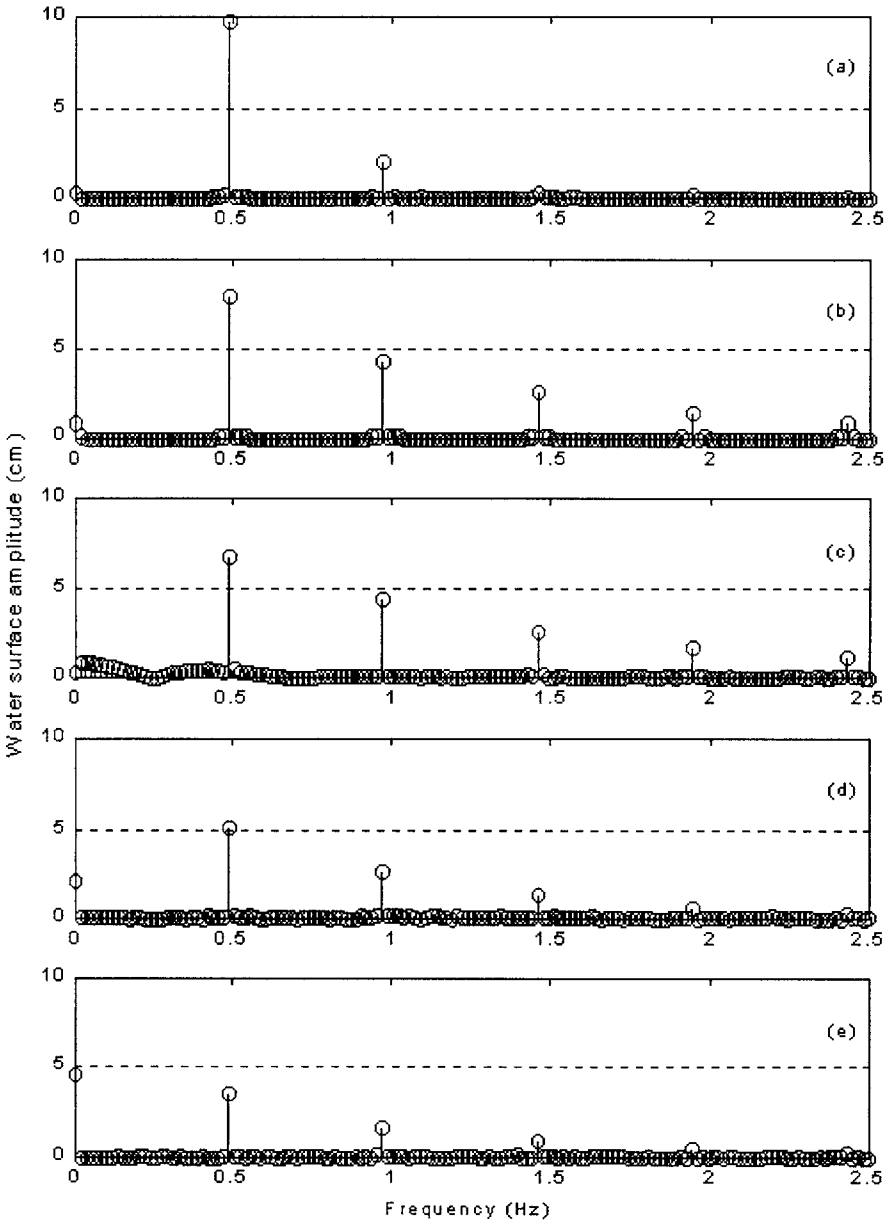

Figure 3-3 Surface displacement spectra; (a) x = 7.0 m, constant depth region; (b) x = 12.6 m, right before wave breaking; (c) x = 13.4 m, right after wave breaking; (d) x = 15.0 m, breaking zone; (e) x = 17.1 m, farther away from the breaking point. Note: Only the first 150 points are shown in the above spectra.

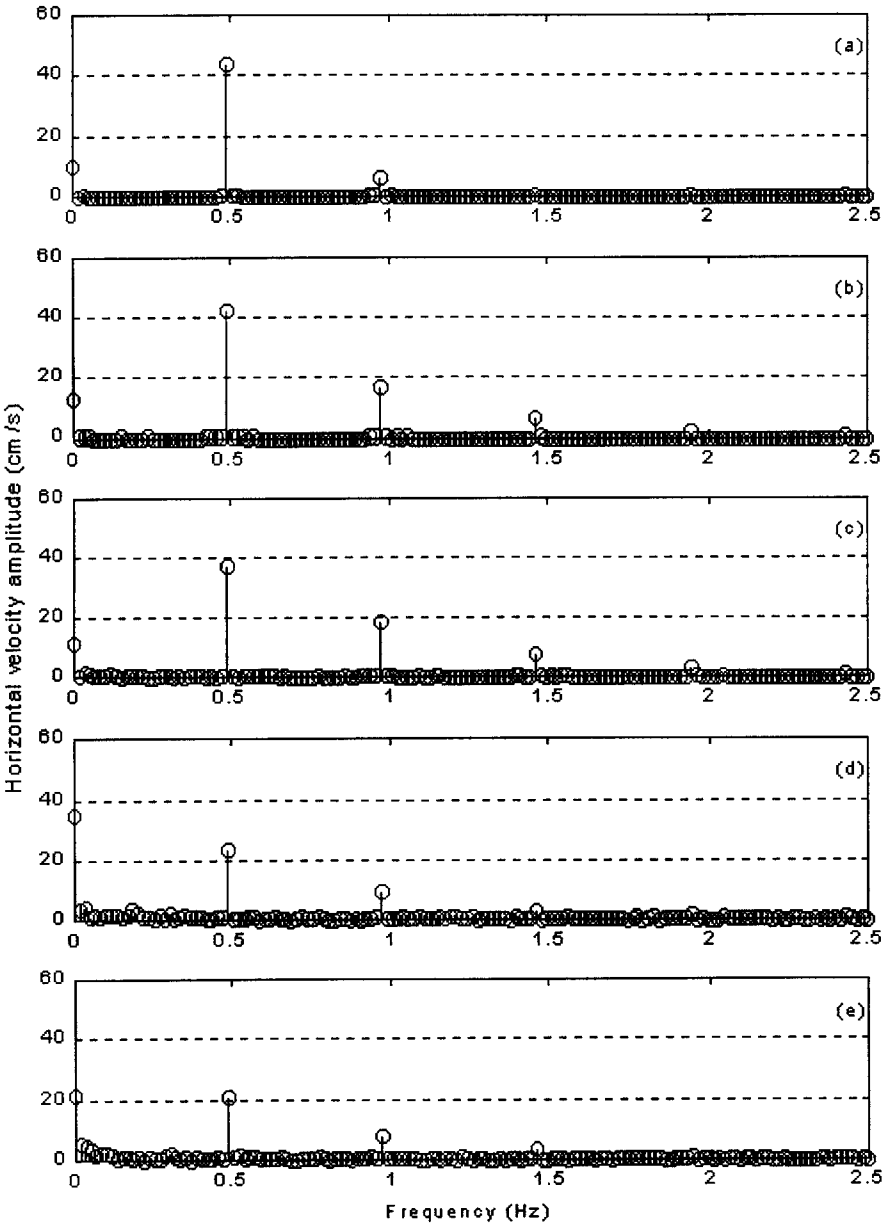

Figure 3-4 Horizontal velocity spectra; (a) x = 7.0 m, constant depth region; (b) x = 12.6 m, right before wave breaking; (c) x = 13.4 m, right after wave breaking; (d) x = 15.0 m, breaking zone; (e) x = 17.1 m, farther away from the breaking point. Note: Only the first 150 points are shown in the above spectra.

In the spectra of surface profile and velocity, it is noted how the second and higher harmonics grow relative to the first harmonic as breaking is approached. Shown in Figures 3-3 and 3-4, the first harmonic is dominant over other higher harmonics in the constant depth region (a), while the second and higher harmonics begin to show up and carry a larger portion of energy slightly before (b) and after (c, d and e) the breaking point, with the second harmonic amplitude being of the order of half of the first harmonic. Still, the strong periodicity of the records is demonstrated by the clear dominance of the harmonic components.

In addition to the harmonic components, the spectra show a zero frequency component, i.e., a constant. Half of this value represents a steady surface displacement or mean water level (MWL), $\bar{\eta}$, in Figure 3-3, and a mean current, $\bar{u}$, in Figure 3-4. The phase of $\bar{u}$ is always π, therefore the amplitude is that of a negative (seaward directed) current. The phase of $\bar{\eta}$, however, is either π or 0, corresponding to the wave set-down or set-up in Figure 3-3 (a, b and c) and (d and e), respectively. These shifts in the mean were also noted in the raw time series of $\eta(t)$ and $u(t)$ previously presented and discussed. Given the incident wave height $H \cong 20$ cm, period $T = 2.06$ s (radian frequency being $\omega = 3.05$ 1/s), and water depth $h = 50.0$ cm in the constant depth region, linear wave theory gives $kh = 0.75$ and the second order Stokes wave theory (Lecture notes of Basic Wave Theory, Madsen)

$$\bar{u} = -\frac{1}{8} H^2 \omega \frac{\coth kh}{h} \tag{3.2}$$

gives a return current of –5.1 cm/s which is in reasonable agreement with the measured mean current shown in Figure 3-4 (a). Notice that this absolute value is only growing

slightly from the constant depth part to the breaking point whereas it grows dramatically inside the surf zone reaching a value of -17.3 cm/s at x = 15.0 m and then decreases to about –11.0 cm/s at x = 17.0 m. This is the undertow created by the breaking waves.

3.3 Cross-shore variation of wave characteristics

We see from the frequency spectra (Figures 3-3 and 3-4) at each location that the first harmonic component of total (incident plus reflected) wave amplitude is dominant, i.e., the majority of the wave energy is carried by the first harmonic. The same conclusion holds true for the horizontal velocity. Although the amplitudes of the first harmonics A_1 and U_1, dominate in the frequency spectra, higher harmonics increase in the shore-ward direction, particularly as breaking is approached. Therefore, we define a representative energy wave amplitude A_e and the corresponding horizontal velocity amplitude U_e as

$$A_e = (\sum_{i=1}^{5} A_i^2)^{1/2} \tag{3.3}$$

$$U_e = (\sum_{i=1}^{5} U_i^2)^{1/2} \tag{3.4}$$

where A_i and U_i, $i = 1..5$, are the i th harmonic wave amplitude and horizontal velocity obtained directly from FFT of the wave record, respectively. Shown clearly in the frequency spectra, Figures 3-3 and 3-4, is the fact that the peaks are located almost exclusively at main harmonics, particularly in the first five harmonics, which means the energy values A_e and U_e are almost the same as RSS (Root of Sum of the Squares) values of surface displacement and horizontal velocity spectra, A_{RSS} and U_{RSS}, defined by

$$A_{RSS} = (\sum_{i=1}^{n} A_i^2)^{1/2} \tag{3.5}$$

$$U_{RSS} = (\sum_{i=1}^{n} U_i^2)^{1/2} \tag{3.6}$$

where n is the total number of points in the frequency spectra minus one (the *zero* th harmonic). However, for experiments in which the signals are not clearly periodic, the RSS values A_{RSS} and U_{RSS} may differ from A_e and U_e.

Rather than a spectrally determined amplitude, it is customary to define the wave amplitude and velocity amplitude based on the analysis of individual wave characteristics in the wave record, i.e.,

$$A_{wr} = \frac{1}{2n} \sum_{i=1}^{n} (\eta_{\max} - \eta_{\min})_i \tag{3.7}$$

$$U_{wr} = \frac{1}{2n} \sum_{i=1}^{n} (u_{\max} - u_{\min})_i \tag{3.8}$$

where $(\eta_{\max} - \eta_{\min})_i$ is the height measured from the i th crest to the following trough in the surface displacement record, $(u_{\max} - u_{\min})_i$ is the similar value calculated from the velocity record and n, set to 10 in our analysis, is the total number of waves in the calculation. These definitions are widely used by ocean engineers to get the wave height in the field and in laboratory research.

The variation of these measured wave characteristics along the wave channel is presented in Figures 3-5 and 3-6. As described in Chapter 2, the 1 on 10 beach slope starts at x = 9.5 m and ends at x = 10.6 m, after which the slope is 1 on 30.

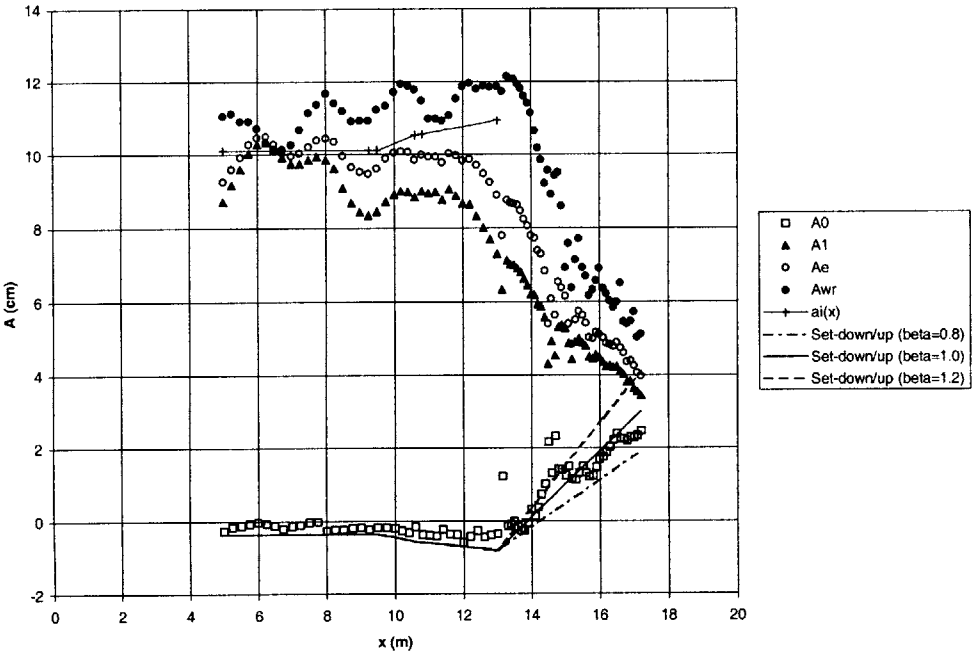

Figure 3-5 Cross-shore variation of wave amplitudes

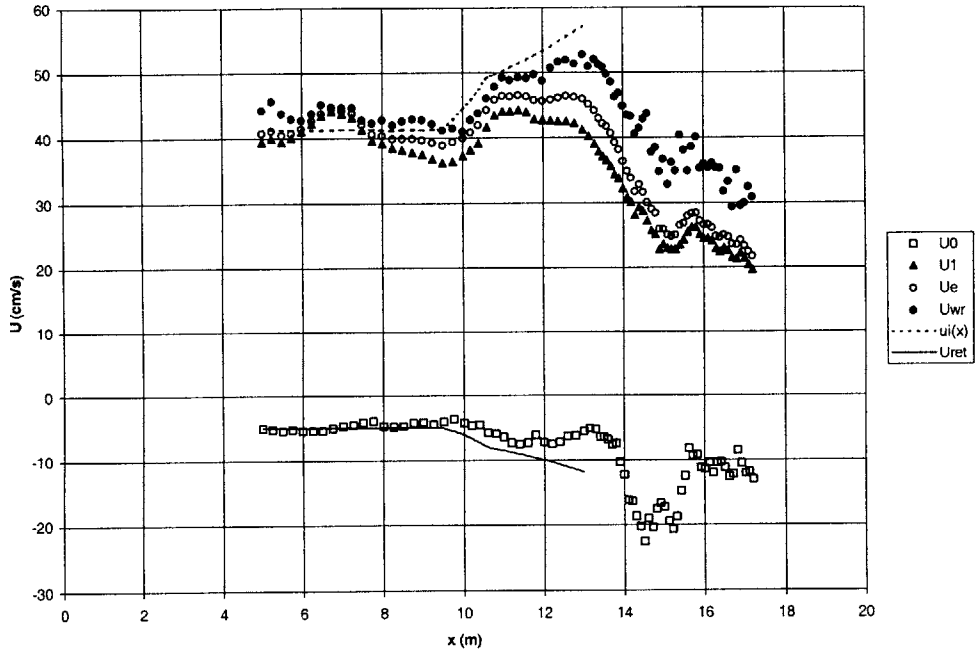

Figure 3-6 Cross-shore variation of horizontal velocities

Figure 3-5 shows the cross-shore variation of several representative values of wave amplitude in which A_0 is the wave set-down/set-up, A_1 is the first harmonic wave amplitude, A_e the energy surface amplitude, A_{wr} the wave record amplitude, and $a_i(x)$ is the predicted incident wave amplitude accounting for shoaling. Figure 3-6 shows the cross-shore variation of representative values of horizontal velocity in which U_0 is the wave-induced current, U_1 is the first harmonic horizontal velocity, U_e the energy velocity amplitude, U_{wr} the wave record velocity amplitude, U_{ret} the predicted return current, and $u_i(x)$ is the predicted first harmonic horizontal velocity of the incident wave accounting for shoaling.

It is noticed that A_1 and A_e are nearly the same in the constant depth portion as seen from Figure 3-3 (a), the frequency spectra, in which the second and higher harmonics are negligible small compared with the first harmonic component. A_1 and A_e start to deviate as waves climb the slope as seen from Figure 3-3 (b, c, d and e) in which higher harmonics begin to grow. U_1 and U_e in Figure 3-6 also exhibit the similar relation as A_1 and A_e. As we move from the constant depth region onto the slope, we see that record amplitude A_{wr} is 10% to 20% bigger than energy amplitude A_e, whereas U_{wr} is 10% to 25% larger than U_e. It is interesting to note that A_1 and A_e start dropping at about x = 11.9 m and U_1 and U_e start dropping at x = 13.0 m, whereas the waves were visually observed to break at x = 13.1 m. However, both A_{wr} and U_{wr} start decreasing at x = 13.1 m which agrees well with our experimental observation. This can be taken as the

first clear evidence that different definitions of wave amplitude and velocity used by various researchers can have considerable effects upon their conclusion regarding the location of the break point.

The constant depth portion's ($x < 9.5$ m) waviness of amplitude variation of A_i, A_e and A_{wr} is evidence of a small reflection. It is noticed that the constant depth part of A_{wr} curve has the wave length (beat length) of 2.1 m, being half the incident or reflected wave length, 4.2 m. The maximum amplitude appears around $x = 6$ m, $x = 8$ m and $x = 10$ m, and these locations correspond to minimum velocity amplitude although this is not very clear in Figure 3-6. Recalling the spatial analysis in Section 2.2.2, we find the maximum of the amplitude A in Equation (2.25) is roughly the incident wave amplitude a_i plus the reflected wave amplitude a_r, i.e., $A_{\max} \cong a_i + a_r$, and the minimum of A is $A_{\min} \cong a_i - a_r$, if the decay coefficients α and β are small. Therefore, an estimate can be made by taking the segment of the A_{wr} curve between $x = 8.0$ m and $x = 10.0$ m and the reflection coefficient is then $R \approx \dfrac{(A_{wr})_{\max} - (A_{wr})_{\min}}{(A_{wr})_{\max} + (A_{wr})_{\min}} = \dfrac{12.0 - 11.0}{12.0 + 11.0} = 4.3\% << 1$, as one would expect.

It was observed during the experiment that the waves broke at $x = 13.1$ m as spilling breakers. Galvin (1968) gave a parameter for classifying breaker type

$$B_0 = \frac{H_0}{L_0 (\tan\alpha)^2} \tag{3.9}$$

where H_0/L_0 is the deep water wave steepness and $\tan\alpha$ is the beach slope. Galvin (1968) found that spilling breakers occurred for $B_0 > 4.8$. Given wave period T = 2.06 s, deep water wave length is $L_0 = gT^2/2\pi$ = 6.6 m and the group velocity is $C_{g0} = gT/4\pi$ = 160.8 cm/s. With incident and reflected wave amplitudes resolved from temporal analysis described in Section 2.2.1, the incident wave amplitude in the constant depth region, a_{ic} = 9.7 cm (subscript "c" denoting constant depth), is taken as the average within the beat length from x = 6 m to x = 8 m. The dispersion relationship (2.3) is used to calculate the wave number k and the group velocity is given by linear theory

$$C_g = \frac{\omega}{2k}\left(1 + \frac{2kh}{\sinh 2kh}\right) \tag{3.10}$$

With still water depth h_c = 50.0 cm, the group velocity C_{gc} = 173.7 cm/s in constant depth portion. The deep water wave height is $H_0 = H_{ic}\sqrt{C_{gc}/C_{g0}}$ = 20.3 cm where the incident wave height $H_{ic} = 2a_{ic}$ = 19.3 cm/s. With $\tan\alpha$ = 1/30 in our experiments, B_0 turns out to be 27.7, indicating the breaker type of spilling, in agreement with the observation.

The incident wave amplitude due to pure shoaling, $a_i(x)$ can be predicted using linear theory

$$a_i(x) = a_{ic}\sqrt{C_{gc}/C_g(x)} \tag{3.11}$$

and is shown in Figure 3-5. The corresponding horizontal velocity amplitude is then calculated using

$$u_i(x) = \frac{a_i(x)\omega}{\sinh kh} \tag{3.12}$$

and shown in Figure 3-6. Both of the curves terminate at the observed breaking point, x = 13.1 m.

The mean water level, $\overline{\eta}$, mentioned in Section 3.2, the wave set-up/set-down in Figure 3-5, A_0, is half the *zero* th harmonic of surface spectra. Outside the surf zone, the wave set-down can be predicted using the formula given by Svendsen and Jonsson (1976) under the assumption of no energy dissipation

$$\overline{\eta} = -\frac{H^2}{16h} \cdot \frac{2kh}{\sinh 2kh} \tag{3.13}$$

where $H = 2a_i(x)$ is the predicted incident wave height obtained from (3.11). Inside the surf zone, Svendsen and Jonsson (1976) give the slope of the mean water surface as approximately proportional to the bed slope

$$\frac{d\overline{\eta}}{dx} = \frac{3\beta^2/8}{1+3\beta^2/8}\tan\alpha \tag{3.14}$$

in which $\frac{d\overline{\eta}}{dx}$ is the slope of the mean water surface, $\tan\alpha$ is the gentle bed slope, $\beta = \frac{H}{h}$ is the ratio of wave height to water depth and assumed to be constant within surf zone (Note: this β is not the decay coefficient associated with reflected waves discussed in Section 2.2.2). The "constant" β is of the order of 1 and is about 0.8 for spilling breakers. However, Bowen et al. (1968) have shown good agreement with (3.13) for mean values of β across the surf zone higher that 1.2. Thus, the three lines in Figure 3.5

give the prediction of wave set-down/up for $\beta = 0.8$, 1.0 and 1.2 respectively, in which the $\beta = 1.0$ line agrees reasonably well with the present measurements.

The return current is calculated using Equation (3.2) with $H = 2a_i(x)$ and is shown in Figure 3-6 for comparison with the measured values. The predicted return current agrees well with observations up to the slope ($x = 9.5$ m) and then starts to deviate from the measurement. The undertow created by breaking waves is clearly seen in the region from $x = 13.3$ m to $x = 16.0$ m. There is a transition from $x = 13.1$ to $x \cong 14.5$ m over which the undertow strengthens to reach its maximum value of about 20 cm/s in the seaward direction. Beyond this point the undertow decreases in strength as a result of the decreased wave height.

Again, we notice that the first harmonic component is dominant over the higher harmonics, resulting in A_1 and U_1 being fairly close to A_e and U_e, respectively. Thus we can safely employ only the first harmonics to come up with the incident, reflected wave characteristics and reflection coefficients using the temporal analysis discussed in Section 2.2.1. Since the reflection is so small, we are unable to get anything meaningful from the spatial analysis discussed in Section 2.2.2. The cross-shore variation of incident wave amplitude, reflected wave amplitude and reflection coefficients, resolved solely from the first harmonic components of surface displacement and horizontal velocity following the data analysis procedure described in Section 2.2.1, are shown in Figure 3-7, 3-8 and 3-9, respectively.

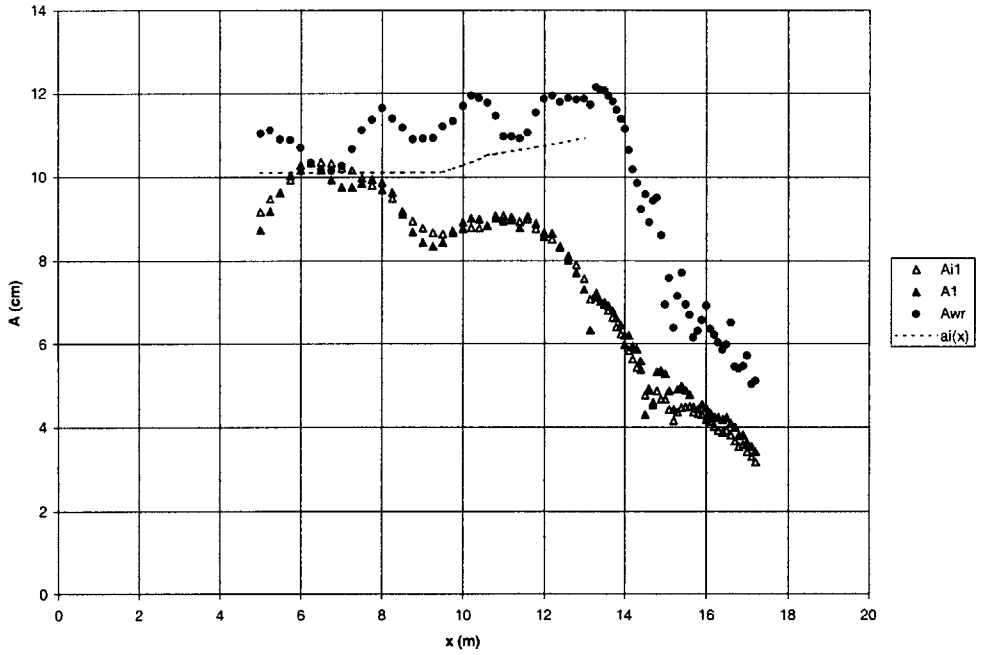

Figure 3-7 Cross-shore variation of incident wave amplitude, A_{i1}

The incident wave amplitude, A_{i1}, obtained from the temporal analysis of the first harmonic component, is shown in Figure 3-7. For comparison the total first harmonic amplitude A_1 and the wave record amplitude A_{wr} are also presented in Figure 3-7. The A_{i1} curve is very close to A_1, which shows that the reflected waves are indeed very small. The incident first harmonic amplitude drops at x = 11.2 m, well before the visually observed location of breaking. At x = 13.15 m which is right after the visually observed breaking point x = 13.1 m, the A_1 curve shows a dramatic drop from 7.3 cm to 6.3 cm. This feature is not present in either A_{i1} or A_{wr} curve. It is important to notice the big difference in predicted wave amplitude and the actual value at x = 13.0 m, just before the break point: the predicted incident wave amplitude gives 10.9 cm, while the measured value is only 7.3 cm. The discrepancy is even greater if the measured first harmonic incident amplitude is compared with the wave record amplitude A_{wr}.

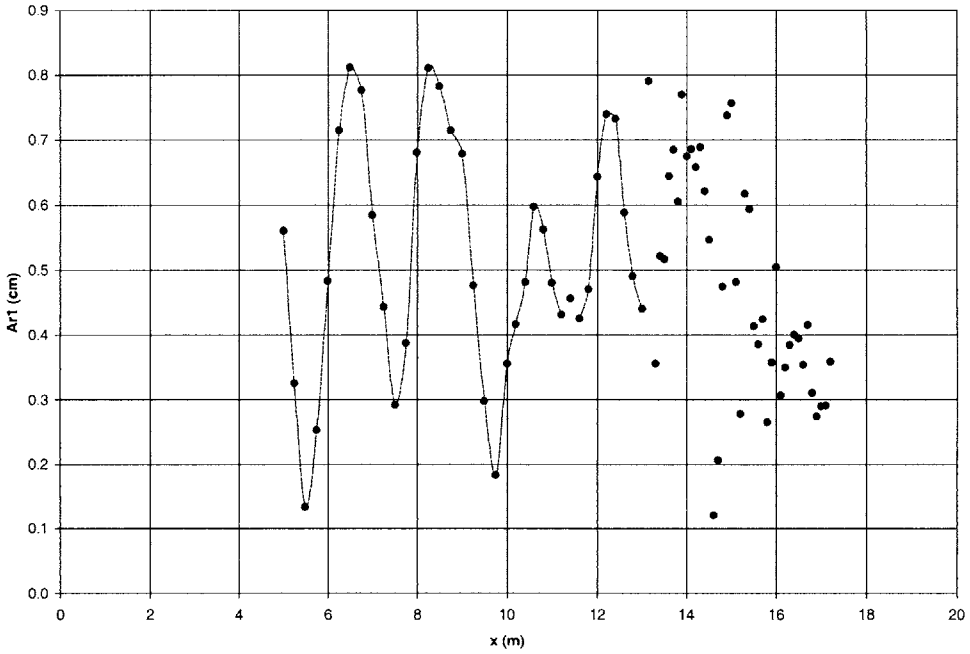

Figure 3-8 Cross-shore variation of reflected wave amplitude, A_{r1}

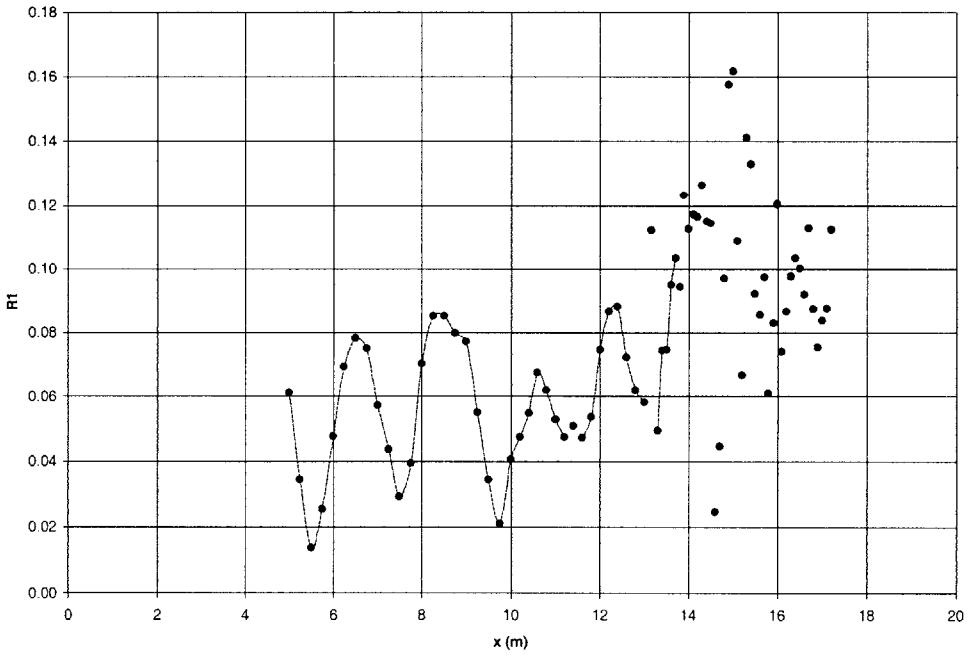

Figure 3-9 Cross-shore variation of reflection coefficients, $R_1 = A_{r1} / A_{i1}$

Figure 3-8 shows the variation of the first harmonic reflected wave amplitude as obtained from the temporal analysis of the measurements. The amplitude of A_{r1} is roughly 0.4 cm, so with $A_{i1} \cong 10$ cm, the reflection coefficient $R \cong 0.04$, in reasonable agreement with the value (4.3%) obtained from the raw data of A_{wr}. The variation of the first harmonic reflection coefficient, $R_1 = a_{r1} / a_{i1}$, is shown in Figure 3-9. The small reflection coefficient fluctuates by ± 0.03 around the mean value of 0.05 in the constant depth region, while this average goes up to 0.10 after wave breaking, largely due to the decrease in incident wave amplitude and the near-constancy of the reflected wave amplitude.

An interesting phenomenon exhibited by Figures 3-8 and 3-9 is that the reflected wave amplitude shows some kind of organized waviness (see the dotted line) from the constant depth part up to the break point, with a wave length of roughly half the local wave length, i.e., similar to the beat length. However, there is no systematic variation inside the surf zone. The phenomenon might be explained in a paper written by Madsen, et al. (1970). When two crests of waves propagating in the same direction are superimposed, the resulting surface wave amplitude is decreased, i.e., superposition is not valid. This may be explained by considering the wave crest of one wave being superimposed on the "current" associated with the crest of the other wave. When the "current" is following the wave, its amplitude decreases. If this is applied to the situation when one wave is reflected (small) and the other is incident (large), then the small reflected wave should increase its amplitude when it is superimposed on an opposing current associated with the crest of an incident wave. Thus, reflected wave amplitude should increase at locations of

antinodes in the partially standing wave formed in the constant depth region. The observation that the antinodes around x = 8 m and x = 10 m (see Figure 3-7) essentially coincide with the locations where A_{r1} reaches maximum in Figure 3-8 lends some credibility to this conceptual explanation of the systematic variation of A_{r1} and R_1.

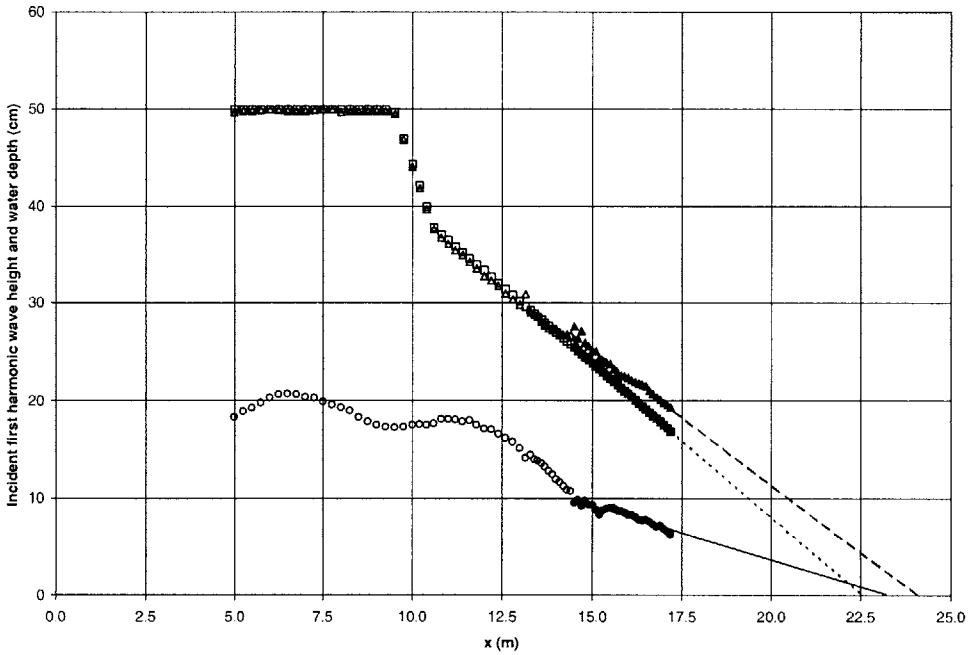

Figure 3-10 Variation of water depth and incident wave height; the triangles stand for still water depth plus set-up $h_+ = h + A_0$; the squares being the still water depth h; the circles being the incident first harmonic wave height H_{i1}; and the full symbols for data well beyond the break point (x > 14.5 m)

It is often used that wave breaking occurs in shallow water when H/h reaches a certain limit. This breaking ratio is often assumed to hold in the surf zone, i.e., for a beach of constant slope the wave height is assumed to vary linearly with location in the surf zone.

If we plot the water depth together with the incident wave height as in Figure 3-10, we find that the best straight line fit of $(H_{i1})_{B+}$, the incident wave height well beyond breaking denoted by the subscript "B+", intersects with the x-axis at $x = 23.33$ m. The linearity of the data can be evaluated by the R^2 value ($R^2 = 1$ meaning absolutely linear), defined as

$$R^2 = 1 - \frac{SSE}{SST};\ SSE = \sum_{i=1}^{n}(Y_i - \hat{Y}_i)^2,\ SST = (\sum_{i=1}^{n} Y_i^2) - \frac{(\sum_{i=1}^{n} Y_i)^2}{n} \tag{3.15}$$

in which Y_i is the real data point, $\hat{Y}_i$ is the anticipated value obtained from the linear relationship at the same "x" location as Y_i, and n is the total number of data points used in the linear fit. While the fit of $(H_{i1})_{B+}$ gives $R^2 = 0.915$, the water depth including set-up $(h + A_0)_{B+}$ and without set-up $(h)_{B+}$ best fit lines cross the x-axis at $x = 24.10$ m ($R^2 = 0.977$) and $x = 22.56$ m ($R^2 = 0.998$), respectively. The reasonable good linear fit to the wave height variation within the surf zone, shown by R^2 close to 1, is in general agreement with the previously mentioned rule of H/h = constant in the surf zone. It is pointed out, however, that this trend is obtained from data well within the surf zone ($x >$ 14.5 m) and does not apply for the entire surf zone ($x > 13.1$ m).

To make this point more clearly, Figure 3-11 shows the variation of incident first harmonic wave height $H_{i1} = 2a_{i1}$ non-dimensionalized by the total water depth, i.e., still water depth plus set-up, $h_+ = h + A_0$. In Figure 3-11, we establish a different horizontal axis, "X", with zero at $x = 24.10$ m, the intersection of mean water level and the beach, and positive direction seaward, i.e., $X = 24.10 - x$. The X-axis is then non-

dimensionalized by the position of the visually observed breaking point X_B = 11.0 m (x_B = 13.1 m). The total first harmonic wave height $H_1 = 2A_1$, the energy wave height $H_e = 2A_e$ and the wave record wave height $H_{wr} = 2A_{wr}$ normalized by the total water depth h_+, are also plotted in Figure 3-11 for comparison.

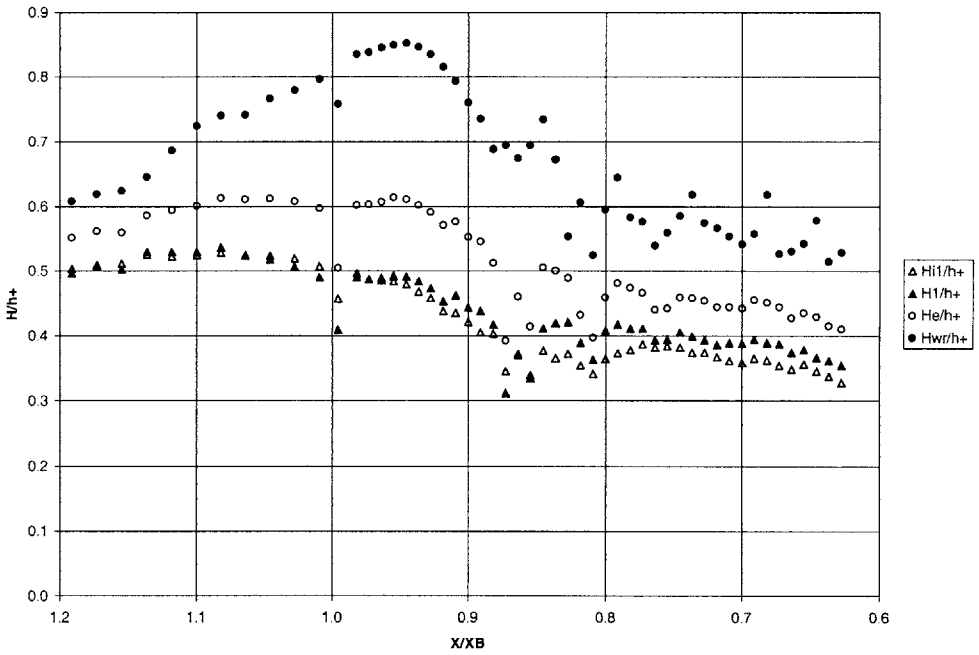

Figure 3-11 Cross-shore variation of wave height non-dimensionalized by the total water depth $h_+ = h + A_0$

It is noticed that H_1 / h_+, H_e / h_+ and H_{wr} / h_+ curves all reach a maximum at X / X_B = 0.95 corresponding to x = 13.7 m. It therefore seems reasonable to question if the breaking point actually is located x = 13.1 m, as visually observed. With a "corrected" breaking point x_{1B} = 13.7 m, or X_{1B} = 10.4 m, the variation of H / h_+ is redrawn in Figure 3-12.

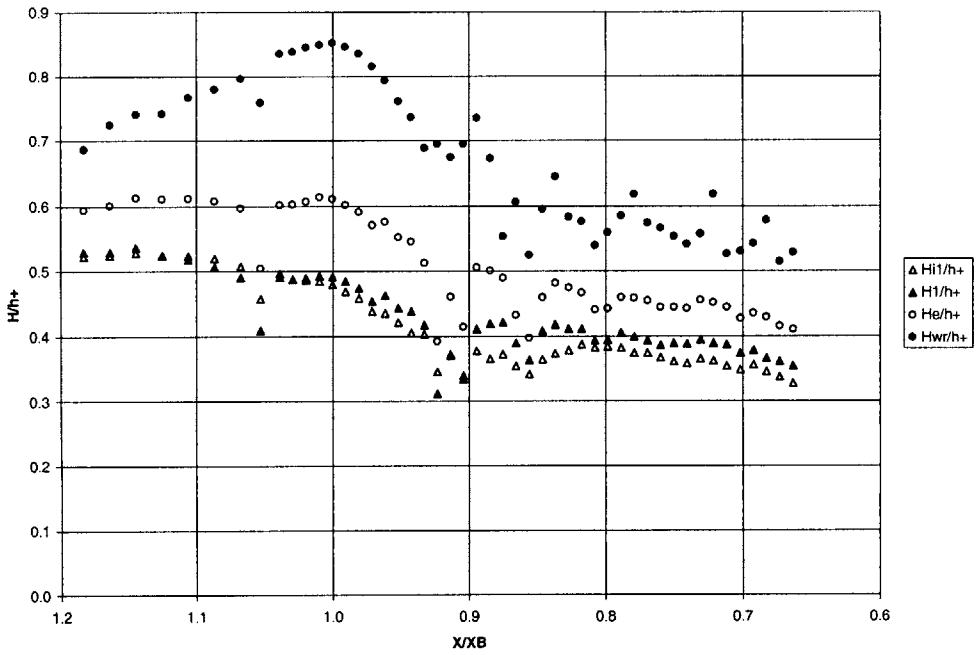

Figure 3-12 Cross-shore variation of wave height with "corrected" breaking point; h_+ is the total water depth

It is obvious that H_{wr}/h_+ and H_e/h_+ climb to maxima as the "corrected" break point is approached, whereas the H_1/h_+ curve reaches a very weak local maximum. The values of H/h_+ in the vicinity of the break point are of definite interest. If the record wave height H_{wr} is used for H, $(H/h_+)_B = 0.85$ is obtained at breaking, denoted by the subscript "B". This value is in good agreement with the widely used criterion of wave breaking, $(H/h_+)_B = 0.8$. However, non-dimensional energy wave height $(H_e/h_+)_B$, first harmonic total wave height $(H_1/h_+)_B$ and first harmonic incident wave height $(H_{i1}/h_+)_B$ give 0.61, 0.49 and 0.48, respectively, which all are substantially lower than the commonly used value of 0.8. The predicted non-dimensional incident wave height

$(H_i(x)/h_+)_B = 0.78$ with $H_i(x)_B = 2a_i(x)_B = 22.1$ cm (see Figure 3-7). This is the second time we see that different results are obtained from different definitions of wave height. After the break point, H_{wr}/h_+ drops dramatically from the peak value of 0.85 within a distance of about 1.5 m and then remains approximately constant at a value of $H_{wr}/h_+ \cong 0.56$. Examination at the H_e/h_+, H_1/h_+ and H_{i1}/h_+ shows variation, but they all exhibit similar features to H_{wr}/h_+ with near-constant values of 0.44, 0.39 and 0.36, respectively following an initial drop after the break point.

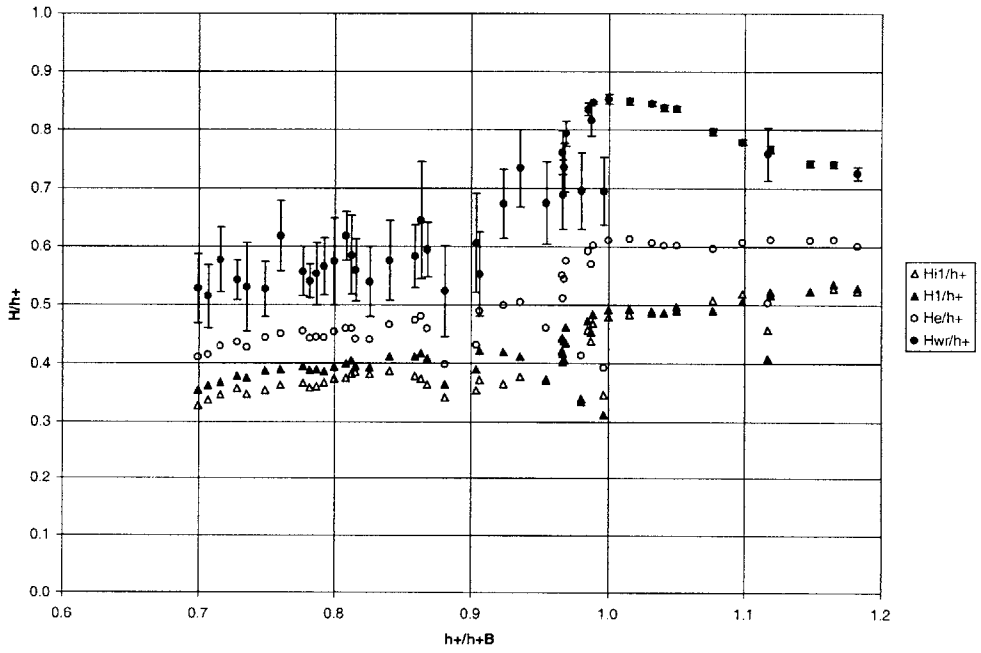

Figure 3-13 Wave height variation with total water depth

In Figure 3-13, the vertical axis shows wave height non-dimensionalized by the total water depth, and the horizontal axis is the water depth non-dimensionalized by that of the "corrected" breaking point $h_{+B} = 27.68$ cm at $x_B = 13.7$ m. The solid circle on the H_{wr}/h_+ curve is plotted using the mean value of 10 successive wave heights obtained

from the wave record divided by the total water depth. The error bars show the standard deviation of these 10 wave heights over total water depth. In the surf zone, the wave record is somewhat difficult to measure as we discussed in the previous Section 3.2, and this is reflected in the relatively large variability of the H_{wr}/h_{+} values beyond breaking, i.e., when $h_{+}/h_{+B} < 1.0$.

It is noticed that the measurements ended at x = 17.2 m and did not go further into the surf zone because the results here will be compared with the experiments in which the seawall is located at x = 17.8 m. The experimental results with extensive surf zone measurements are presented in the Appendix A.

Experimental results without a seawall on the beach are used to obtain baseline data on incident wave energy dissipation in the absence of a reflective structure. Subsequent chapters present experimental results for which seawalls are either vertical (Chapter 4) or sloped (Chapter 5).

Chapter 4

Experimental Results in the Presence of Vertical Seawalls

4.1 Overview of experiments

Two sets of experiments, one with non-breaking waves and the other with breaking waves, were carried out in the presence of a vertical seawall, whose toe is located at x = 17.8 m. As described in Chapter 2, the 1 on 10 slope starts from x = 9.5 m and ends at x = 10.6 m, beyond which point the beach slope is 1 on 30. The non-breaking wave experiments provide the reflection coefficient of the highly reflecting structure, whereas the breaking wave experiments give the incident and reflected wave characteristics due to breaking, which is the goal of the present research. In both experiments, the wave maker was run 15 minutes in order for stationarity to be established before measurements were taken. The experimental results are shown in the following sections 4.2 (non-breaking waves) and 4.3 (breaking waves), respectively.

4.2 Non-breaking wave experimental results

In the non-breaking wave experiments, the wave period was 2.10 seconds and the water depth in the constant depth region was 48.5 cm. The wave height was kept small (incident wave height being roughly 2.4 cm in the constant depth region) so that the waves did not break at any point along the flume. A three-minute record of both water surface displacement and velocity was taken at 77 locations from x = 5.0 to x = 17.2 m. The measuring interval in the constant depth region was 25 cm, while it shortened to 20 cm on the slope, and 15 cm near the toe of the seawall, respectively. Because the friction introduced by the rubble glued to the seaward side of the reflective structure dissipates a small portion of the incident wave energy, we would expect a reflection coefficient to be less than but close to unity.

4.2.1 Wave records and frequency spectra

The wave record is very periodic throughout the wave channel, even on the slope and near the toe of the structure. The wave records and frequency spectra shown in Figure 4-1 are from x = 15.1 m which is on the 1 on 30 slope. The periodicity is obvious in both surface profile and velocity records, with each wave being virtually identical to its neighbors. The surface displacement (b) and horizontal velocity (d) spectra show that the first harmonic is dominant over higher harmonics.

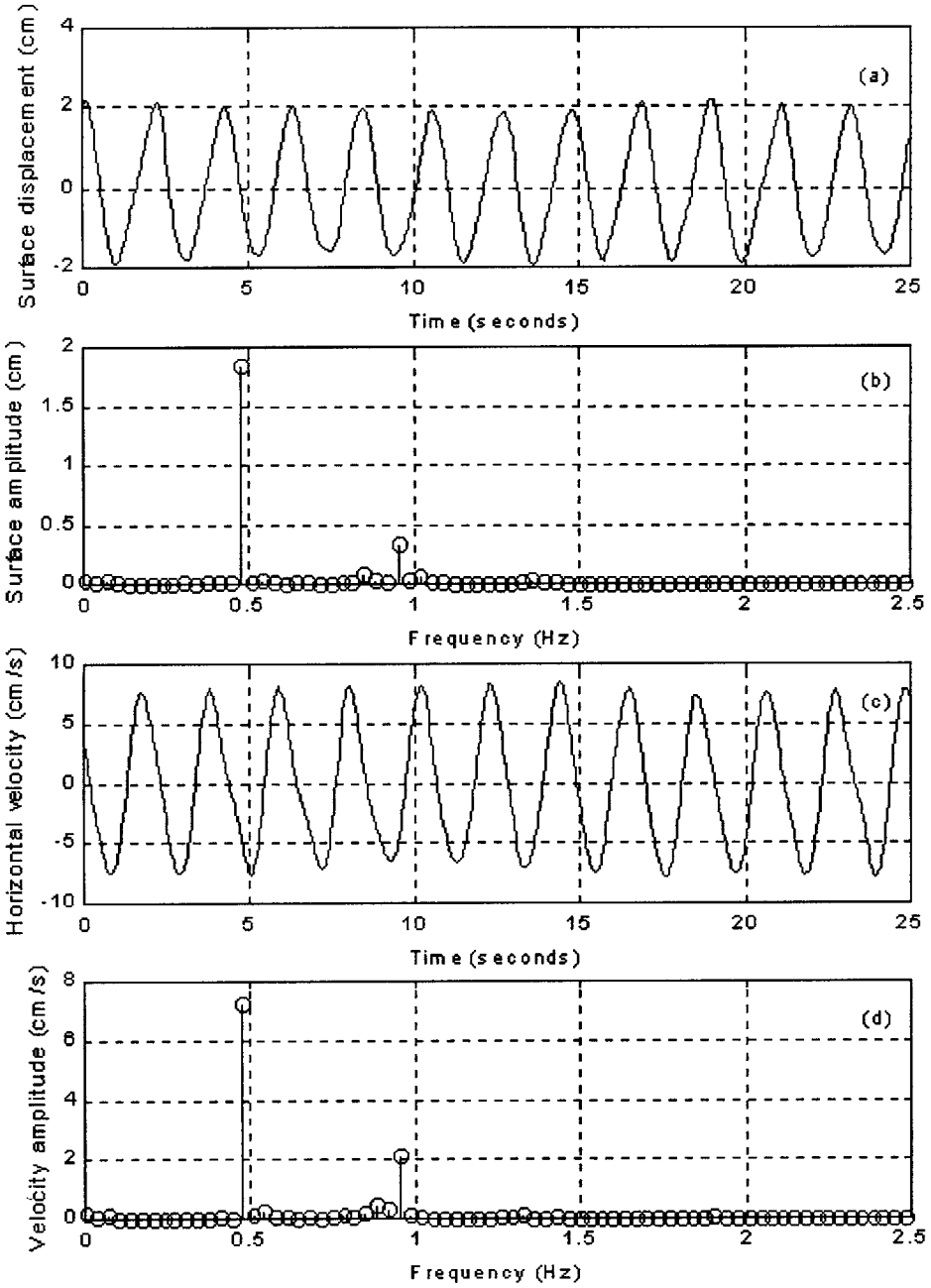

Figure 4-1 Wave records and frequency spectra at x = 15.1 m; (a) surface displacement record $\eta(t)$, (b) surface displacement spectrum, (c) horizontal velocity record $u(t)$, (d) horizontal velocity spectrum. Note: only the first 74 points are shown in the spectra.

We also see from the *zero* th harmonics in (b) and (d), i.e., twice the mean of $\eta(t)$ and $u(t)$, that the wave set-down and the return current are both very small which is also reflected in the wave records (a) and (c), respectively. The incident wave height at x = 15.1 m is H = 2.6 cm, calculated using the temporal analysis presented in Section 2.2.1. Given T = 2.1 s and h = 21.7 cm, linear wave theory gives kh = 0.46 and the second order Stokes wave theory (3.2) gives an incident wave return current of -0.06 cm/s which is in agreement with the observation from (d).

4.2.2 Cross-shore variation of wave characteristics

Figure 4-2 shows the variation of wave amplitudes in which A_0 is the wave set-down/set-up, A_1 is the first harmonic wave amplitude, and A_{wr} is the record wave amplitude.

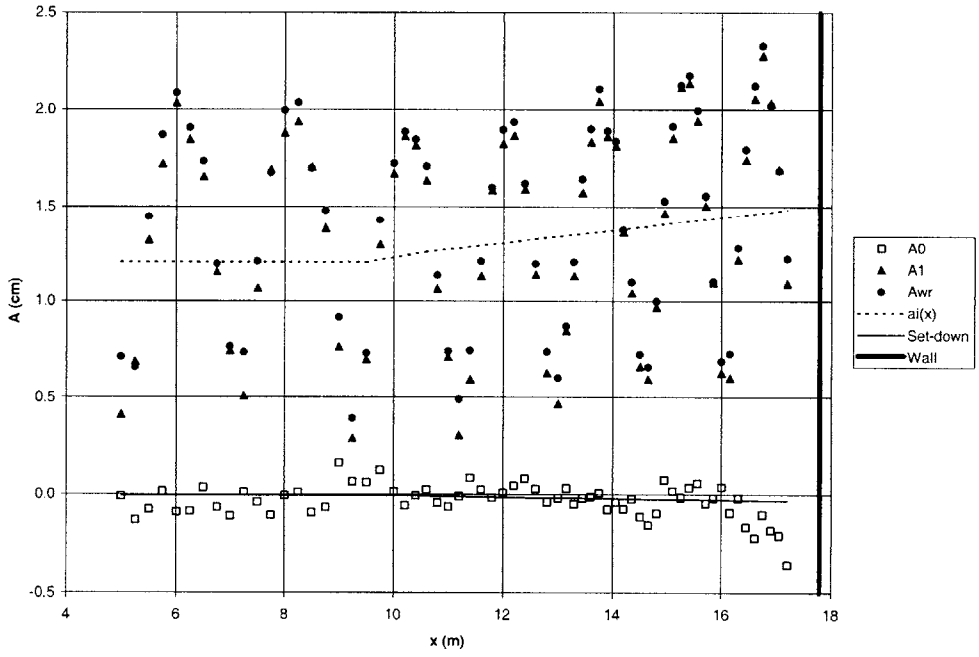

Figure 4-2 Cross-shore variation of wave amplitudes

Figure 4-3 shows the variation of horizontal velocities in which U_0 is the return current, U_1 and U_{wr} are the corresponding values to A_1 and A_{wr}, respectively.

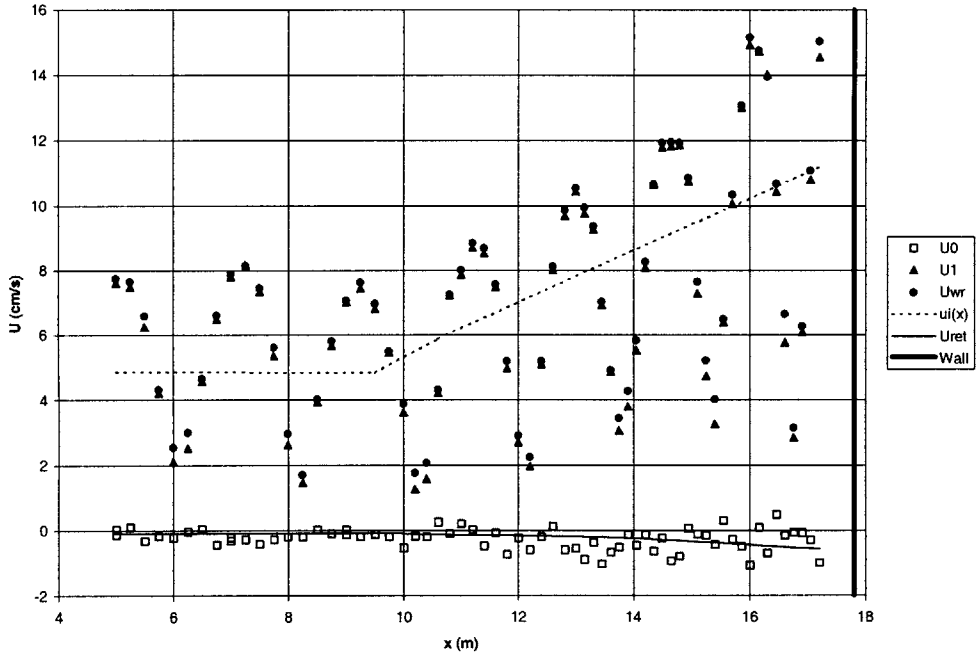

Figure 4-3 Cross-shore variation of horizontal velocities

As A_e is very close to A_1 which can also be seen from the spectrum in Figure 4-1 (b), only the first harmonic wave amplitude A_1 is shown in Figure 4-2 along with the record wave amplitude A_{wr} (otherwise A_e will overlap A_1). Similarly, only U_1 is shown together with U_{wr} in Figure 4-3.

The clear waviness of A_1 throughout the wave channel is strong evidence of reflection, with the average remaining nearly constant in the constant depth region and increasing on the slope. The maximum wave amplitude in Figure 4-2 appears around x = 6 m, x = 8.25 m and x = 10.2 m, and these locations correspond to minimum velocity amplitude

in Figure 4-3. An estimate of reflection coefficient in the constant depth region can be made by taking the segment of the A_1 curve between $x = 6$ m and $x = 8.25$ m, that is

$$R \approx \frac{(A_1)_{\max} - (A_1)_{\min}}{(A_1)_{\max} + (A_1)_{\min}} = \frac{2.0 - 0.5}{2.0 + 0.5} = 60\%.$$

For comparison, the incident wave amplitude accounting for shoaling, $a_i(x)$, is predicted using (3.11) and shown in Figure 4-2, with the constant depth portion's incident wave amplitude being the average obtained from temporal analysis (refer to Section 2.2.1) within the beat length from $x = 6$ m to $x = 8.25$ m, i.e., $a_{ic} = 1.21$ cm. Given the wave period $T = 2.10$ s and the still water depth in the constant depth region $h_c = 48.5$ cm, linear theory gives the group velocity in the constant depth region $C_{gc} = 174$ cm/s. C_{gc} and a_{ic} are then used in (3.11) to calculated the incident wave amplitude on the slope due to shoaling. The corresponding horizontal velocity amplitude $u_i(x)$ is calculated using (3.12) and shown in Figure 4-3. Seen from Figure 4-2, $a_i(x)$ is virtually in the center of the A_1 curve, however, $u_i(x)$ appears to be slightly higher than the average line of U_1.

Obtained from (3.13), the predicted incident wave set-down is also shown in Figure 4-2, which is fairly close to the measured values despite the small undulation of A_0 caused by reflection. The predicted incident wave return current U_{ret} obtained from (3.2) is shown in Figure 4-3. Again, the predicted and measured values are in good agreement in the constant depth region and a larger discrepancy appears on the 1 on 30 slope, which starts at $x = 10.6$ m, with a reflection-associated waviness of the measured values.

As the first harmonic component is dominant over the higher harmonics, we only use the first harmonic components in the following temporal and spatial analyses (described in Sections 2.2.1 and 2.2.2, respectively) to resolve the incident and reflected wave characteristics and these results are presented in Section 4.2.3.

4.2.3 Cross-shore variation of incident and reflected wave characteristics and reflection coefficient

Figure 4-4 shows the spatial curve fitting of the first harmonic wave amplitude variation, in which the circles in the figure stand for the measured values and the solid line is the fitted curve obtained using the methodology presented in Section 2.2.2.

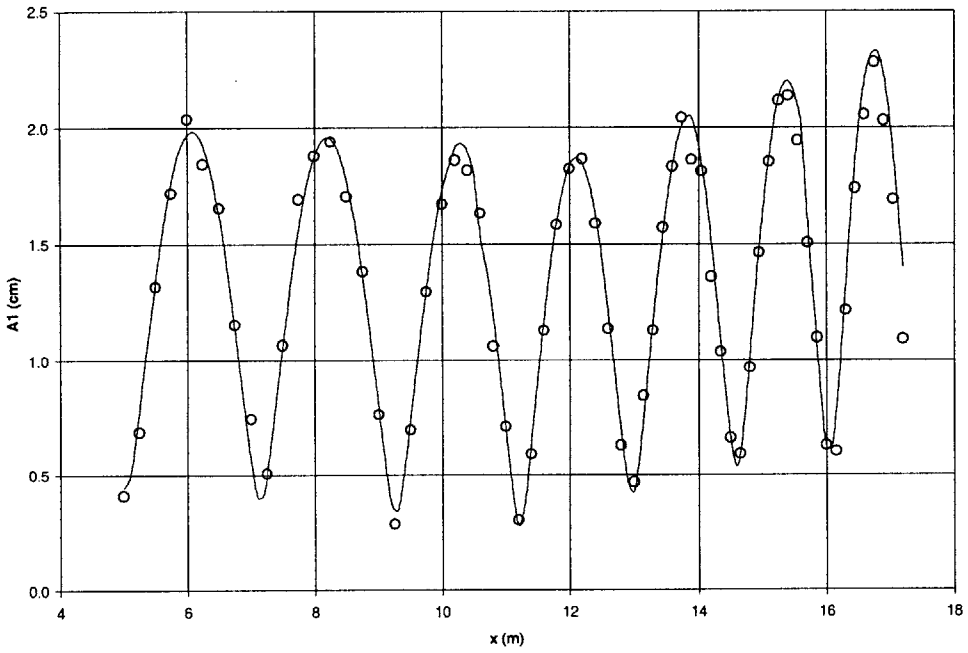

Figure 4-4 Spatial curve fitting of first harmonic wave amplitude

The resolved incident and reflected wave amplitudes from temporal (Section 2.2.1) and spatial (Section 2.2.2) analyses are shown in Figures 4-5 and 4-6, respectively. For comparison, the predicted incident wave amplitude accounting for pure shoaling, $a_i(x)$, and the first harmonic wave amplitude, A_1, indicated by the faint dotted line, are also presented in Figure 4-5.

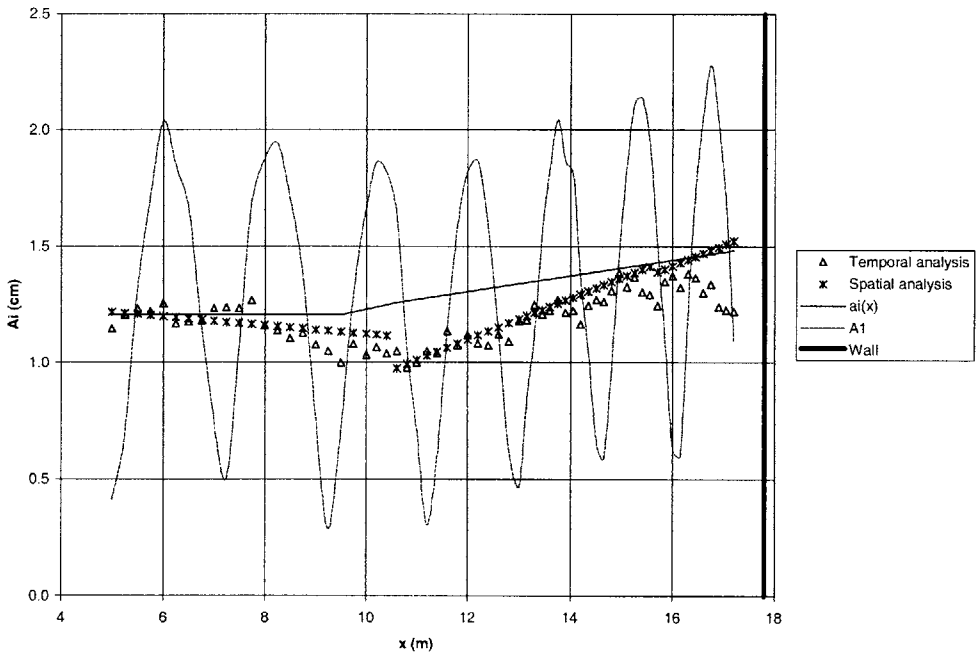

Figure 4-5 Cross-shore variation of incident wave amplitude

It is noticed that the incident wave amplitudes resolved from spatial analysis and temporal analysis are in excellent agreement, both decaying in the constant depth region and then increasing on the slope. However, there is a discrepancy between predicted incident wave amplitude $a_i(x)$ and the resolved incident wave amplitudes from x = 12 m to x = 14 m on the slope. The spatial line (denoted by "*") is obvious in the center of A_1 curve, which is expected.

The incident wave height in the constant depth region is about H = 2.4 cm as seen from Figure 4-5. Given the still water depth h = 48.5 cm in the constant depth region and wave period T = 2.10 s, linear wave theory gives the wave length L = 425 cm. The Ursell parameter is then $U = HL^2/h^3$ = 3.8, indicating that linear theory can be applied with reasonable accuracy.

The reflected wave amplitude (Figure 4-6), despite the variability, remains nearly constant (about 0.8 cm) in the constant depth region and starts to climb from x = 14 m up to x = 17.2 m. Again, the spatial and temporal analyses yield results in close agreement.

For comparison, the predicted reflected wave amplitude accounting for shoaling,

$$a_r(x) = a_{rc}\sqrt{C_{gc}/C_g(x)} \tag{4.1}$$

is also shown in Figure 4-6 in which a_{rc} and C_{gc} are the constant depth portion's reflected wave amplitude and group velocity, respectively, and $C_g(x)$ is the local group velocity as in (3.11). The average of the constant depth portion's reflected wave amplitude from x = 6.5 m to x = 8.75 m, a_{rc} = 0.80 cm, is taken as the base for the amplitude prediction on the slope. C_{gc} is equal to 174 cm/s as previously presented in this chapter. Although some discrepancy between $a_r(x)$ and measurements is noticed on the slope, the predicted and measured values on the slope differ no more than about 15%, which is considered acceptable.

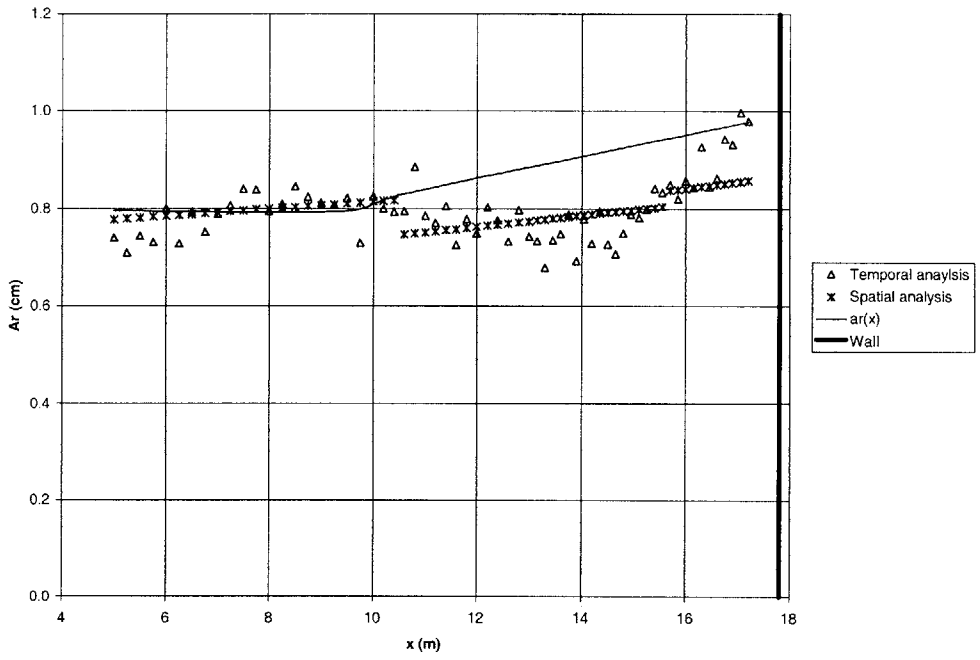

Figure 4-6 Cross-shore variation of reflected wave amplitude

Figure 4-7 shows the variation of reflection coefficients. Ideally, the reflection coefficient $R = a_r(x)/a_i(x) = a_{rc}(x)/a_{ic}(x)$ = 0.67 = constant since shoaling affects the incident wave a_i and reflected wave a_r in the same manner. With the incident and reflected wave amplitudes resolved from spatial and temporal analyses being close to each other, respectively, the good agreement of reflection coefficients from both analyses is therefore expected. Despite the variability, the reflection coefficient remains nearly constant around 0.7, which as anticipated is close to unity. Full reflection is not expected because of the friction introduced by the rubbles on the reflecting structure as discussed previously in this chapter. However, the value of 0.7 is surprisingly low and it is conceivable that leakage around the slope may have contributed to the small value of R.

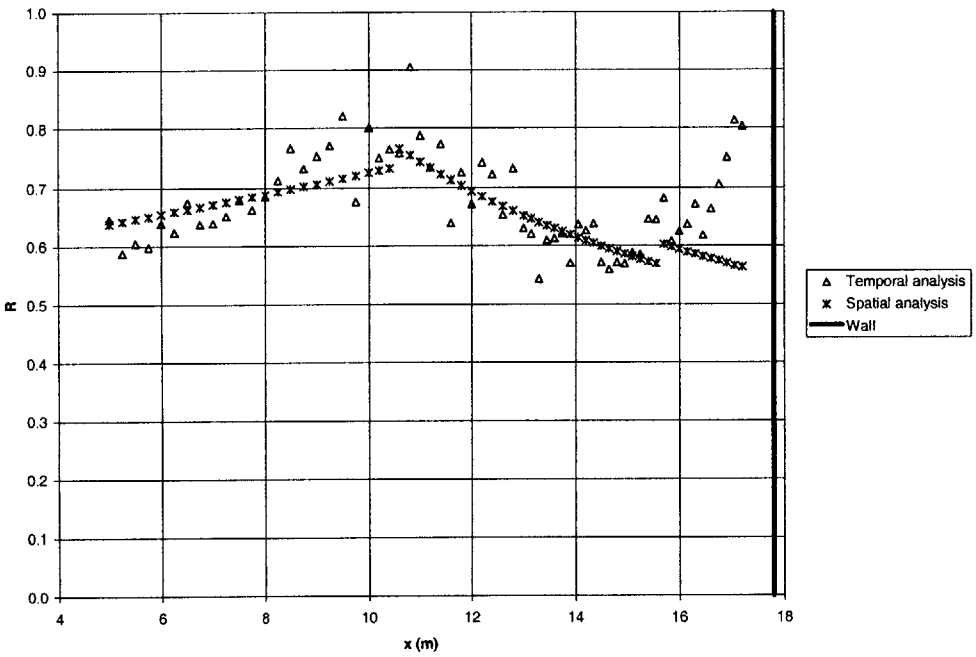

Figure 4-7 Cross-shore variation of reflection coefficient

4.3 Breaking wave experimental results

In the breaking wave experiments, the wave period is 2.03 seconds and the water depth in the constant depth region is 46 cm. The breaking of the waves occurred visually around x = 11.8 m and the breaker can be classified as the spilling type. The breakers tend to overshoot and are more violent than those in the no-structure experiments because of the considerable reflection. With reflection clearly evident, the incident wave height in the constant depth region is about 20 cm, which is about the same as the value for the no-wall breaking wave experiments. Therefore, the results here should be directly comparable with the no-wall breaking result. The measurements were taken at the same locations as in the non-breaking wave experiments. At each station, a three-minute record of both surface displacement and velocity was taken.

4.3.1 Wave records and frequency spectra

The wave records are quite periodic although the waves are non-linear. It is of interest to examine the surface displacement and horizontal velocity immediately after the break point, which is from x = 12.2 m (right after breaking) and shown in Figure 4-8.

Figure 4-8 (a) depicts the time series of the surface displacement, from which periodicity is obviously seen. However, there are other frequency components contained in the record, as we can see from the spectrum (b). Similar phenomena are present in the horizontal velocity record (c) and the corresponding spectrum (d). It is, however, noticed that the first harmonics dominate higher harmonics, with the first to second harmonic ratio being greater than 2.

4.3.2 Cross-shore variation of wave amplitude and velocity

Figure 4-9 shows the variation of several representative values of wave amplitude, A_1, A_e, A_{wr}, which are defined as in the non-breaking wave experiments and the experiments without a wall. Figure 4-10 shows the variation of horizontal velocities, U_1, U_e and U_{wr}, which are the corresponding values to A_1, A_e and A_{wr}.

It is noted that all the representative amplitudes in Figure 4-9 are close to one another, within a difference of 10% to 15%. It is seen from the figure that the average of the wave amplitude starts dropping around x = 12 m, in agreement with the observed break point x = 11.8 m.

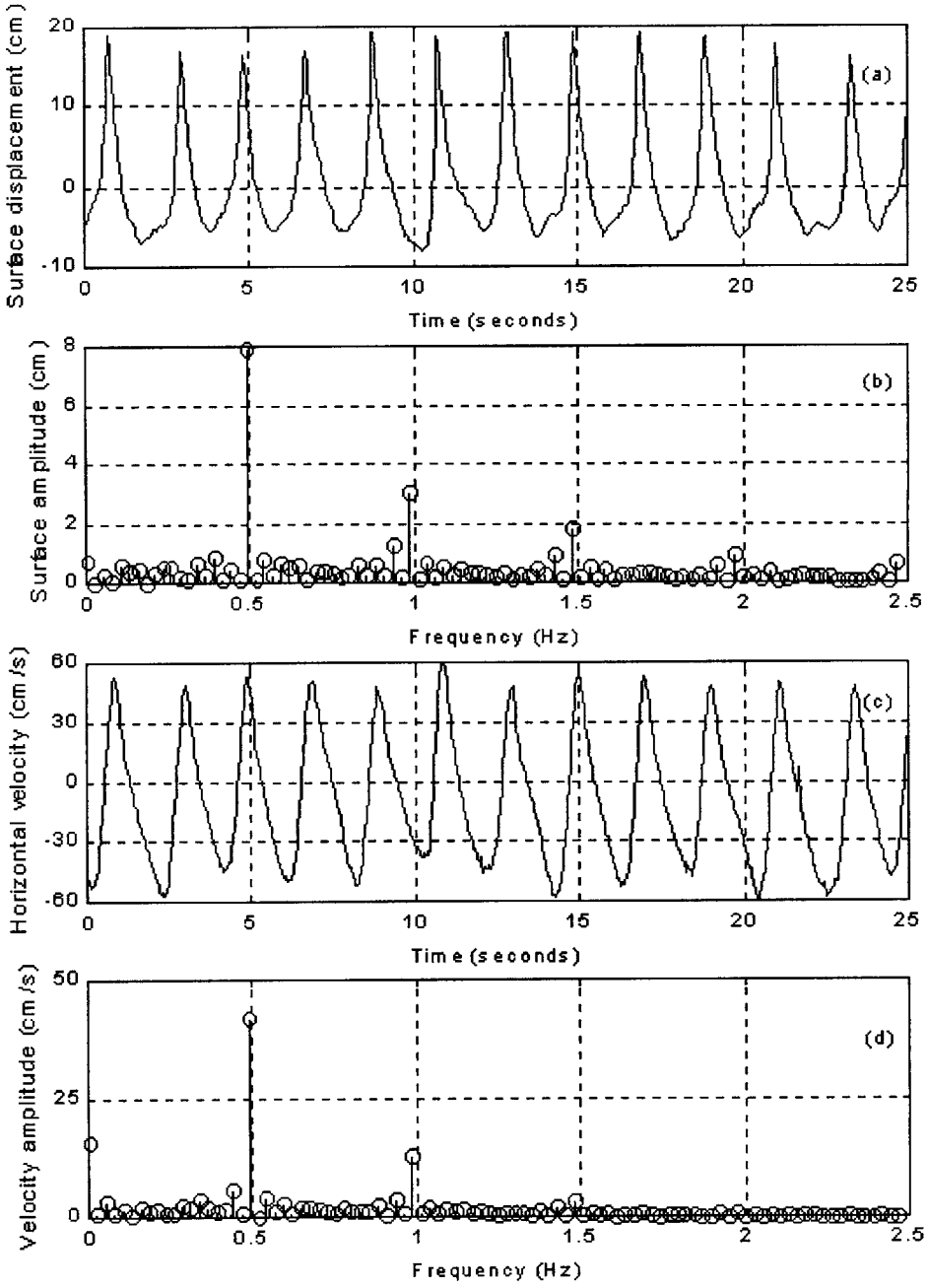

Figure 4-8 Wave records and frequency spectra at x = 12.2 m, right after breaking; (a) surface displacement, (b) surface amplitude spectrum, (c) horizontal velocity record, (d) velocity amplitude spectrum. Note: only the first 96 points are shown in the spectra.

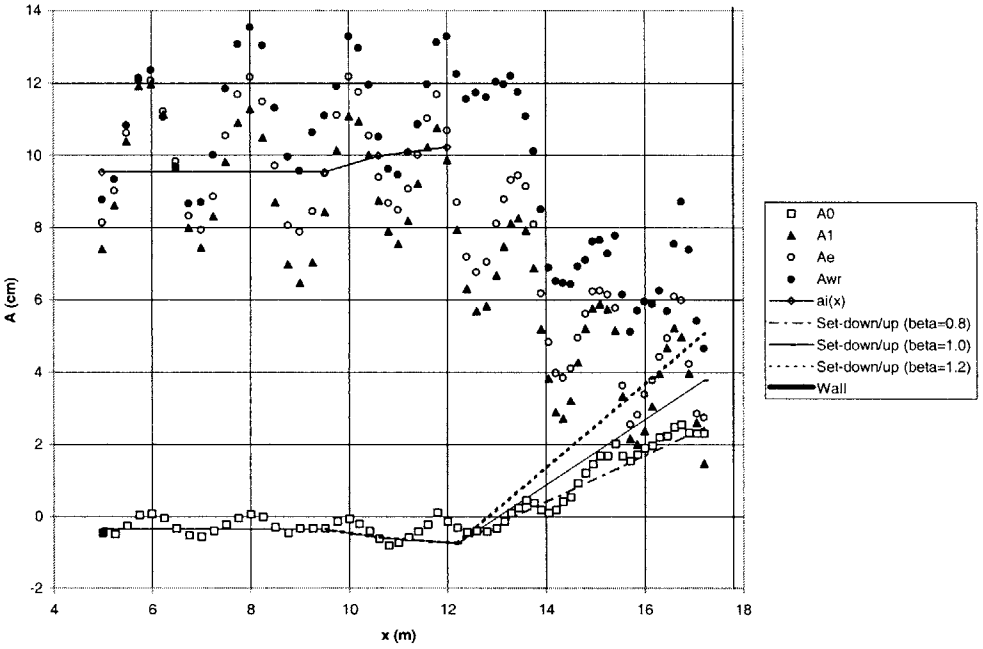

Figure 4-9 Cross-shore variation of wave amplitude

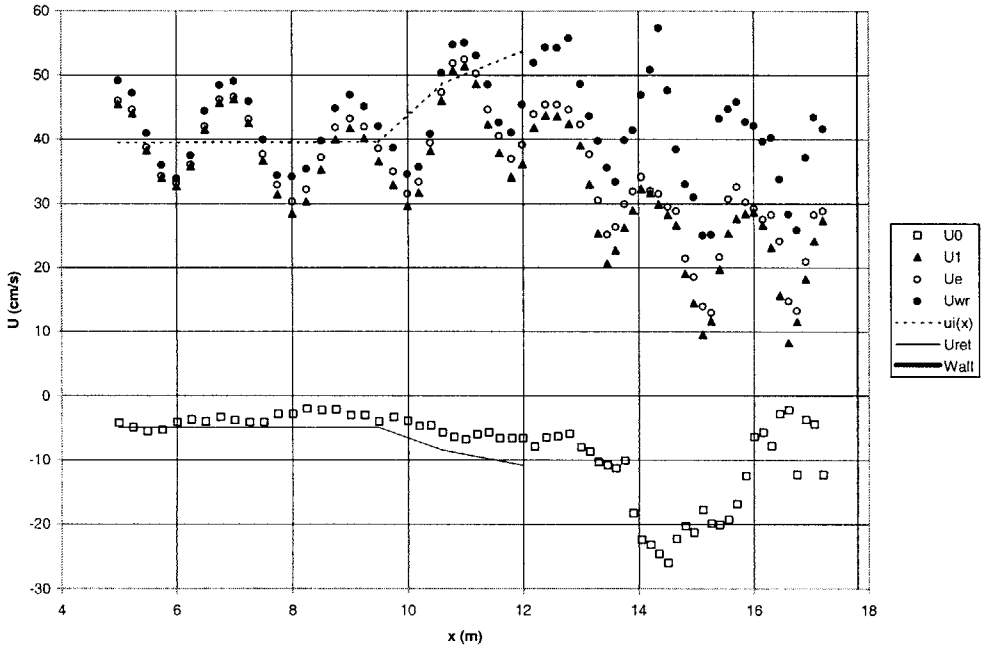

Figure 4-10 Cross-shore variation of horizontal velocity

The incident wave amplitude accounting for shoaling, $a_i(x)$, is predicted using (3.11) and shown in Figure 4-9, with the constant depth portion's incident wave amplitude being the average obtained from temporal analysis (Section 2.2.1) within the beat length from $x = 6$ m to $x = 8$ m, i.e., $a_{ic} = 9.54$ cm. Given the wave period $T = 2.03$ s and the still water depth in the constant depth region $h_c = 46$ cm, linear theory gives the group velocity $C_{gc} = 169$ cm/s and wave length $L = 398$ cm. Thus, the incident waves correspond to $U = HL^2/h^3 = 32$, i.e., quite nonlinear. C_{gc} and a_{ic} are then used in (3.11) to calculated the incident wave amplitude on the slope due to shoaling.

The clear waviness of A_1 throughout the wave channel is strong evidence of reflection, with the average remaining nearly constant in the constant depth region, increasing on the slope and then dropping after the break point. The maximum wave amplitudes in Figure 4-9 appears around $x = 6$ m, $x = 8$ m and $x = 10$ m, and these locations correspond to minimum horizontal velocity amplitudes in Figure 4-10. An estimate of reflection coefficient in the constant depth region can be made by taking the segment of the A_1 curve between $x = 6$ m and $x = 8$ m, that is $R \approx \dfrac{(A_1)_{\max} - (A_1)_{\min}}{(A_1)_{\max} + (A_1)_{\min}} = \dfrac{12.0 - 7.4}{12.0 + 7.4} = 24\%$.

This value is considerably lower than what we expected from the highly reflective vertical seawall.

The predicted incident wave set-down/up calculated using (3.13), before the break point, and (3.14), after the break point, also agrees well with the measurements. After the break

point, the three lines with different β values are drawn for comparison (see 3.14). It appears that the best β value is about 0.8.

Figure 4-10 shows the horizontal velocity variation, with the same symbols as in the non-breaking wave experiments presented previously in this chapter and for the no-structure breaking wave experiments presented in Chapter 3. Again, the first harmonic velocity U_1 is fairly close to the energy velocity amplitude U_e and record velocity amplitude U_{wr}, while in the surf zone, U_1, still close to and U_e, deviates from U_{wr}. The velocity amplitudes all tend to drop at x = 12 m, similar to the wave amplitudes variation and visual observation of the break point. For comparison, the predicted incident wave horizontal velocity calculated by (3.12), $u_i(x)$, is also shown in the figure.

The predicted incident wave return current U_{ret} obtained from (3.2) is in general agreement with the measurements up to the break point. It is interesting to notice that there is a transition region from x = 12 m to x = 13.75 m after the break point, followed by a developed undertow reaching –26 cm/s at x = 14.5 m and back to about -7.5 cm/s beyond x = 16.0 m. This behavior, seen in Figure 4-10, is very similar to the behavior of the return current observed in the no-wall breaking wave experiments shown in Figure 3-6.

4.3.3 Cross-shore variation of incident and reflected wave characteristics

Figure 4-11 shows the spatial curve fitting of the first harmonic wave amplitude in which the circles stand for the measurements with the solid line being the prediction.

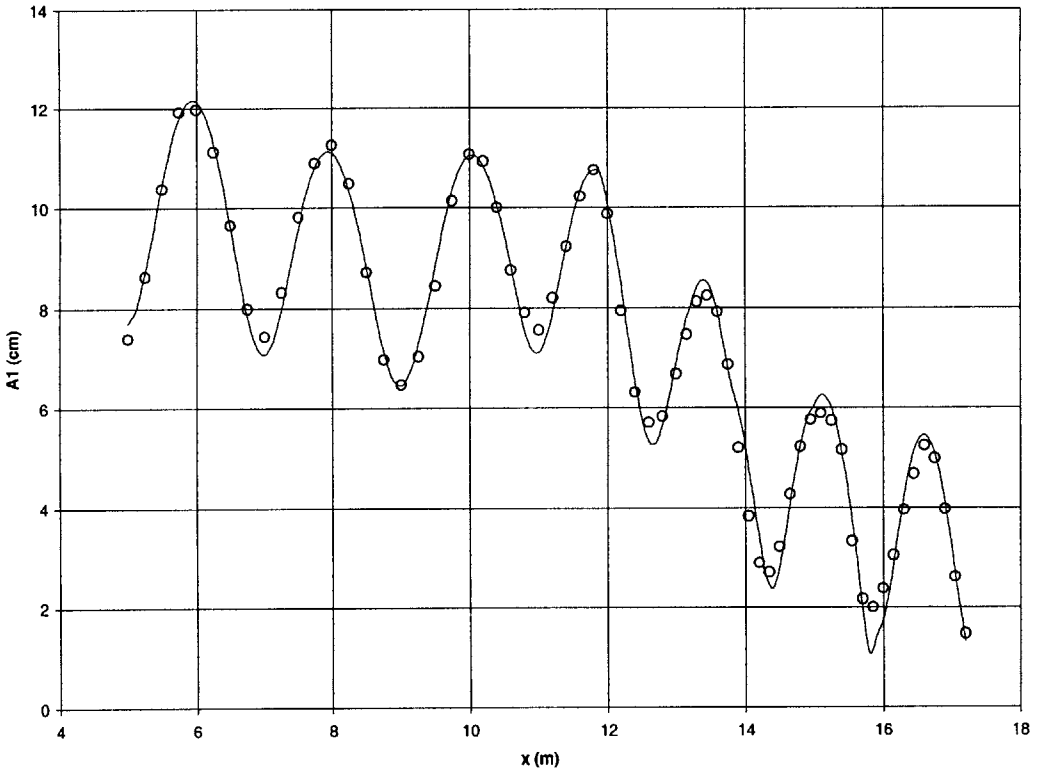

Figure 4-11 Spatial curve fitting of the first harmonic wave amplitude

The variation of incident wave amplitudes resolved from temporal and spatial analyses, described in Sections 2.2.1 and 2.2.2 respectively, is shown in Figure 4-12. For comparison, the predicted incident wave amplitude and the first harmonic incident wave amplitude, dotted trend line, and the predicted $a_i(x)$ are also shown in the figure.

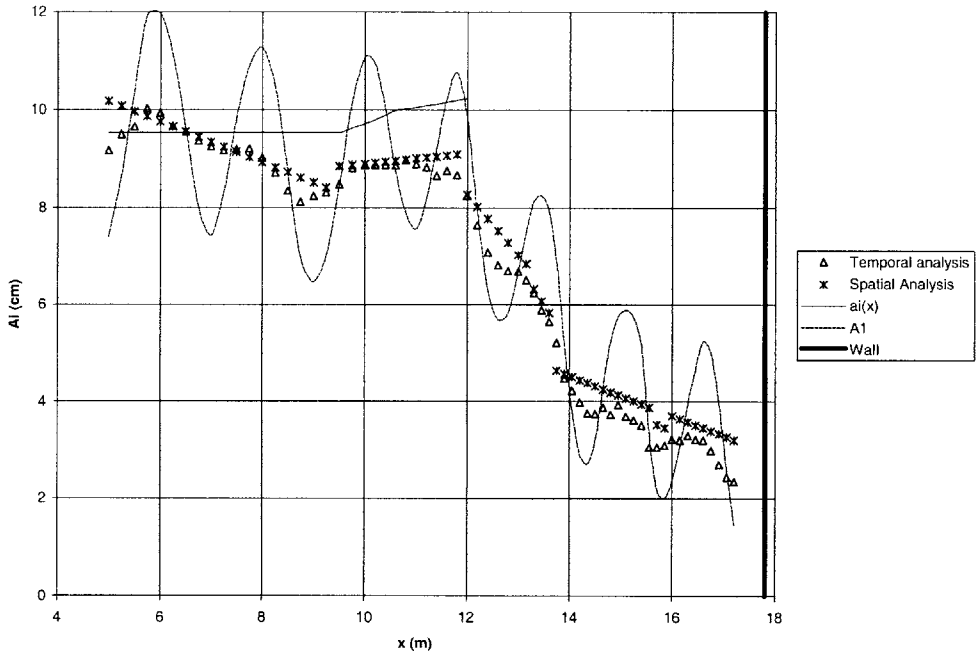

Figure 4-12 Cross-shore variation of incident wave amplitude

The temporal and spatial analyses are in excellent agreement in Figure 4-12. They both decay gently in the constant depth region, then increase on the slope, start dropping sharply from x = 12.0 m to x = 14.0 m, and decay more gently again beyond x = 14.0 m. This general behavior is also seen in Figure 3-7 of Chapter 3 for the no-structure experiments.

The still water depth is 14.8 cm at the last antinode of the measurement (x = 16.6 m), corresponding to a beat length of 1.23 m given the wave period of 2.03 s. The still water depth at the seawall (x = 17.8 m) is 11.0 cm which corresponds to a beat length of 1.04 m. Therefore, the next antinode following the one at x = 16.6 m should be located

between x = 17.66 m and x = 17.83 m, which is in good agreement with the anticipation that an antinode should be located at the seawall (x = 17.8 m).

The reflected wave amplitude variation in Figure 4-13 shows organized waviness demonstrated by the dotted line, the beat length being half the incident wave length again. The spatial results are somewhat larger than those obtained from temporal analysis, although they are close. The reflected waves beyond the break point do not appear to differ very much from those before breaking, with the mean shifting slightly downward and the amplitude increasing a little, probably due to increased nonlinearity of the waves. At x = 17.2 m, the Ursell number associated with the reflected wave is $U = H_r L^2 / h^3$ = 45 with reflected wave height H_r = 2.8 cm, wave length L = 242 cm and the water depth h = 15.2 cm.

For comparison, the predicted reflected wave amplitude accounting for shoaling, $a_r(x)$ is predicted using (4.1) and shown in Figure 4-13, with the constant depth portion's reflected wave amplitude being the average obtained from temporal analysis within the beat length from x = 6 m to x = 8 m, i.e., a_{rc} = 1.98 cm. Given the wave period T = 2.03 s and the still water depth in the constant depth region h_c = 46 cm, linear theory gives the group velocity in the constant depth region C_{gc} = 169 cm/s. C_{gc} and a_{rc} are then used in (4.1) to calculate the reflected wave amplitude due to shoaling.

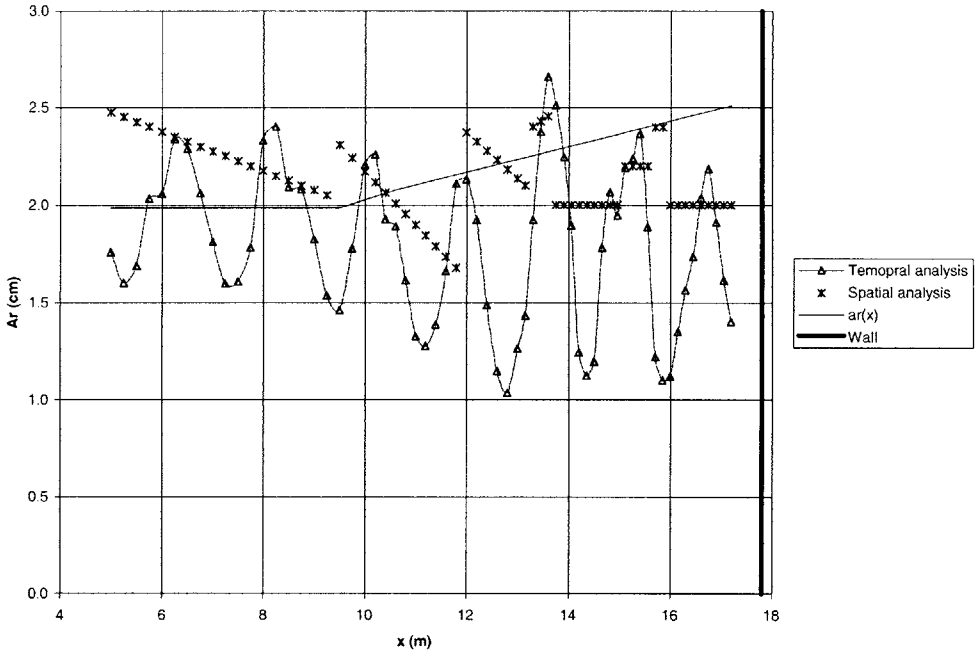

Figure 4-13 Cross-shore variation of reflected wave amplitude

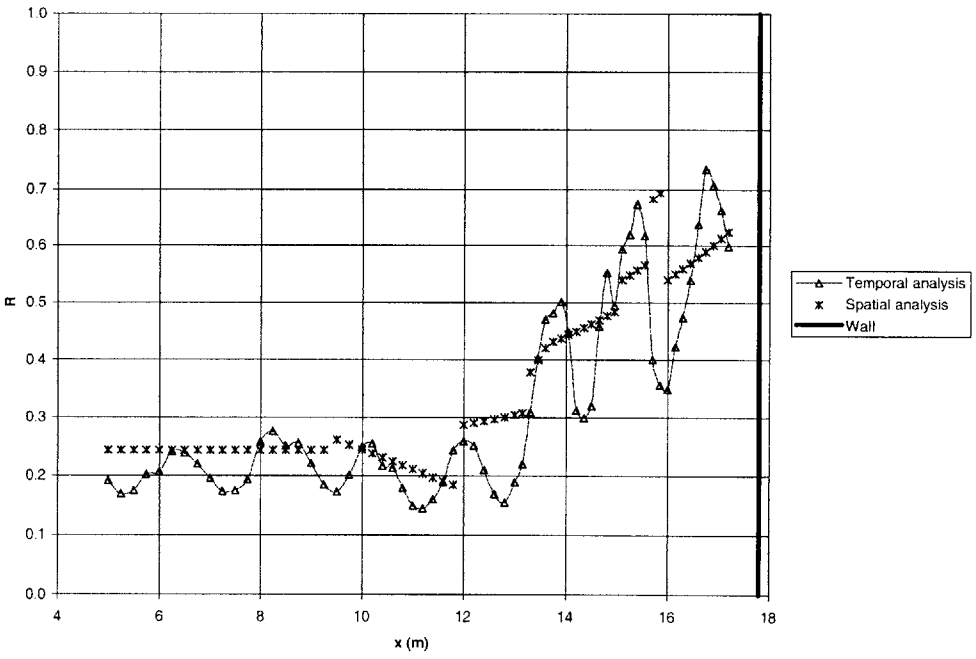

Figure 4-14 Cross-shore variation of reflection coefficients

It is of interest to examine the variation of reflection coefficients which is shown in Figure 4-14. Despite the waviness of temporal results, they agree well with those obtained from the spatial analysis. The reflection coefficient fluctuates around 0.2 in the constant depth region up to the break point, where it starts to increase dramatically to about 0.65 at x = 17.2 m which is near the seawall located at x = 17.8 m. It is noticed that this value of the reflection coefficient immediately in front of the wall is close to the value obtained for non-breaking waves shown in Figure 4-7 ($R \cong 0.7$). The increase in reflection coefficient is largely due to the dramatic drop of incident wave height beyond the break point, as seen in Figure 4-12, and the near-constancy of the reflected wave amplitude, shown in Figure 4-13.

In Figure 4-14, the last antinode of the measurement is located at x = 16.75 m, 1.05 m away from the seawall. This value is in good agreement with the beat length (1.04 m) at the seawall, as discussed previously in this chapter.

4.3.4 Behavior after breaking

It is of importance to examine the behavior of incident and reflected waves after breaking. The incident wave height (denoted by circles), along with the still water depth (denoted by squares) and still water depth plus set-up (denoted by triangles) is shown in Figure 4-15 where the full symbols are the values well beyond the break point (x > 14.5 m) and the straight lines are the linear best fit to these values. The still water level intersects the beach at x = 21.29 m with R^2 = 0.998. It should be noticed that this intersection is not equal to the value (22.56 m) in the no-structure experiment because of

the slightly different water depth in the constant depth region. The difference in h_c is 4 cm and the slope is 1 on 30. The difference in still water level intersection with the slope should therefore be $\Delta x = 4 \cdot 30 = 120$ cm, as observed. The intersections of the mean water level and the incident wave height with be beach are located at $x = 23.20$ m ($R^2 = 0.989$) and $x = 22.60$ m ($R^2 = 0.810$), respectively. Again, these two locations shift seaward by similar amount (0.90 m and 0.73 m, respectively) due to the slight difference in water depth in the constant depth region, compared with the corresponding values in the no-structure experiments in which the mean water level intersection is located at $x = 24.10$ m and the incident wave height intersection is located at $x = 23.33$ m. The "rule" is still reasonable that the wave height varies linearly with water depth beyond breaking.

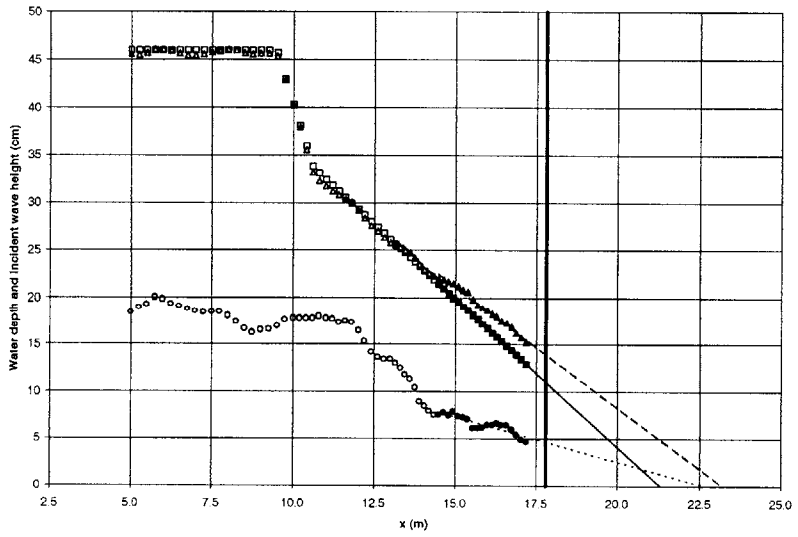

Figure 4-15 Variation of incident wave height and water depth; the triangles stand for still water depth plus set-up $h_+ = h + A_0$; the squares being the still water depth h; the circles the incident first harmonic wave height H_{i1}; and the full symbols for data well beyond the break point ($x > 14.5$ m)

Like we did in Chapter 3, we establish a horizontal axis, "X", with zero at x = 23.20 m, the intersection of total water level and the beach, and positive direction seaward, i.e., $X = 23.20 - x$. The X-axis is then non-dimensionalized by the position of the visually observed breaking point X_B = 11.4 m. The total first harmonic wave height H_1, the energy wave height H_e, the RSS wave height, H_{RSS}, defined by (3.5), and the record wave height H_{wr} normalized by total water depth are plotted in Figure 4-16 for comparison.

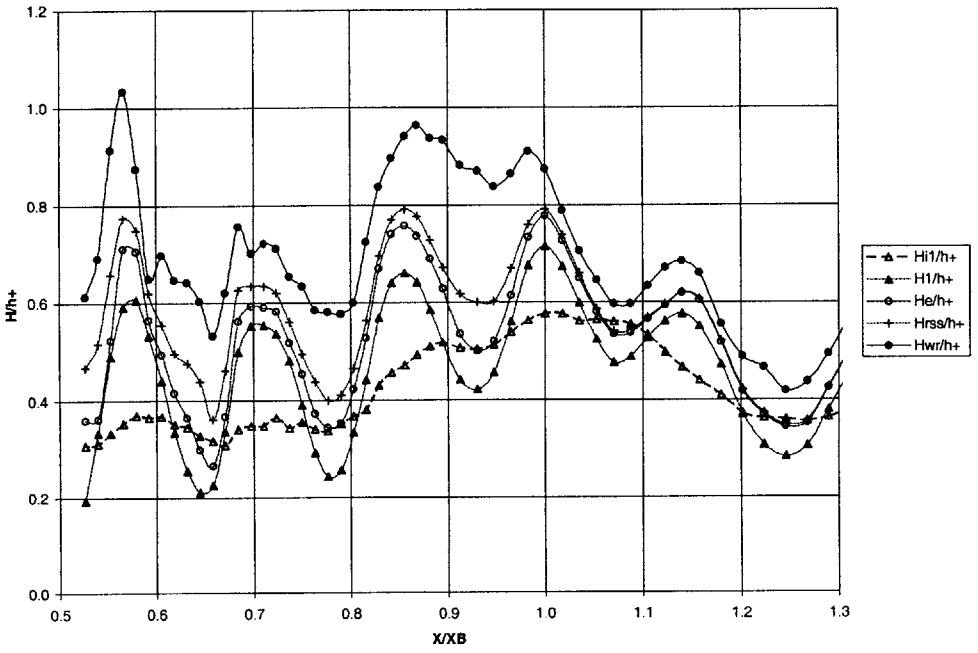

Figure 4-16 Variation of wave height non-dimensionalized by total water depth h_+

All the H/h_+ curves exhibit organized waviness. It is noticed that the waves broke at x = 11.8 m, an antinode, which is in agreement with the incident wave amplitude data suggestion of breaking (see also Figure 4-12) and the visual observation during the

experiment. At the break point, $(H_{wr}/h_+)_B$ (subscript "B" denoting breaking point) gives a maximum value of 0.87, whereas $(H_e/h_+)_B$, $(H_1/h_+)_B$ and $(H_{i1}/h_+)_B$ are 0.78, 0.72 and 0.58, respectively. All these values are higher than those obtained in the no-wall experiments presented in Chapter 3 in which $(H_{wr}/h_+)_B = 0.85$, $(H_e/h_+)_B = 0.61$, $(H_1/h_+)_B = 0.49$ and $(H_{i1}/h_+)_B = 0.48$. The predicted non-dimensional incident wave height $(H_i(x)/h_+)_B = 0.68$ with $H_i(x)_B = 2a_i(x)_B = 20.4$ cm (see Figure 4-9). However, when the average of high value at breaking and the subsequent low value is taken, $(H_{wr}/h_+)_B$, $(H_e/h_+)_B$, $(H_1/h_+)_B$ and $(H_{i1}/h_+)_B$ give 0.86, 0.64, 0.57 and 0.54, respectively. Compared with the no-wall experiments, they are in general agreement. The average lines of all H/h_+ curves start to decay beyond breaking and remain essentially constant with $(H_{i1}/h_+)_{B+} = 0.34$, $(H_1/h_+)_{B+} = 0.39$, $(H_e/h_+)_{B+} = 0.43$ and $(H_{wr}/h_+)_{B+} = 0.69$ where the subscript "B+" denotes the data well beyond breaking, i.e., $X/X_B < 0.75$. They are in good agreement with no-structure experiments (except non-dimensional record wave height) in which $(H_{i1}/h_+)_{B+} = 0.36$, $(H_1/h_+)_{B+} = 0.39$, $(H_e/h_+)_{B+} = 0.44$ and $(H_{wr}/h_+)_{B+} = 0.56$.

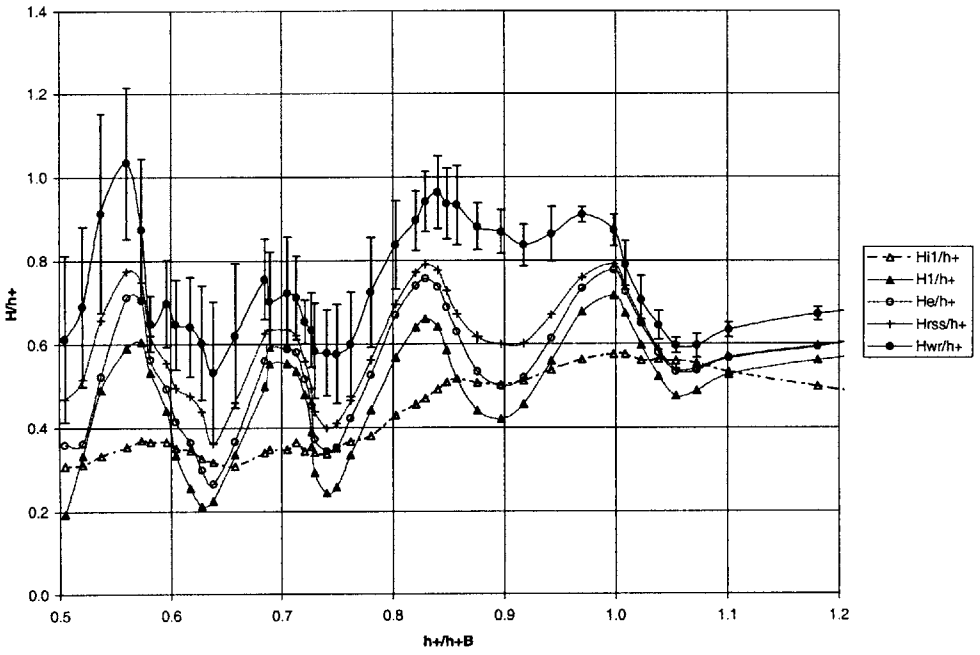

Figure 4-17 Wave height variation with water depth

In Figure 4-17, the horizontal axis is the total water depth non-dimensionalized by that of the breaking point h_{+B} = 30.1 cm at x_B = 11.8 m. The error bars on H_{wr}/h_+ show the standard deviation. In the surf zone, the wave record is somewhat difficult to measure as discussed in Section 3.2 and this is reflected in the relatively large variability of the H_{wr}/h_+ values beyond breaking, i.e., when $h_+/h_{+B} < 1$. The average non-dimensional incident wave height, after reaching a maximum of 0.58, tends to decay sharply and then remain nearly constant at 0.34 within a beat length despite the waviness caused by high reflection.

4.3.5 Comparison with lower wave height experiments

For comparison, two other experiments with lower wave height (incident wave height being about 16 cm) were made and the incident and reflected wave characteristics are shown in Appendix B. In experiment #1, the still water depth in the constant depth region was 47.7 cm with wave period of 2.03 seconds and the waves broke visually at x = 12 m. while in experiment #2, the still water depth in the constant depth region was 46.1 cm with wave period of 2.07 seconds and the waves broke visually at x = 11.8 m. The water depths in the constant depth portion, the wave periods and the visually observed break points are all close to the higher wave experiment presented previously. The temporal (Section 2.2.1) and spatial (Section 2.2.2) analyses give results in close agreement for incident wave amplitude A_i, reflected wave amplitude A_r and reflection coefficient R, therefore in the following comparison, only the results obtained from experiment #1 is presented as the lower waves. The incident wave amplitude A_i decays in the constant depth region, then increases on the slope, drops dramatically after breaking followed by the a gentle decay. The reflection coefficient fluctuates around a constant of 0.27 in the constant depth region and increases beyond the break point, reaching about 0.75 at x = 17.2 m. All these phenomena are similar to the higher wave experiments with incident wave height being about 20 cm (see Figure 3-7).

This similarity can also be seen from a direct comparison of the incident wave amplitude resolved from temporal analysis (Section 2.2.1), Figure 4-18. As seen from Figure 4-18, the incident wave amplitude obtained from temporal analysis has the same behavior beyond breaking in the higher and lower wave experiments, with an initial sharp decay

followed by a gentle decay. The reflected wave amplitude and the reflection coefficients, presented in Figures 4-19 and 4-20, respectively, also show the similar variation. The latter fluctuates around a constant of 0.27 and increases dramatically to about 0.7 near the seawall which again agrees with the reflection coefficient obtained for non-breaking waves. It is noticed that the reflected wave amplitude A_r in Figure 4-19 is nearly the same, i.e., independent of the incident wave amplitude in the constant depth region. This similarity is also seen in the reflection coefficient's variation in Figure 4-20, where the slightly larger values of R for the smaller incident wave height is caused by the smaller incident wave amplitude A_i.

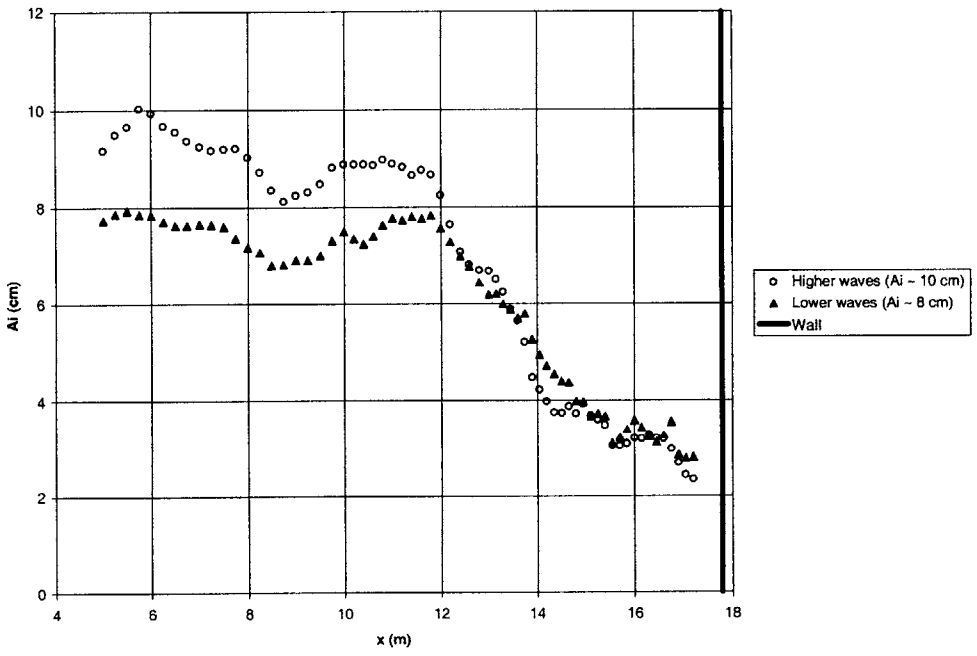

Figure 4-18 Comparison of incident wave amplitude from temporal analysis

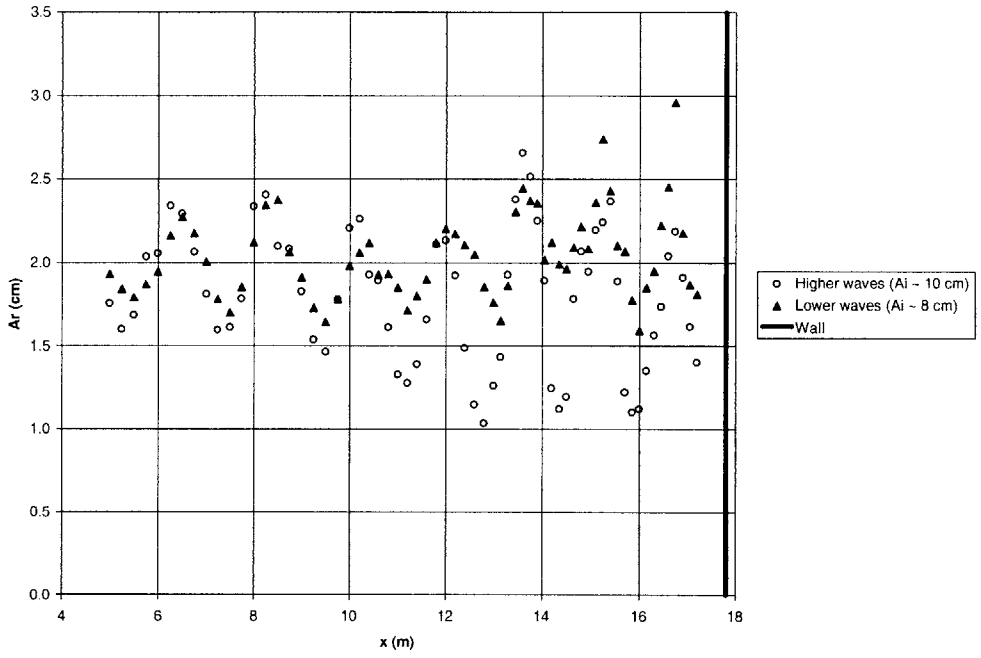

Figure 4-19 Comparison of reflected wave amplitude from temporal analysis

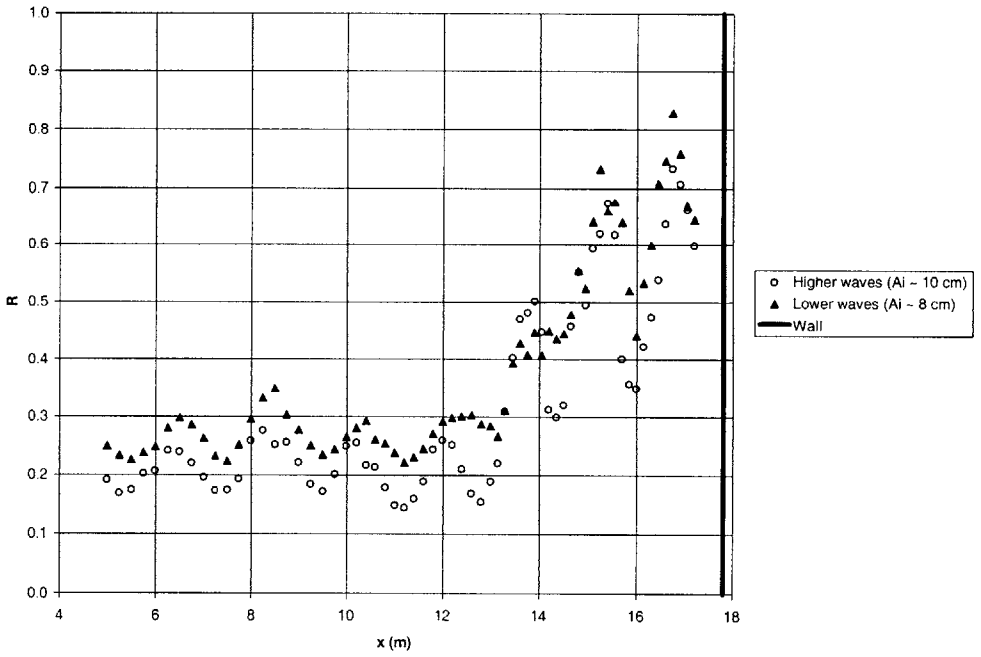

Figure 4-20 Comparison of reflection coefficient from temporal analysis

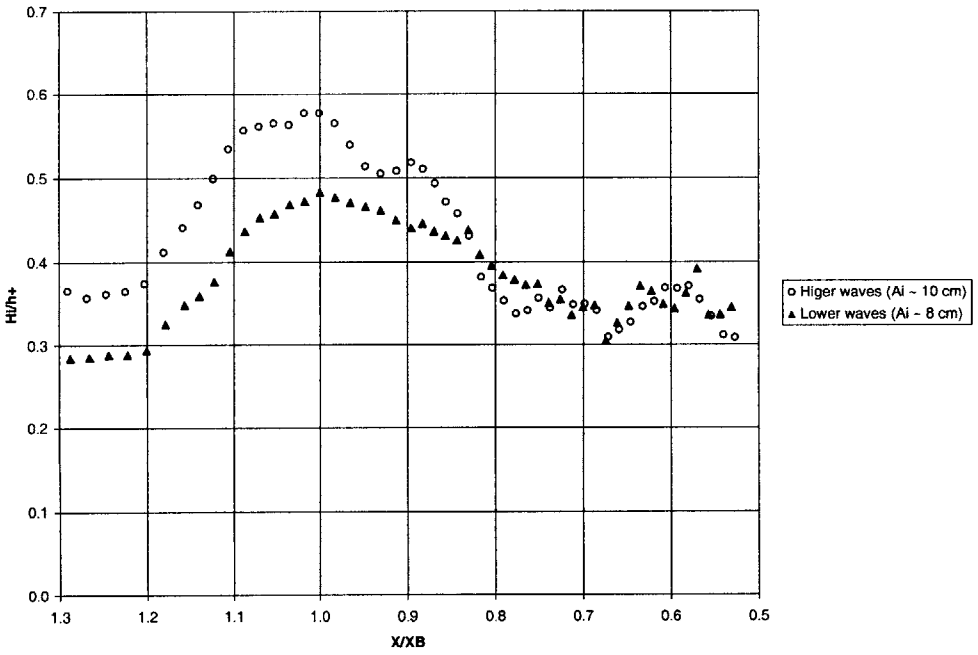

Figure 4-21 Non-dimensional incident wave height variation around breaking

Figures 4-21 shows the variation of incident wave height non-dimensionalized by the total water depth h_+. The X -axis has the same meaning as previously described. At the break point, H_i / h_+ of the higher waves yields 0.58 whereas that of the lower waves is 0.49. However, they behave close beyond breaking, fluctuating around 0.34.

4.3.6 Comparison with experimental results in the absence of highly reflecting structures

The purpose of the experiments is to investigate the potential influence of a highly reflecting seawall in the surf zone on the dissipation of incident wave energy after breaking. It is therefore of particular interest to compare the breaking wave results in the

presence of a vertical wall with those obtained in the absence of highly reflective structures, presented in Chapter 3.

The incident wave amplitudes resolved from no-seawall experiments are plotted in Figure 4-22 together with the vertical-wall experimental results. In the no-wall experiments, the waves broke visually at x = 13.1 m, however, the incident wave amplitude appeared to start decaying at 12.2 m which is before the visually observed break point. The waves in the presence of a vertical wall broke visually at x = 11.8 m, which coincides with the point where A_i begins to drop. It is noticed that the two curves have the same trend, i.e., both decaying dramatically around x = 12.0 m and then decreasing gently beyond x = 15 m. Therefore, the incident waves do not appear to be significantly affected by the presence of a highly reflective structure.

The comparison of non-dimensional incident wave height in the no-seawall and in the vertical-wall experiments is shown in Figures 4-23. Note that the "break point" in the no-wall experiment is "corrected" to x = 13.6 m as in Figures 3-12 and 3-13. At the break point, the non-dimensional incident wave height is 0.52 (no-wall) and 0.58 (vertical-wall), respectively. It is of importance to note that the behavior of the two curves beyond the break point show the same trends, both fluctuating around 0.34.

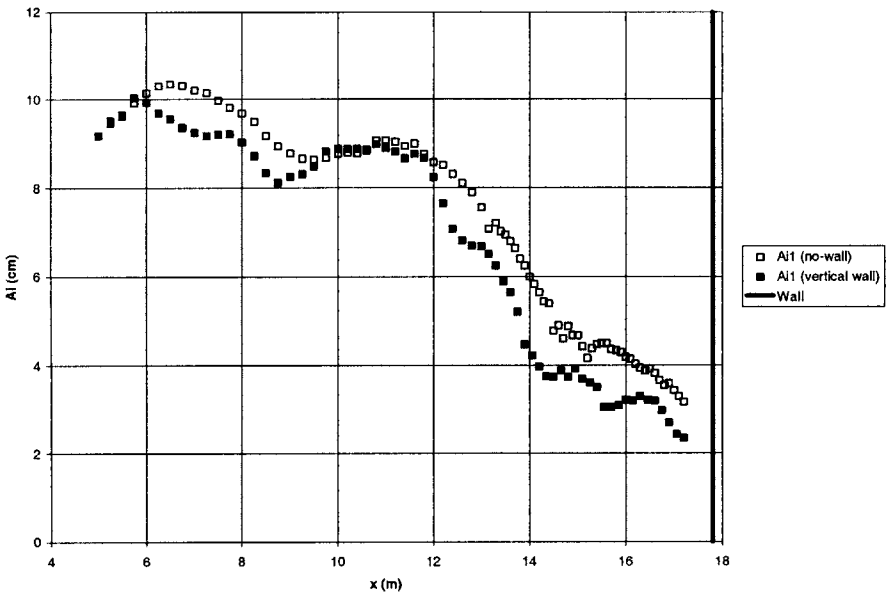

Figure 4-22 Comparison of incident wave amplitude from the no-wall and the vertical-wall experiments

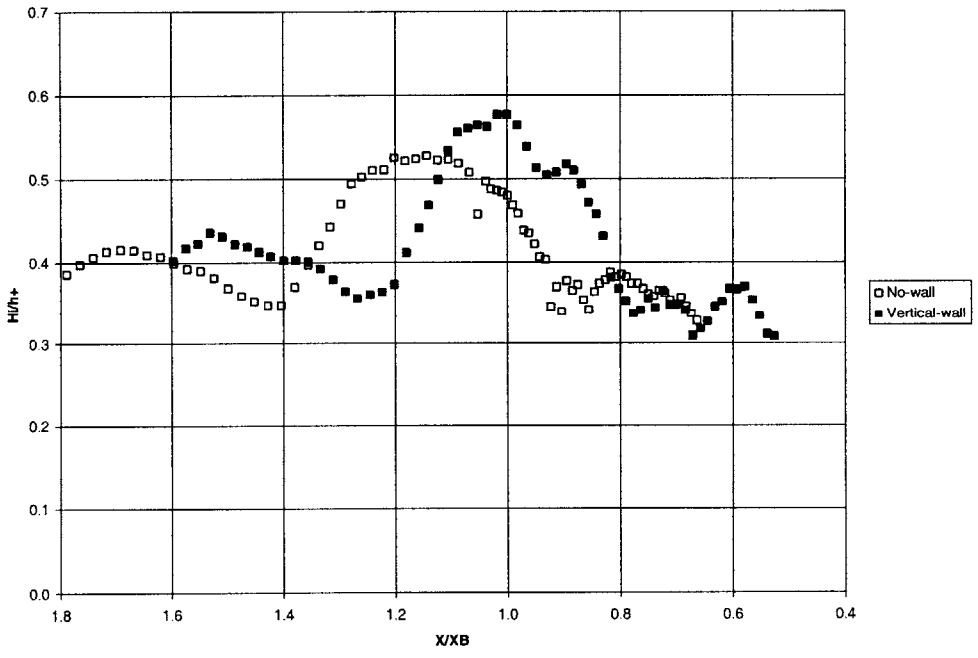

Figure 4-23 Comparison of incident wave height variation near breaking

Through the comparison of incident wave height obtained from the no-seawall breaking wave and vertical-seawall breaking wave experiments, we do not see strong evidence that incident waves after breaking are affected significantly by the presence of a vertical seawall. From the comparison of reflected wave heights obtained from non-breaking and breaking wave experiments in the presence of a vertical seawall, we furthermore conclude that the reflected wave is not affected by the seawall, either, i.e., the reflected waves do not appear to lose energy as they travel seaward from the seawall whether they pass through a surf zone or not on their way.

Chapter 5

Experimental Results in the Presence of Sloped Seawalls

5.1 Overview of experiments

Two sets of experiments, one with non-breaking waves and the other with breaking waves, were carried out in the presence of a 1 on 1.5 sloped seawall, whose toe is located at x = 17.8 m. As described in Chapter 2, the 1 on 10 beach slope starts from x = 9.5 m and ends at x = 10.6 m, beyond which point the beach slope is 1 on 30. The non-breaking wave experiments provide the reflection coefficient of the reflective structure, whereas the breaking wave experiments give the incident and reflected wave characteristics due to breaking, which is the goal of the present research. In both experiments, the wave maker was run 15 minutes in order for stationarity to be established before measurements were taken. The experimental results are shown in the following sections 5.2 (non-breaking waves) and 5.3 (breaking waves), respectively.

5.2 Non-breaking wave experimental results

In the non-breaking wave experiments, the wave period was 2.03 seconds and the water depth in the constant depth region was 51.0 cm. The wave height was kept small (incident wave height being roughly 5.5 cm) so that the waves did not break at any point along the flume. A three-minute record of both water surface displacement and velocity was taken at 77 locations from $x = 5.0$ to $x = 17.2$ m. The measuring interval in the constant depth region was 25 cm, while it shortened to 20 cm on the slope, and 15 cm near the toe of the seawall, respectively. Because the friction introduced by the rubble glued to the seaward side of the reflective structure dissipates a small portion of wave energy, we would expect a reflection coefficient to be less than but close to unity.

5.2.1 Wave records and frequency spectra

The wave record is very periodic throughout the wave channel, even on the slope and near the toe of the structure although the waves are quite non-linear. The wave records and frequency spectra shown in Figure 5-1 are from the $x = 15.7$ m which is on the 1 on 30 slope. The periodicity is obvious in both surface profile and velocity record, with each wave being virtually identical to its neighbors. The surface displacement (b) and horizontal velocity (d) spectra show that the first harmonic is dominant over higher harmonics.

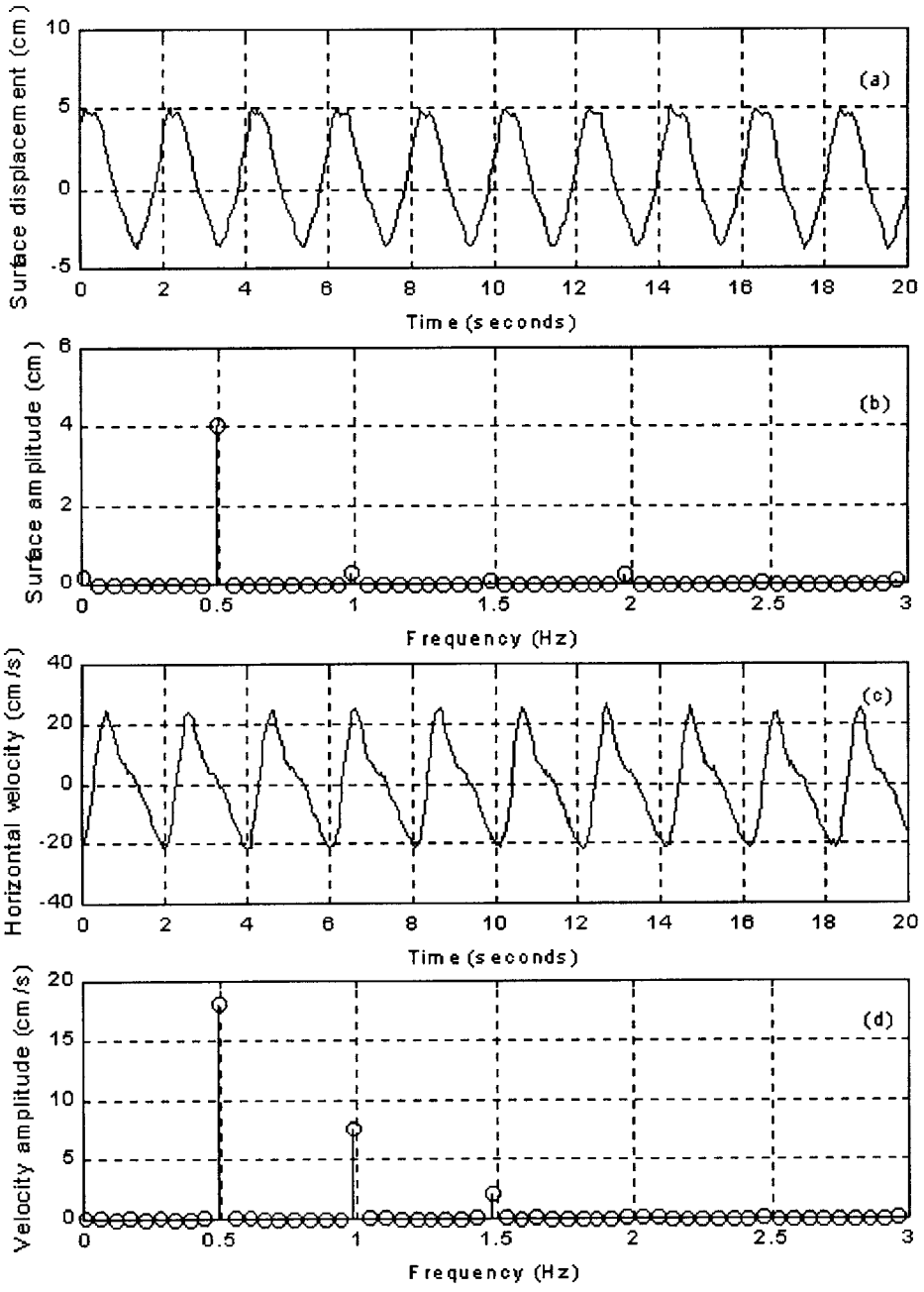

Figure 5-1 Wave records and frequency spectra at x = 15.7 m; (a) surface displacement record $\eta(t)$, (b) surface displacement spectrum, (c) horizontal velocity record $u(t)$, (d) horizontal velocity spectrum. Note: only the first 74 points are shown in the spectra.

We also see from the *zero* th harmonics in (b) and (d), i.e., twice the mean of $\eta(t)$ and $u(t)$, that the wave set-down and return current are both very small which is also reflected in the wave records (a) and (c), respectively. The incident wave height at x = 15.7 m is H = 5.3 cm, calculated using the temporal analysis presented in Section 2.2.1. Given T = 2.03 s and h = 22.4 cm, linear wave theory gives kh = 0.49 and the second order Stokes wave theory (3.2) gives an incident wave return current of –1.5 cm/s. The predicted wave set-down calculated by (3.13) is –0.09 cm. Both values are in good agreement with our observation from (b) and (d).

5.2.2 Cross-shore variation of wave characteristics

Figure 5-2 shows the variation of wave amplitudes in which A_0 is the wave set-down/set-up, A_1 is the first harmonic wave amplitude and A_{wr} is the record wave amplitude. Figure 5-3 shows the variation of horizontal velocities in which U_0 is the return current, U_1 and U_{wr} are the corresponding values to A_1 and A_{wr}, respectively.

As A_1 is close to A_e which can also be seen from the spectrum in Figure 5-1 (b), only the first harmonic wave amplitude A_1 is shown in Figure 5-2 along with the record wave amplitude A_{wr} (otherwise A_e will overlap A_1). Similarly, only U_1 is shown together with U_{wr} in Figure 5-3.

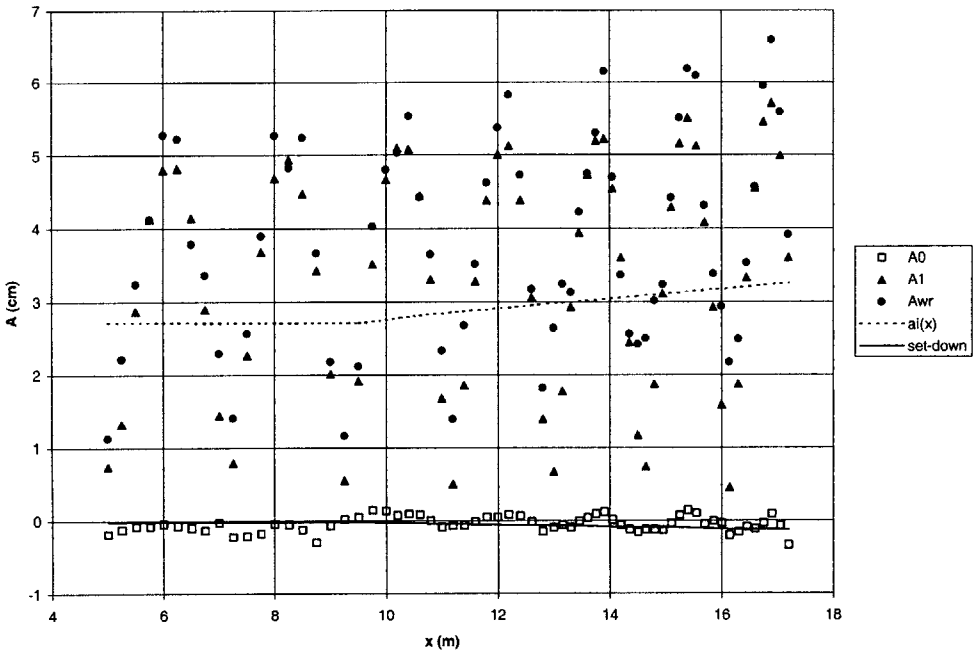

Figure 5-2 Cross-shore variation of wave amplitudes

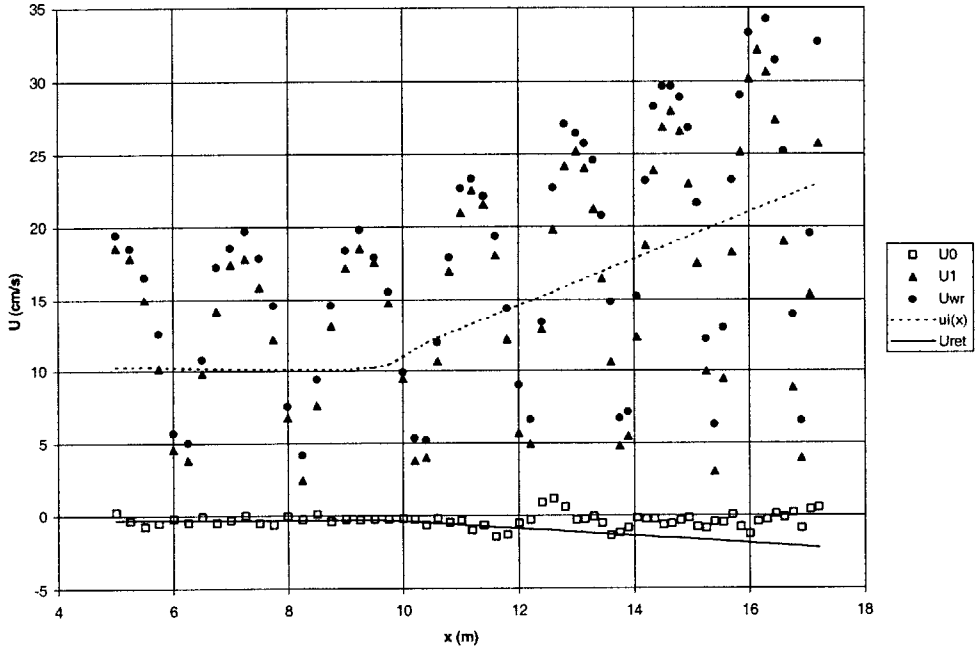

Figure 5-3 Cross-shore variation of horizontal velocities

The clear waviness of A_1 throughout the wave channel is strong evidence of reflection, with the average remaining nearly constant in the constant depth region and increasing slightly on the slope. The maximum wave amplitude in Figure 5-2 appears around $x = 6$ m, $x = 8.25$ m and $x = 10.2$ m, and these locations correspond to minimum velocity amplitude in Figure 5-3. An estimate of reflection coefficient in the constant depth region can be made by taking the segment of the A_1 curve between $x = 6$ m and $x = 8.25$ m, that is $R \approx \dfrac{(A_1)_{\max} - (A_1)_{\min}}{(A_1)_{\max} + (A_1)_{\min}} = \dfrac{4.9 - 0.8}{4.9 + 0.8} = 72\%.$

For comparison, the incident wave amplitude accounting for shoaling, $a_i(x)$, is predicted using (3.11) and shown in Figure 5-2, with the constant depth portion's incident wave amplitude being the average obtained from temporal analysis (Section 2.2.1) within the beat length from $x = 6$ m to $x = 8.25$ m, i.e., $a_{ic} = 2.7$ cm. Given the wave period $T = 2.03$ s and the still water depth in the constant depth region $h_c = 51$ cm, linear theory gives the group velocity in the constant depth region $C_{gc} = 174$ cm/s. Given the still water depth $h_c = 51$ cm in the constant depth region and wave period $T = 2.03$ s, linear wave theory gives the wave length $L = 416$ cm. The Ursell parameter is then $U = HL^2/h^3 = 7.0$, indicating that linear theory is applicable. C_{gc} and a_{ic} are then used in (3.11) to calculated the incident wave amplitude on the slope due to shoaling. The corresponding horizontal velocity amplitude $u_i(x)$ is calculated using (3.12) and shown in Figure 5-3. Seen from Figure 5-2, $a_i(x)$ is virtually in the center of the A_1 curve, however, $u_i(x)$ appears to be slightly higher than the average line of U_1 in Figure 5-3.

Obtained from (3.13), the predicted incident wave set-down is also shown in Figure 5-2, which is fairly close to the measured values despite the small undulation of A_0 caused by reflection. The predicted incident wave return current U_{ret} obtained from (3.2) is shown in Figure 5-3. Again, the predicted and measured values are in good agreement in the constant depth region and a larger discrepancy appears on the 1 on 30 slope, which starts at x = 11.4 m, with a reflection-associated waviness of the measured values.

As the first harmonic component is dominant over the higher harmonics, we only use the first harmonic components in the following temporal and spatial analyses (described in Sections 2.2.1 and 2.2.2, respectively) to resolve the incident and reflected wave characteristics and these results are presented in Section 5.2.3.

5.2.3 Cross-shore variation of incident and reflected wave characteristics and reflection coefficient

Figure 5-4 shows the spatial curve fitting of the first harmonic wave amplitude variation, in which the circles in the figure stand for the measured values and the solid line is the fitted curve obtained using the methodology presented in Section 2.2.2.

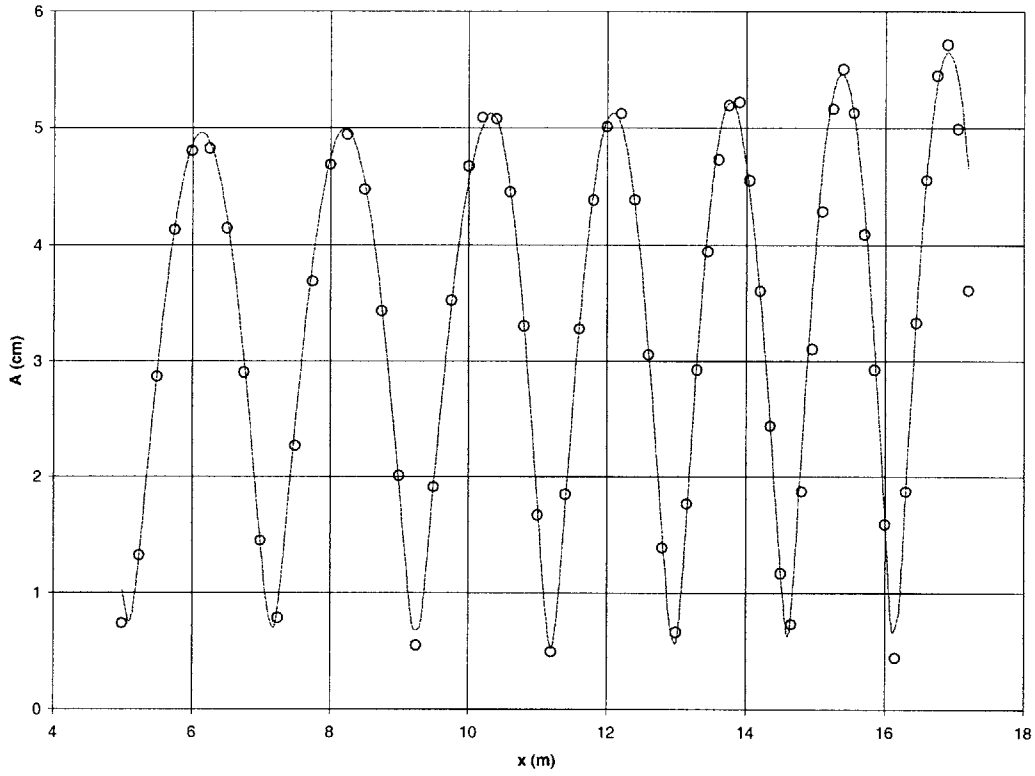

Figure 5-4 Spatial curve fitting of first harmonic wave amplitude

The resolved incident and reflected wave amplitudes from temporal (Section 2.2.1) and spatial (Section 2.2.2) analyses are shown in Figures 5-5 and 5-6, respectively. For comparison, the predicted wave amplitude accounting for pure shoaling, $a_i(x)$, and the first harmonic wave amplitude, A_1, indicated by the faint dotted line, are also shown in Figure 5-5.

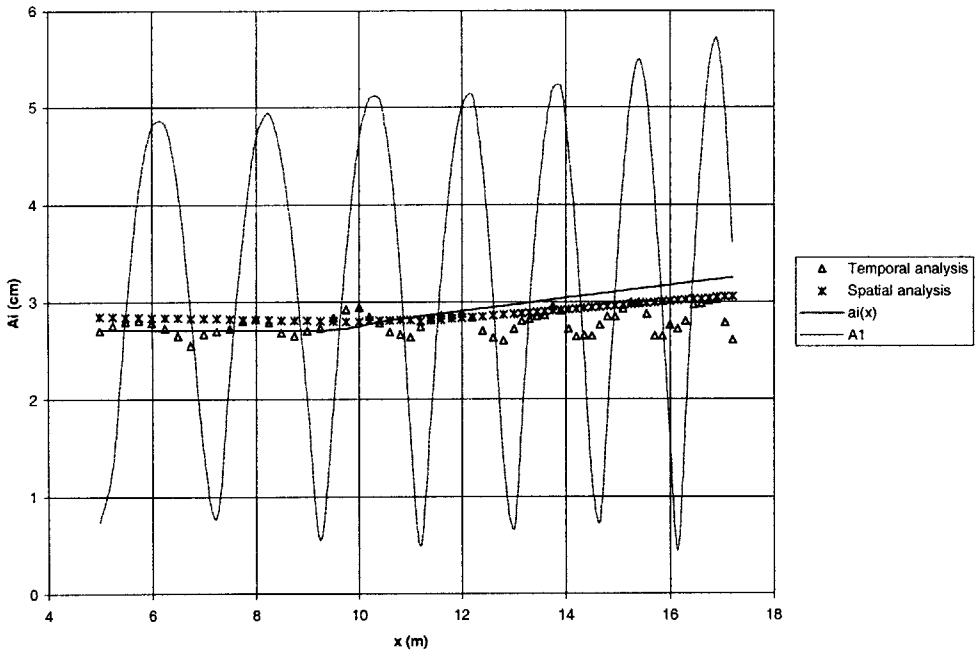

Figure 5-5 Cross-shore variation of incident wave amplitude

It is noticed that the incident wave amplitudes resolved from spatial analysis and temporal analysis are in excellent agreement, both decaying very slightly in the constant depth region and then increasing gently on the slope. The spatial line (denoted by "*") is obvious in the center of A_1 curve, which is expected.

The reflected wave amplitude (Figure 5-6), despite the variability, remains nearly constant (about 2.2 cm) in the constant depth region and starts to climb from x = 10 m up to x = 17.2 m. Again, the spatial and temporal analyses yield results in close agreement.

For comparison, the predicted reflected wave amplitude accounting for shoaling, $a_r(x)$, obtained from (4.1), is also shown in Figure 5-6. The average of constant depth portion's reflected wave amplitude from x = 6 m to x = 8.25 m, a_{rc} = 2.1 cm, is taken as the basis for the amplitude prediction on the slope. C_{gc} is equal to 174 cm/s as previously presented in this chapter. It is noticed that the predicted and measured values are in general agreement.

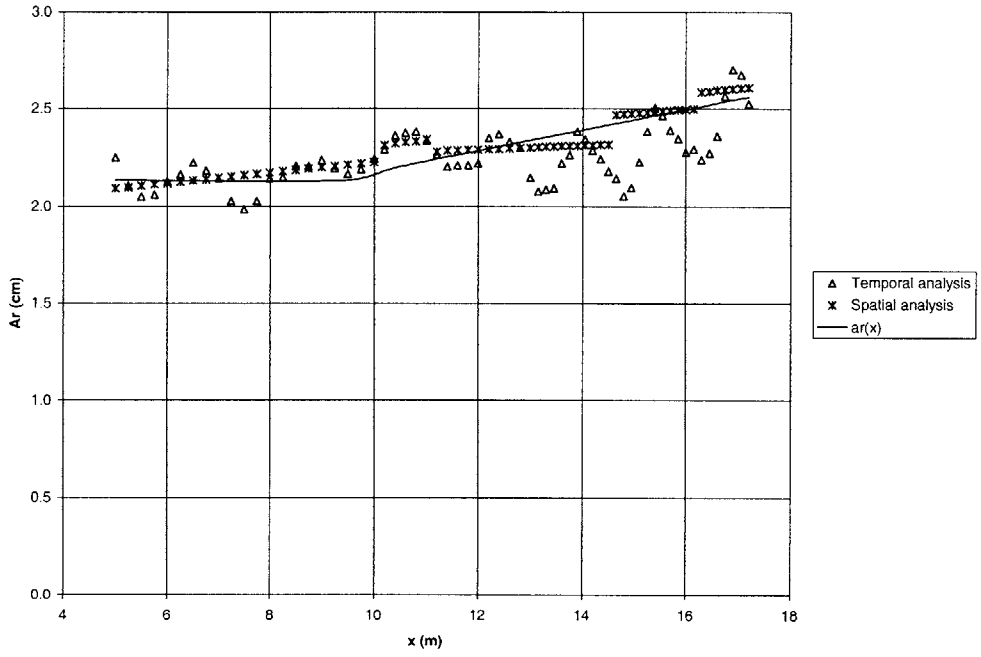

Figure 5-6 Cross-shore variation of reflected wave amplitude

Figure 5-7 shows the variation of reflection coefficients. Ideally, the reflection coefficient $R = a_r(x)/a_i(x) = a_{rc}(x)/a_{ic}(x)$ = 0.78 = constant since shoaling affects the incident wave a_i and reflected wave a_r in the same manner. With the incident and reflected wave amplitudes resolved from spatial and temporal analyses being close to each other, respectively, the good agreement of reflection coefficients from both analyses is therefore

expected. Despite the variability, the reflection coefficient remains nearly constant around 0.78, which as anticipated is close to unity because of the relative long wave. It is noticed that the reflection coefficient is larger that the one obtained in the vertical wall experiments (see Figure 4-7). A possible explanation is that the sloping wall was better sealed around the edges than the vertical wall.

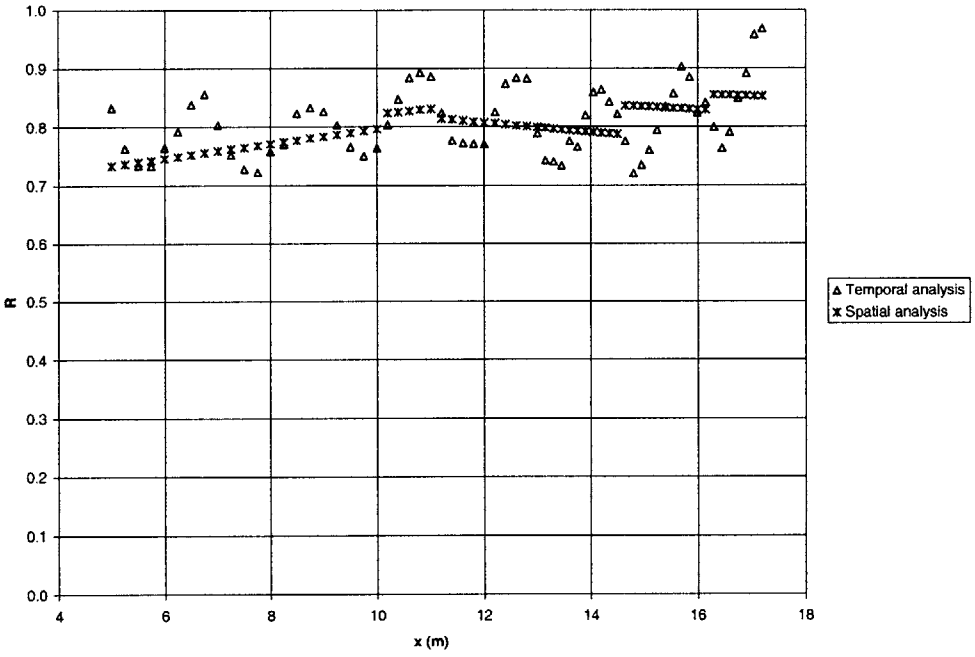

Figure 5-7 Cross-shore variation of reflection coefficient

5.3 Breaking wave experimental results

In the breaking wave experiments, the wave period is 2.05 seconds and the water depth in the constant depth region is 50 cm. The breaking of the waves occurred visually around x = 11.8 m and the breaker can be classified as the spilling type. The breakers tend to overshoot and are more violent than those in the no-structure experiments because of the considerable reflection. With reflection clearly evident, the incident wave height in the

constant depth region is about 19 cm, which is nearly the same as the value for the no-wall and vertical wall breaking wave experiments. Therefore, the results here should be directly comparable with the no-wall and vertical wall breaking results. The measurements were taken at the same locations as in the non-breaking wave experiments. At each station, a three-minute record of both surface displacement and velocity was taken.

5.3.1 Wave records and frequency spectra

The wave records are quite periodic although the waves are non-linear. It is of interest to examine the surface displacement and horizontal velocity immediately after the break point, which is from x = 12.4 m (right after breaking) and shown in Figure 5-8.

Figure 5-8 (a) depicts the time series of the surface displacement, from which periodicity is obviously seen. However, there are other frequency components contained in the record, as we can see from the spectrum (b). Similar phenomena are present in the horizontal velocity record (c) and the corresponding spectrum (d). It is, however, noticed that the first harmonics dominate higher harmonics, with the first to second harmonic ratio being greater than 2.

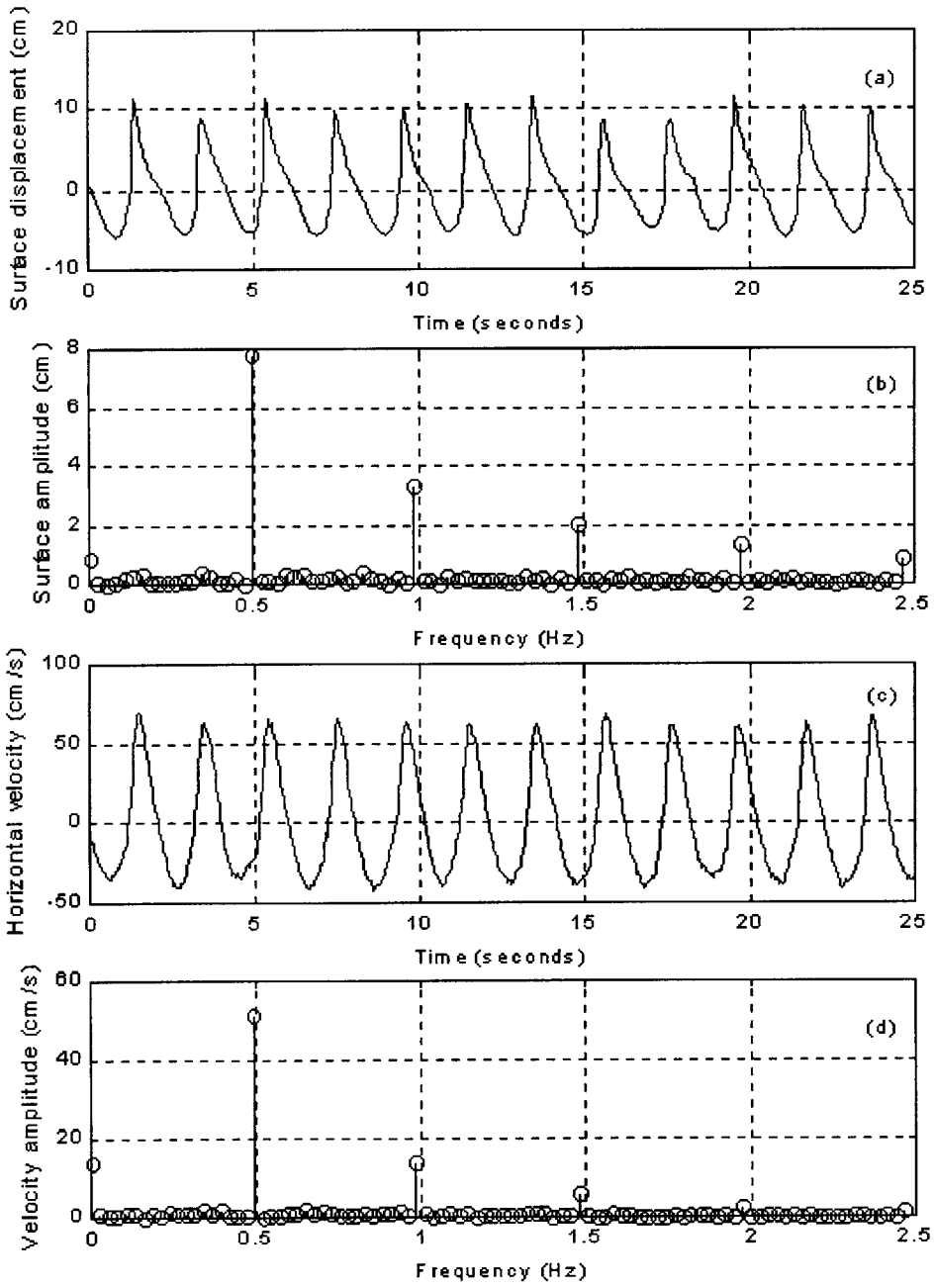

Figure 5-8 Wave records and frequency spectra at x = 12.4 m, right after breaking; (a) surface displacement, (b) surface amplitude spectrum, (c) horizontal velocity record, (d) velocity amplitude spectrum. Note: only the first 96 points are shown in the spectra.

5.3.2 Cross-shore variation of wave amplitude and velocity

Figure 5-9 shows the variation of several representative values of wave amplitude, A_1, A_e, A_{wr}, which are defined as in the non-breaking wave experiments and the experiments without a wall. Figure 5-10 shows the variation of horizontal velocities, U_1, U_e and U_{wr}, which are the corresponding values to A_1, A_e and A_{wr}. Note that the sloping lines (denoted by "Wall") in Figures 5-9, 5-10 and the following figures signify sloping-wall results, but do not represent the actual sloping wall. Only the starting point at x = 17.8 m signifies the toe of the sloping wall.

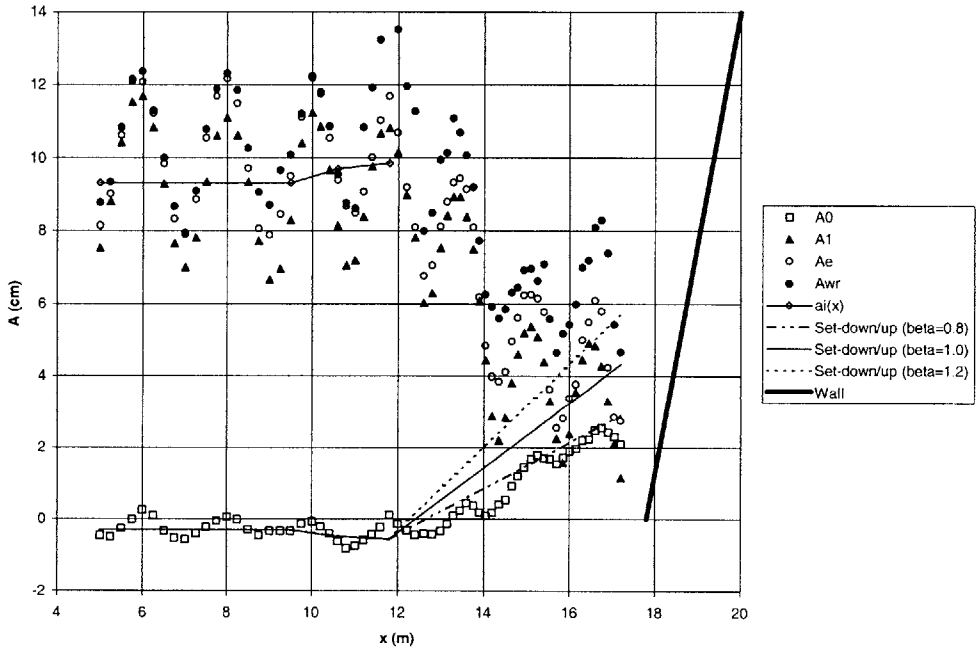

Figure 5-9 Cross-shore variation of wave amplitude. Note: the slope of the wall is not scaled.

It is noted that all the representative amplitudes in Figure 5-9 are close to one another, within a difference of 10% to 15%. It is seen from the figure that the average of the wave

amplitude starts dropping around x = 12 m, in agreement with the observed break point x = 11.8 m.

The incident wave amplitude accounting for shoaling, $a_i(x)$, is predicted using (3.11) and shown in Figure 5-9, with the constant depth portion's incident wave amplitude being the average obtained from temporal analysis (refer to Section 2.2.1) within the beat length from x = 6 m to x = 8 m, i.e., a_{ic} = 9.3 cm. Given the wave period T = 2.05 s and the still water depth in the constant depth region h_c = 50 cm, linear theory gives the group velocity C_{gc} = 173 cm/s and the wave length L = 418 cm. Thus, the incident waves correspond to $U = HL^2/h^3$ = 26, i.e., quite non-linear. C_{gc} and a_{ic} are then used in (3.11) to calculate the incident wave amplitude on the slope due to shoaling.

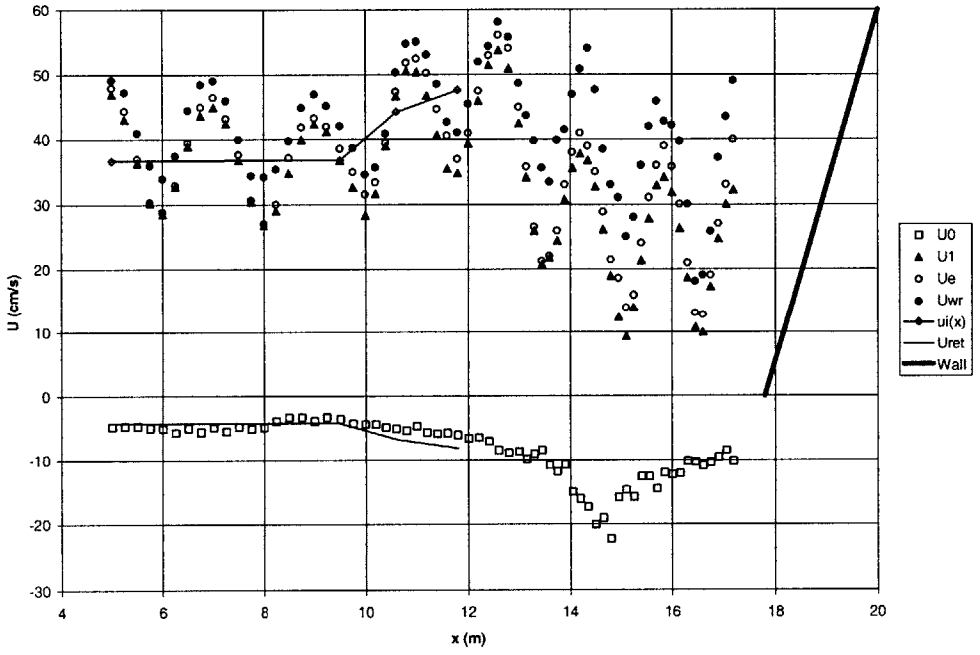

Figure 5-10 Cross-shore variation of horizontal velocity. Note: the slope of the wall is not scaled.

The clear waviness of A_1 throughout the wave channel is strong evidence of reflection, with the average remaining nearly constant in the constant depth region, increasing on the slope and then dropping after the break point. The maximum wave amplitude in Figure 5-9 appears around $x = 6$ m, $x = 8$ m and $x = 10$ m, and these locations correspond to minimum horizontal velocity amplitude in Figure 5-10. An estimate of reflection coefficient in the constant depth region can be made by taking the segment of the A_1 curve between $x = 6$ m and $x = 8$ m, that is $R \approx \dfrac{(A_1)_{\max} - (A_1)_{\min}}{(A_1)_{\max} + (A_1)_{\min}} = \dfrac{11.7 - 7.0}{11.7 + 7.0} = 25\%.$

This value is considerably lower than what we expected from the non-breaking wave results for the 1 on 1.5 sloping wall.

The predicted incident wave set-down/up calculated using (3.13), before the break point, and (3.14), after the break point, also agrees well with the measurements. After the break point, the three lines with different β values are drawn for comparison (see 3.14). It appears that the best β value is 0.8.

Figure 5-10 shows the horizontal velocity variation, with the same symbols as in the non-breaking wave experiments presented previously in this chapter and for the no-structure and vertical wall breaking wave experiments presented in Chapters 3 and 4, respectively. Again, the first harmonic velocity U_1 is fairly close to the energy velocity amplitude U_e and record velocity amplitude U_{wr}, while in the surf zone, U_1, still close to and U_e, deviates from U_{wr}. The velocity amplitudes all tend to drop at $x = 12$ m, similar to the wave amplitudes variation and visual observation of the break point. For comparison, the

predicted incident wave horizontal velocity calculated by (3.12), $u_i(x)$, is also shown in the figure.

The predicted incident wave return current U_{ret} obtained from (3.2) is in general agreement with the measurements up to the break point. It is interesting to notice that there is a transition region from x = 12 m to x = 14.5 m after the break point, followed by a developed undertow reaching –20 cm/s at x = 14.5 m and back to about –10 cm/s beyond x = 16.0 m. It is very similar to the return currents observed in the no-wall and vertical wall experiments shown in Figures 3-6 and 4-10, respectively.

5.3.3 Cross-shore variation of incident and reflected wave characteristics

Figure 5-11 shows the spatial curve fitting of the first harmonic wave amplitude in which the circles stand for the measurements with the solid line being the prediction.

The variation of incident wave amplitudes resolved from temporal and spatial analyses, described in Sections 2.2.1 and 2.2.2, respectively, is shown in Figure 5-12. For comparison, the predicted incident wave amplitude and the first harmonic incident wave amplitude, dotted trend line, and the predicted $a_i(x)$ are also shown in the figure.

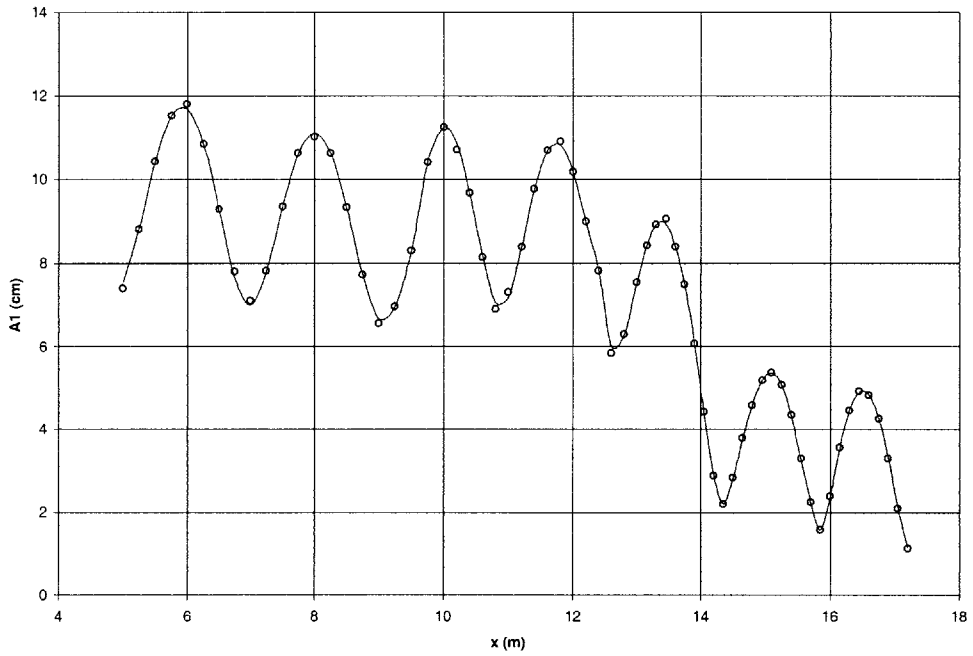

Figure 5-11 Spatial curve fitting of the first harmonic wave amplitude

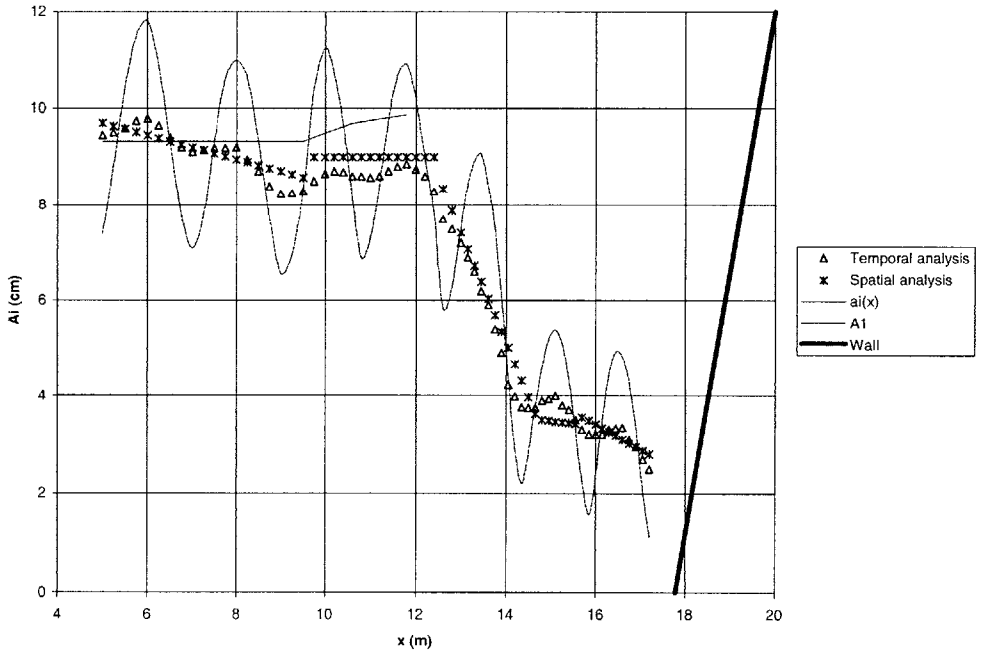

Figure 5-12 Cross-shore variation of incident wave amplitude. Note: the slope of the wall is not scaled.

The temporal and spatial analyses are in excellent agreement in Figure 5-12. They both decay gently in the constant depth region, then remain constant on the slope, start dropping sharply from x = 12.0 m to x = 14.2 m, and decay more gently again beyond x = 14.2 m. This general behavior is also seen in Figure 3-7 for the no-structure experiments and in Figure 4-12 for the vertical wall experiments.

The still water depth is 18.8 cm at the last antinode of the measurement (x = 16.6 m), corresponding to a beat length of 1.35 m given the wave period of 2.05 s. The still water depth at the seawall (x = 17.8 m) is 15.0 cm which corresponds to a beat length of 1.21 m. Therefore, the next antinode following the one at x = 16.6 m should be located between x = 17.81 m and x = 17.95 m, which is in agreement with the anticipation that an antinode should be located within the stretch of the seawall, that is, from x = 17.8 m to x = 17.8 + 0.23 = 18.03 m (The value of 0.23 m, the projection length of the seawall onto the x-axis, is obtained from the still water depth at the x = 17.8 m divided by the slope, i.e., 15 cm /(1/1.5) = 22.5 cm = 0.23 m).

The reflected wave amplitude variation in Figure 5-13 shows organized waviness demonstrated by the dotted line, the beat length being half the incident wave length again. The spatial results are somewhat larger than those obtained from temporal analysis, although they are fairly close. The reflected waves beyond the break point do not appear to differ very much from those before breaking, with the mean remaining nearly unchanged and the amplitude increasing a little, probably due to increased nonlinearity of the waves. At x = 17.2 m, the Ursell number associated with the reflected wave is

$U = H_r L^2 / h^3$ = 38.3 with reflected wave height H_r = 2.8 cm, wave length L = 257 cm and the water depth h = 16.9 cm.

For comparison, the predicted reflected wave amplitude accounting for shoaling, $a_r(x)$ is predicted using (4.1) and shown in Figure 5-13, with the constant depth portion's reflected wave amplitude being the average obtained from temporal analysis within the beat length from x = 6 m to x = 8 m, i.e., a_{rc} = 2.1 cm. Given the wave period T = 2.05 s and the still water depth in the constant depth region h_c = 50 cm, linear theory gives the group velocity in the constant depth region C_{gc} = 173 cm/s. C_{gc} and a_{rc} are then used in (4.1) to calculate the reflected wave amplitude due to shoaling.

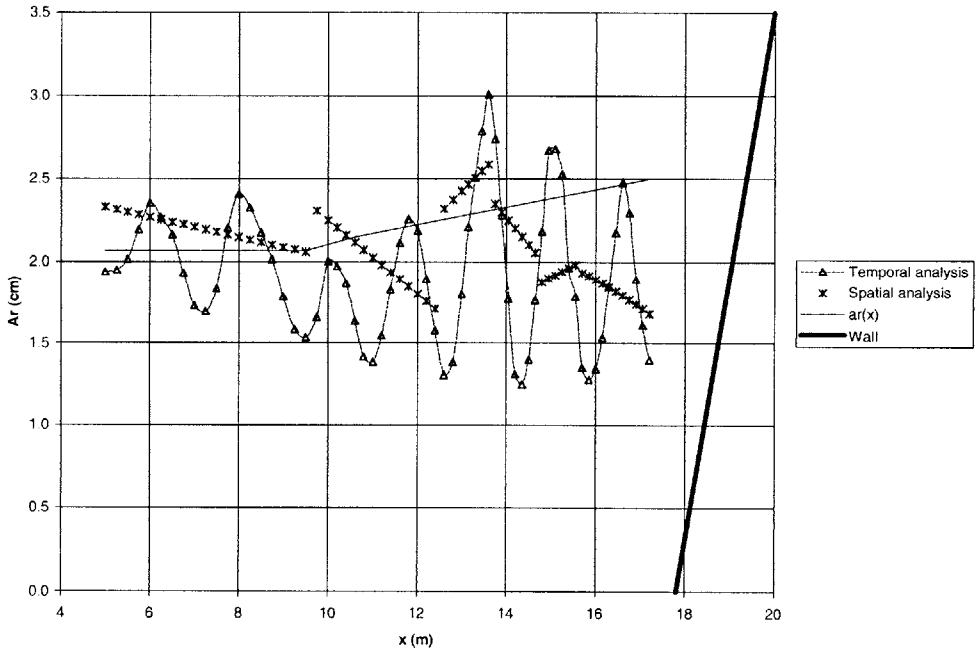

Figure 5-13 Cross-shore variation of reflected wave amplitude. Note: the slope of the wall is not scaled.

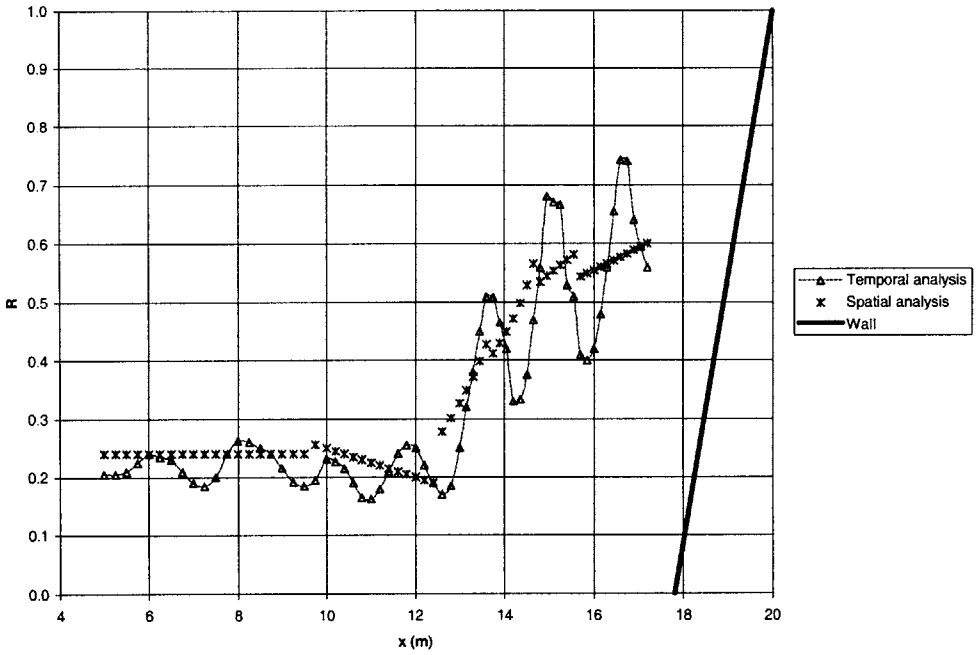

Figure 5-14 Cross-shore variation of reflection coefficients. Note: the slope of the wall is not scaled.

It is of interest to examine the variation of reflection coefficients which is shown in Figure 5-14. Despite the waviness of temporal results, they agree well with those obtained from the spatial analysis. The reflection coefficient fluctuates around 0.22 in the constant depth region up to the break point, where it starts to increase dramatically to about 0.56 at x = 17.2 m which is near the seawall located at x = 17.8 m. It is noted that the reflection coefficient immediately in front of the wall varies around 0.7, which is close to the value obtained from the non-breaking waves shown in Figure 5-7 ($R \cong$ 0.78). The increase in reflection coefficient is largely due to the dramatic drop of incident wave height beyond the break point, as seen in Figure 5-12, and the near-constancy of the reflected wave amplitude shown in Figure 5-13.

In Figure 5-14, the last antinode of the measurement is located at x = 16.75 m, 1.17 m away from the center of the seawall. This value is in general agreement with the beat length (1.21 m) at the seawall, as discussed previously in this chapter.

5.3.4 Behavior after breaking

It is of importance to examine the behavior of incident and reflected waves after breaking. The incident wave height (denoted by circles), along with the still water depth (denoted by squares) and still water depth plus set-up (denoted by triangles) is shown in Figure 5-15 where the full symbols are the values well beyond the break point (x > 14.5 m) and the straight lines are the linear best fit to these values. Since the constant depth portion's water depth (50 cm) is the same as that in no-structure experiments, results here should therefore be directly comparable for the still water level intersection, etc. The still water level intersects the beach at x = 22.56 m with R^2 = 0.998. The intersections of the mean water level and the incident wave height with be beach are located at x = 24.72 m (R^2 = 0.989) and x = 23.40 m (R^2 = 0.824), respectively. These values are fairly close to the no-structure results in which the still water level, the mean water level and the first harmonic incident wave height intersect with the beach at x = 22.56 m, x = 22.41 m and x = 23.33 m, respectively. The "rule" is still reasonable that the wave height varies linearly with water depth beyond breaking.

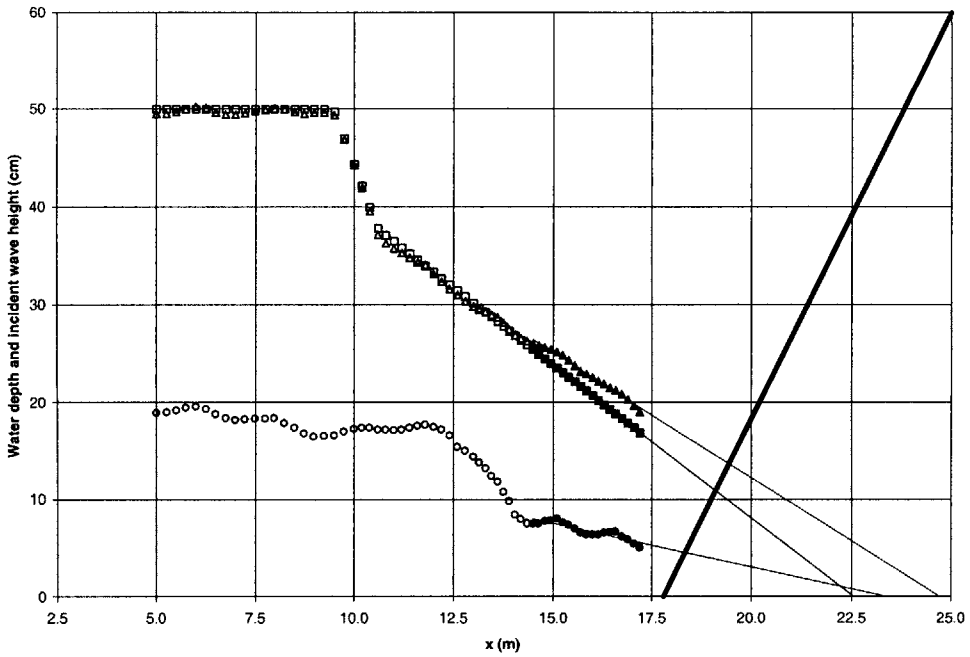

Figure 5-15 Variation of incident wave height and water depth; the triangles stand for still water depth plus set-up $h_+ = h + A_0$; the squares being the still water depth h; the circles the incident first harmonic wave height H_{i1}; and the full symbols for data well beyond the break point (x > 14.5 m). Note: the slope of the wall is not scaled.

Like we did in Chapter 3, we now establish a horizontal axis, "X", with zero at x = 24.72 m, the intersection of still water level and the beach, and positive direction seaward, i.e., $X = 24.72 - x$. The X -axis is then non-dimensionalized by the position of the visually observed breaking point X_B = 12.92 m. The total first harmonic wave height H_1, the energy wave height H_e, and the record wave height H_{wr} normalized by total water depth are plotted in Figure 5-16 for comparison.

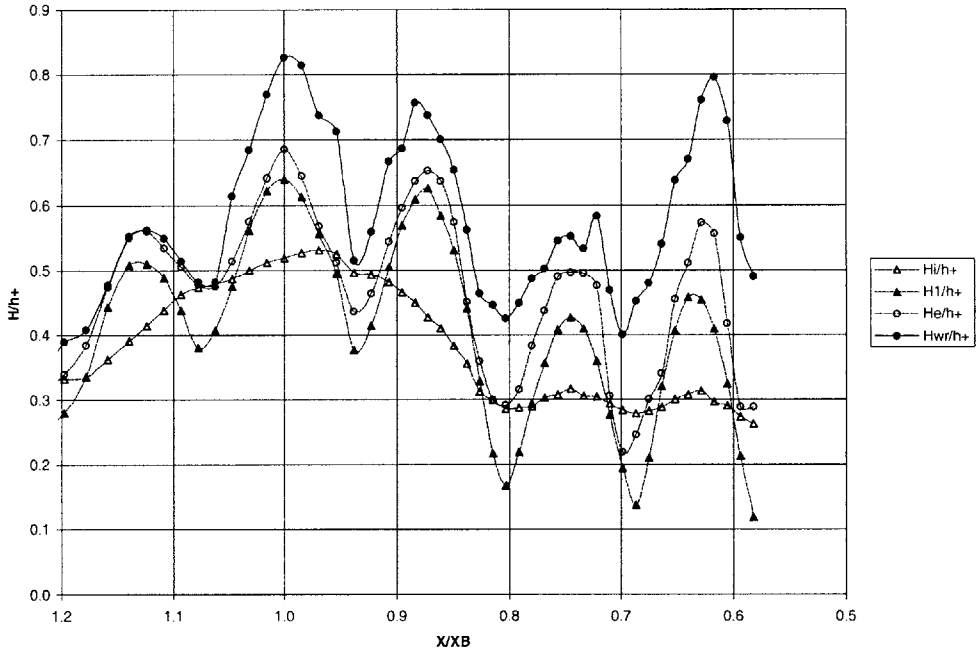

Figure 5-16 Variation of wave height non-dimensionalized by total water depth h_+

All the H/h_+ curves exhibit organized waviness. It is noticed that the waves broke at x = 11.8 m, an antinode, which is in agreement with the incident wave amplitude data suggestion of breaking (see also Figure 5-12) and the visual observation during the experiment. At the break point, $(H_{wr}/h_+)_B$ (subscript "B" denoting breaking point) gives a maximum value of 0.83, whereas $(H_e/h_+)_B$, $(H_1/h_+)_B$ and $(H_{i1}/h_+)_B$ are 0.69, 0.64 and 0.51, respectively. The predicted non-dimensional incident wave height $(H_i(x)/h_+)_B$ = 0.58 with $H_i(x)_B = 2a_i(x)_B$ = 19.7 cm (see Figure 5-9). $(H_{wr}/h_+)_B$ and $(H_{i1}/h_+)_B$ are fairly close to those values obtained from the no-wall experiments in which $(H_{wr}/h_+)_B$ = 0.85 and $(H_{i1}/h_+)_B$ = 0.48 whereas $(H_e/h_+)_B$ and $(H_1/h_+)_B$ appear to be greater than those in the no-wall experiments in which $(H_e/h_+)_B$ = 0.61 and $(H_1/h_+)_B$ = 0.49.

However, at the break point, all of the non-dimensional representative wave amplitudes obtained for the sloping wall are smaller than those obtained in the vertical wall breaking wave experiments in which $(H_{wr}/h_+)_B = 0.87$, $(H_e/h_+)_B = 0.78$, $(H_1/h_+)_B = 0.72$ and $(H_{i1}/h_+)_B = 0.58$.

When the average of high value at breaking and the subsequent low value is taken, $(H_{wr}/h_+)_B$, $(H_e/h_+)_B$, $(H_1/h_+)_B$ and $(H_{i1}/h_+)_B$ give 0.68, 0.57, 0.51 and 0.50, respectively. Compared with the no-wall experiments, they are in general agreement except for $(H_{wr}/h_+)_B$. Again, they are smaller than the values obtained in the vertical wall breaking wave experiments where the average $(H_{wr}/h_+)_B$, $(H_e/h_+)_B$, $(H_1/h_+)_B$ and $(H_{i1}/h_+)_B$ give 0.86, 0.64, 0.57 and 0.54, respectively.

The average lines of all H/h_+ curves start to decay beyond breaking and remain essentially constant with $(H_{i1}/h_+)_{B+} = 0.31$, $(H_1/h_+)_{B+} = 0.31$, $(H_e/h_+)_{B+} = 0.38$ and $(H_{wr}/h_+)_{B+} = 0.57$ where the subscript "B+" denotes the data well beyond breaking, i.e., $X/X_B < 0.76$. They are close to the no-structure experimental results in which $(H_{i1}/h_+)_{B+} = 0.36$, $(H_1/h_+)_{B+} = 0.39$, $(H_e/h_+)_{B+} = 0.44$ and $(H_{wr}/h_+)_{B+} = 0.56$ and the vertical-wall breaking wave experimental results in which $(H_{i1}/h_+)_{B+} = 0.34$, $(H_1/h_+)_{B+} = 0.39$, $(H_e/h_+)_{B+} = 0.43$ and $(H_{wr}/h_+)_{B+} = 0.69$.

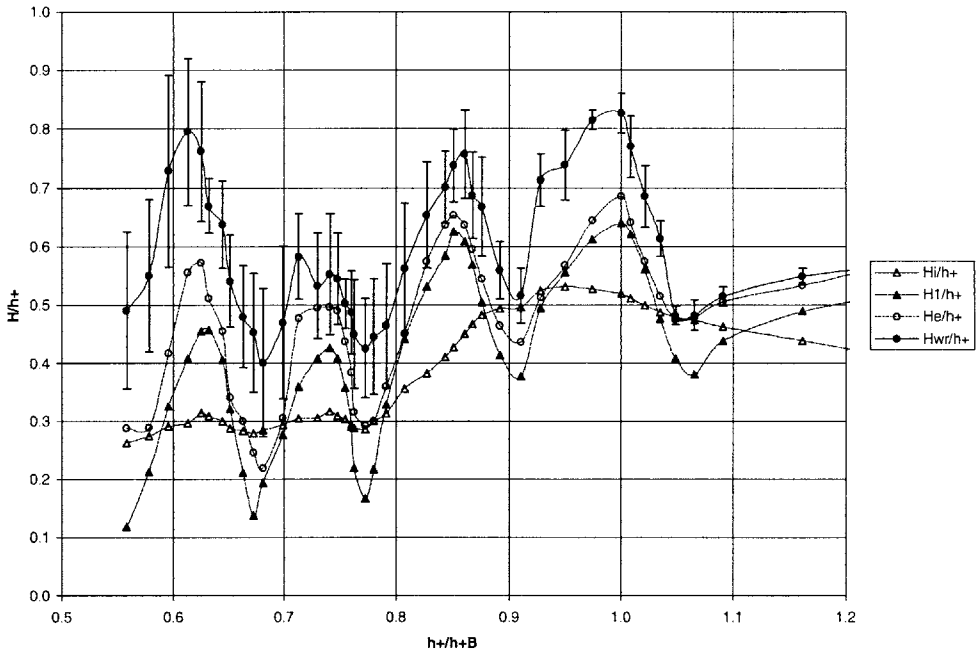

Figure 5-17 Wave height variation with water depth

In Figure 5-17, the horizontal axis is the total water depth non-dimensionalized by that of the breaking point h_{+B} = 34.1 cm at x_B = 11.8 m. The error bars on H_{wr}/h_+ show the standard deviation. In the surf zone, the wave record is somewhat difficult to measure as discussed in Section 3.2 and this is reflected in the relatively large variability of the H_{wr}/h values beyond breaking, i.e., when $h_+/h_{+B} < 1$. The average non-dimensional incident wave height, after reaching a maximum of 0.52, tends to decay sharply and then remain nearly constant at 0.31 within a beat length despite the waviness caused by high reflection.

Another experiment with shallower water depth (38.6 cm in the constant depth region) was also conducted and the results are presented in the Appendix C.

5.3.5 Comparison with experimental results in the absence of highly reflecting structures and in the presence of vertical seawalls

The purpose of the experiments is to investigate the potential influence of a highly reflecting seawall in the surf zone on the dissipation of incident wave energy after breaking. It is therefore of particular interest to compare the breaking wave results in the presence of a sloped wall with those obtained in the absence of highly reflective structures, presented in Chapter 3, and with the breaking wave results obtained in the presence of a vertical seawalls, presented in Chapter 4.

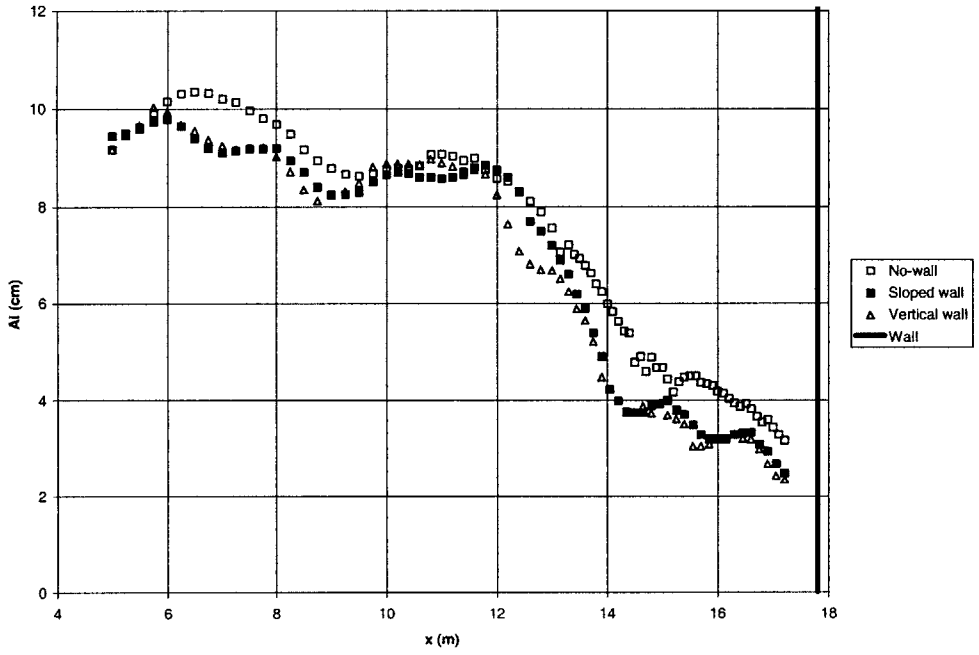

Figure 5-18 Comparison of incident wave amplitudes obtained from no-wall, vertical-wall and sloped-wall experiments. Note: the toe of the sloped wall is located at the same position as the vertical wall.

The incident wave amplitudes resolved from no-seawall experiments are plotted in Figure 5-18 together with the sloping-wall and vertical-wall experimental results. In the no-wall experiments, the waves broke visually at x = 13.1 m, however, the incident wave amplitude appeared to start decaying at 11.8 m which is well before the visually observed break point. The waves in the presence of a sloped wall and in the presence of a vertical wall both broke visually at x = 11.8 m, which coincides with the point where A_i begins to drop. It is noticed that the three curves have the same trend, i.e., all decaying dramatically around x = 12.0 m and then decreasing gently beyond x = 15 m. Therefore, the incident waves do not appear to be significantly affected by the presence of a highly reflective structure.

The comparison of non-dimensional incident wave height in the no-seawall, sloping-wall and vertical-wall experiments is shown in Figures 5-19. Note that the "break point" in the no-wall experiment is different from the definition described previously in Chapter 3. As seen from Figure 3-7, the incident wave amplitude begins to drop at x = 11.8 m, which coincides with the break points in the vertical-wall and sloping-wall experiments. Therefore in the following analysis, the break point is adopted as the point where the incident wave amplitude starts decaying. At the break point, the non-dimensional incident wave height is 0.52 (no-wall), 0.52 (sloped-wall) and 0.58 (vertical-wall), respectively. It is of importance to note that the behavior of the three curves beyond the break point shows the same trends, decaying rapidly immediately after breaking and remaining essentially constant well beyond the break point. The non-dimensional wave height fluctuates around 0.36 for the no-wall experiments, 0.31 for the sloped-wall experiments

and 0.34 for the vertical-wall experiments. The break point and the initial rapid decay may not be in agreement, but once we get well within the surf zone, i.e., when $H_i / h_+ \cong$ constant, the general agreement of the three curves is encouraging.

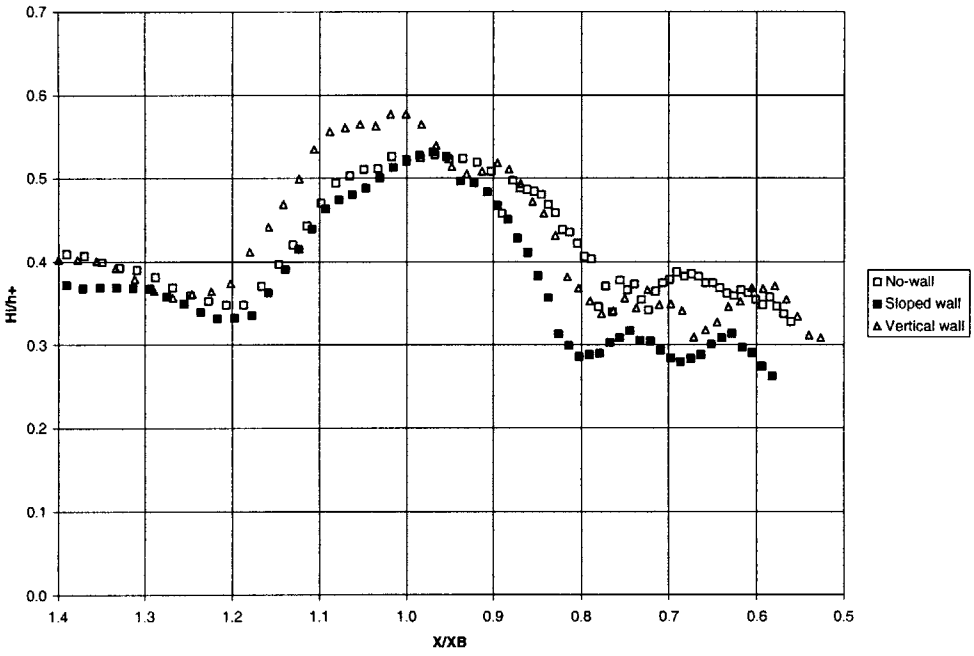

Figure 5-19 Comparison of incident wave height variation near breaking

Through the comparison of incident wave heights obtained from the no-structure breaking wave, sloping-wall breaking and vertical-wall breaking wave experiments, we do not see strong evidence that incident waves after breaking are affected significantly by the presence of a seawall. From the comparison of reflected wave heights obtained from non-breaking and breaking wave experiments in the presence of a seawall, we furthermore conclude that the reflected wave is not affected by the seawall, either, i.e., the reflected waves do not appear to lose energy as they travel seaward from the seawall whether they pass through a surf zone or not on their way.

Chapter 6

Conclusions

The purpose of this study is to investigate the potential influence of a highly reflecting seawall in the surf zone on the dissipation of incident wave energy after breaking. Therefore, sets of experiments were performed, in the absence of highly reflective structures, in the presence of vertical seawalls and in the presence of sloping seawalls, respectively. The no-structure breaking wave experiments provide baseline data of incident wave energy dissipation. The non-breaking wave experiments in the presence of vertical or sloping seawalls provide reflecting characteristics of the structure. The incident wave characteristics, reflected wave characteristics and the reflection coefficients resolved using linear theory from the breaking wave experiments in the presence of seawalls are then used to compare with those obtained from the no-structure breaking wave experiments and examine potential influence by the presence of seawalls. For direct comparison, all the experiments were carried out under nearly the same wave conditions, i.e., the constant depth portion's still water depth is 50 cm, wave period is around 2.05 seconds and the incident wave height in the breaking wave experiments is about 19 cm.

The predicted wave set-down/set-up calculated using the formulae (3.13) before wave breaking and (3.14) after wave breaking (Svendsen and Jonsson, 1976) agrees reasonably

well with the measurements. The parameter β (ratio of wave height to water depth) in (3.14) is about 0.8.

The predicted return current calculated by (3.2) also agrees well with the measurements. It is noticed that there is a transition region after the break point. The absolute value of return current increases to some point and then decreases again. This is the undertow introduced by the breaking waves.

The experiments also demonstrated that different definition of representative wave heights could yield different results for the breaking point and the breaking criterion.

Through the comparison of reflected wave height obtained from non-breaking and breaking wave experiments in the presence of highly reflective seawalls, we conclude that the reflected wave is not affected by the seawall, i.e., the reflected waves do not appear to lose energy as they travel seaward from the seawall whether they pass through a surf zone or not on their way.

After examining the behavior of the incident wave energy dissipation obtained from the no-structure breaking waves, the vertical-wall breaking waves and the sloping-wall breaking waves experiments, we noticed that the break point may not be in agreement depending on the definition of breaking criterion, but the general behavior of the incident wave height, non-dimensionalized by the total water depth, is very similar. The non-dimensional incident wave height reaches a maximum of about 0.53 (predicted non-

dimensional incident wave height accounting for shoaling being about 0.63) at the break point, decays rapidly immediately after breaking up to about $X / X_B \cong 0.8$, then remains nearly constant at about 0.34 (see Figure 5-19). Given the beach slope of 1 on 30, the distance of initial rapid decay, $0.2X_B$, corresponds to $6h_B$ where h_B is the water depth at breaking. This is not in agreement with the model (Brown, 1996) that the incident wave height varies linearly with the water depth immediately after breaking. The new model is tentatively adopted for the incident wave energy dissipation and shown in Figure 6-1 together with the results obtained from the no-structure, vertical-wall and the sloping-wall experiments.

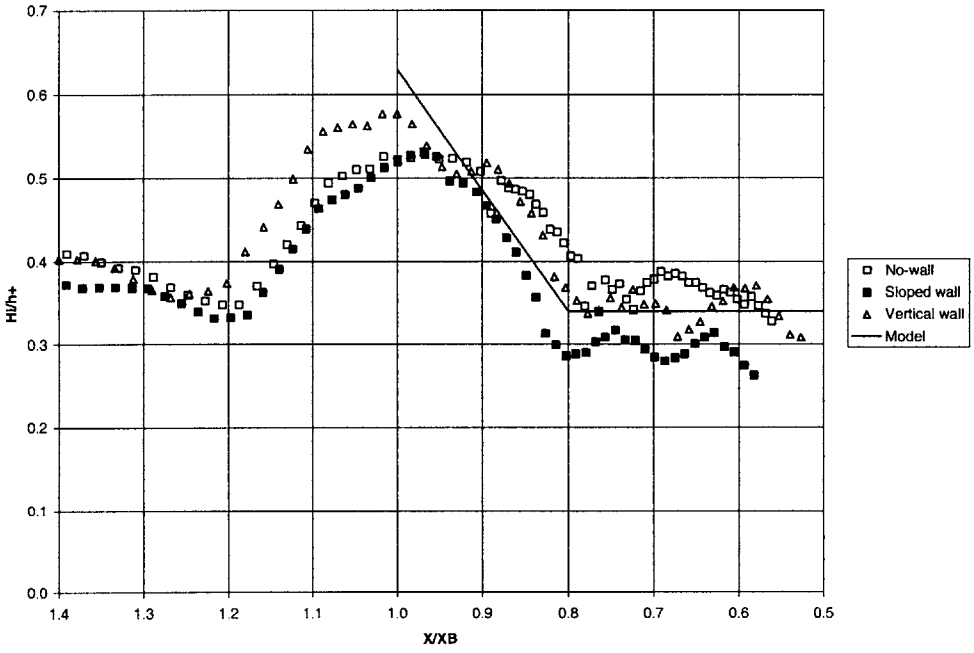

Figure 6-1 The incident wave energy dissipation model

6.1 Proposed model

Although limited by our experimental ranges, e.g., spilling breakers and wave period, the behavior of incident wave characteristics after breaking for the no-wall, vertical-wall and sloping-wall experiments shows general agreement, from which we have developed a tentative model of wave characteristics within the surf zone in the presence of highly reflecting structures.

(a) Incident wave height up to breaking

The incident wave is shoaled using linear theory up to the point of breaking.

(b) Break point

The break point is defined as the location where the incident wave height predicted from (a) is $0.63h$, where h is the still water depth.

(c) Set-up

Outside surf zone, wave set-up is obtained from Equation (3.13). Set-up within the surf zone is predicted from Equation (3.14) using $\beta = 0.8$.

(d) Incident wave height immediately after breaking

The wave height to total water depth ratio varies from a value of 0.63 at breaking to a value of 0.34 over a distance of approximately $6h_{+B}$ where h_{+B} is the total water depth at the break point. This is a generalization of our results which showed the region of rapid

decay to be of the order $0.2X_B$ where X_B is the surf zone width. It appears reasonable to expect the development distance to be proportional to the wave height or water depth. Thus, with the bottom slope in our experiments being approximately 1 on 30, the development distance of $6h_B$ would account for the effect of bottom slope.

(e) Incident wave in the fully developed surf zone

Beyond the transition region described in (d), the wave height to total water depth ratio remains constant and equal to 0.34.

(f) Reflected wave at the structure

The incident wave height, H_{is}, at the structure, is predicted from the structure's location within the surf zone using results of (e). With the reflection coefficient of the structure being R, the reflected wave height at the structure is $RH_{is} = H_{rs}$.

(g) Reflected wave characteristics

The reflected wave starting at the structure with $H_r = H_{rs}$ obtained in (f) is shoaled using linear theory into deeper waters to obtain $H_r(x)$.

(h) Prediction of wave orbital velocities

From knowledge of the incident (from (d) and (e)) and the reflected (from (f) and (g)) wave heights variation ($H_i(x)$ and $H_r(x)$) with proper attention to their phase, the wave orbital velocity variation can be predicted across the surf zone.

(i) Prediction of radiation stress gradient and wave-induced current

For waves incident to the coastline at a small angle of incidence we believe that the above-outlined model for wave characteristics may still be employed. This therefore results in prediction of the local radiation stress gradient, which drives the longshore wave-induced current. The bottom friction term's modification by the partially standing wave characteristics seaward of the structure is also obtained. Finally, the mean on-off shore wave-induced current may, up to the point of wave breaking, be predicted from the mass transport return current expression, Equation (3.2). In the fully developed surf zone, an undertow model, e.g., a modified version of the model by Meyer (1998), may be used to predict the near-bottom mean velocity. For the transition region from the breakpoint to the fully developed surf zone, a linear interpolation between these values is proposed.

The model proposed above is applied to the experiments conducted as part of this study in Appendix D. Although there are some differences between the measured and predicted breakpoint locations, the differences are very minor for the variations of the surface and orbital velocity amplitudes across the surf zone. The overall comparison is very encouraging.

Bibliography

Brown, J.S. (1996). Longshore currents on seawall-protected beaches. Masters Thesis, Department of Civil and Environmental Engineering, MIT.

Dally, W.R., R.G. Dean and R.A. Dalrymple (1985). Wave height variation across beaches of arbitrary profile. *Journal of Geophysical Research*, 90(C6):11917-11927.

Grant, W.D., O.S. Madsen (1979). Combined wave and current interaction with a rough bottom. *Journal of Geophysical Research*, 84 (C4):1979-1988.

Kraus, N.C., W.G. McDougal (1996). The effects of seawalls on the beach: Part I, An updated literature review. *Journal of Coastal Research*, 12(3):591-701.

Longuet-Higgins, M.S. (1970). Longshore currents generated by obliquely incident sea waves, 1&2. *Journal of Geophysical Research*, 75(33):6788-6801.

Longuet-Higgins, M.S. (1972). Recent progress in the study of longshore currents. In *Waves on Beaches*. R.E. Meyer, ed, Academic Press:203-248.

Madsen, O.S. Lecture notes of Basic Wave Theory. Ralph M. Parsons Laboratory, MIT.

Madsen, O.S., D.W. Ostendorf, and A.S. Reyman (1978). A longshore current model. *Proceedings Coastal Zone 78, ASCE*, San Francisco, 3:2332-2341.

Mathisen, P. (1989). Experimental study of the response of fine sediments to wave agitation and associated wave attenuation. Masters Thesis, Department of Civil and Environmental Engineering, MIT.

Mei, C.C. (1994). The applied dynamics of ocean surface waves. World Scientific Publishing Co. Pte. Ltd.:2-59.

Meyer, R.N. (1998). Modeling equilibrium beach profiles using a theoretical approach. Masters Thesis, Department of Civil and Environmental Engineering, MIT.

Moody, P.M. (1996). Laboratory study of the effects of sea walls on beach erosion. Masters Thesis, Department of Civil and Environmental Engineering, MIT.

Silvester, R. (1974). Coastal engineering, Part I. Generation, propagation and influence of waves. Elsevier Scientific Publishing Company:240-246.

Svendsen, I.A., I.G. Jonsson (1976). Hydrodynamics of coastal regions. Technical University of Denmark:236-245.

Appendix A

No-structure Experimental Results with Extensive Measurements in the Surf Zone

A.1 Overview of experiments

An experiment in the absence of seawalls was carried out with extensive measurements in the surf zone as mentioned in Chapter 3. The wave maker was run 10 minutes in order for stationarity to be established before measurements were taken. The still water depth in the constant depth region is 48.4 cm and the wave period is 2.05 seconds. The waves broke visually at x = 13.15 m and the breakers can be classified as the spilling type. A three-minute record of both water surface displacement and velocity was taken at 74 locations from x = 5.0 m to x = 18.8 m which was limited by the length of the ADV cable. The measuring interval in the constant depth region was 25 cm, while it shortened to 20 cm on the slope, and 15 cm near the toe of the seawall, respectively.

A.2 Experimental results

Figures A-1 and A-2 show the variation of wave amplitudes and horizontal velocities, respectively, with the same symbols used in Chapters 3, 4 and 5.

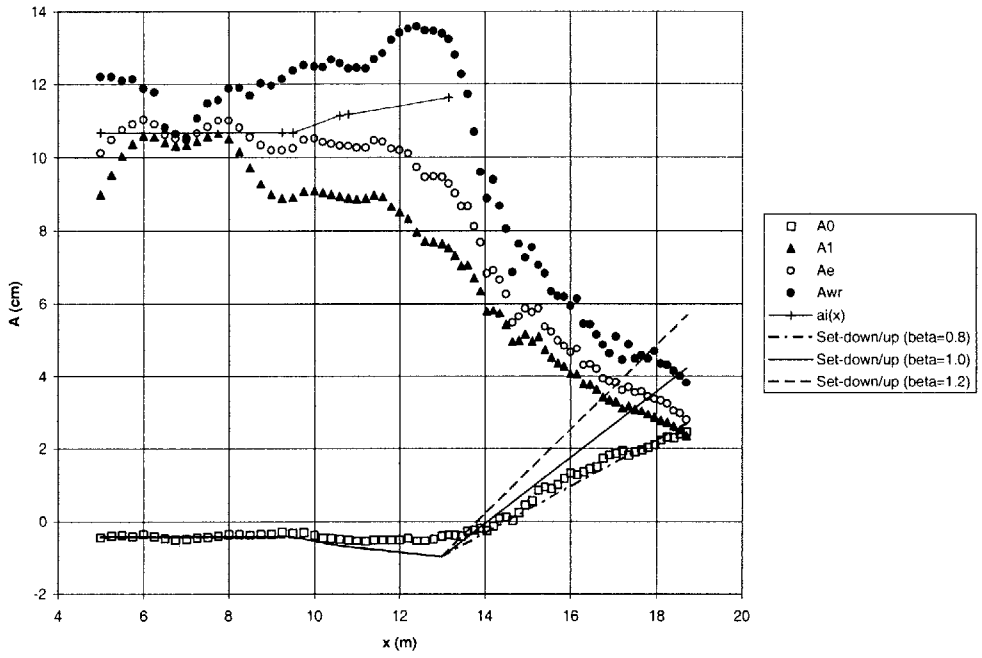

Figure A-1 Cross-shore variation of wave amplitudes

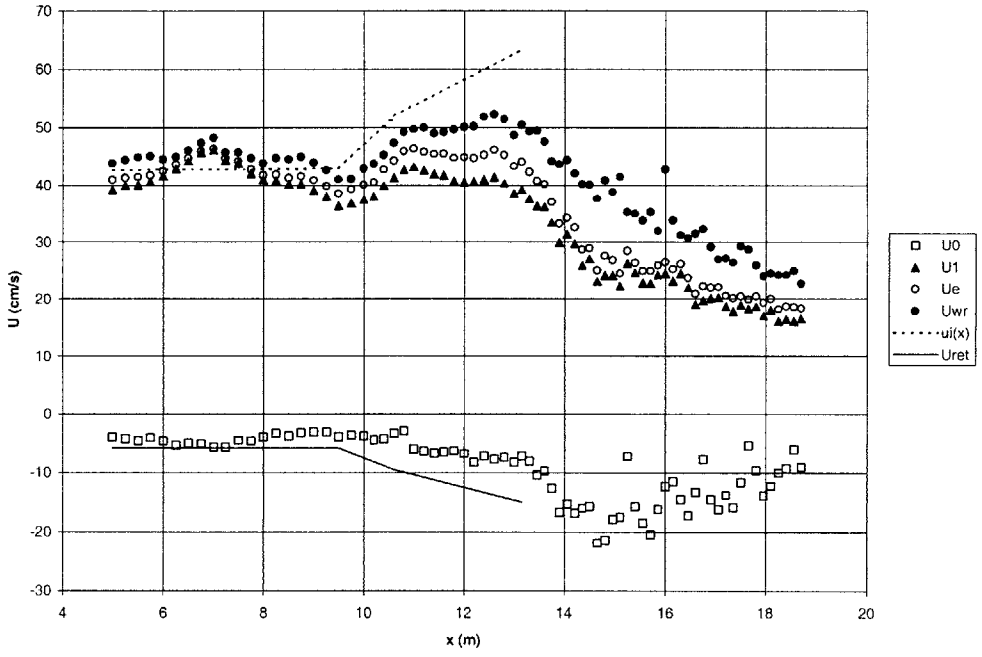

Figure A-2 Cross-shore variation of horizontal velocities

It is noticed that A_1 and A_e start to decay at x = 13.15 m (a local maxima), which is in agreement with the visually observed break point, whereas A_{wr} reaches a maxima at x = 12.4 m, and U_1, U_e and U_{wr} appear to decay at x = 12.6 m.

The constant depth portion's (x < 9.5 m) waviness of amplitude variation of A_1, A_e and A_{wr} is evidence of a small reflection. An estimate of reflection coefficient can be made by taking the segment of the A_e curve between x = 6 m and x = 8 m and the reflection coefficient is then $R \approx \frac{(A_e)_{\max} - (A_e)_{\min}}{(A_e)_{\max} + (A_e)_{\min}} = \frac{11.0 - 10.5}{11.0 + 10.5} = 2.3\% << 1$, as one would expect.

Given wave period T = 2.05 s, deep water wave length is $L_0 = gT^2/2\pi$ = 6.6 m and the group velocity is $C_{g0} = gT/4\pi$ = 160.0 cm/s. With incident and reflected wave amplitudes resolved from temporal analysis described in Section 2.2.1, the incident wave amplitude in the constant depth region, a_{ic} = 10.7 cm (subscript "c" denoting constant depth), is taken as the average within the beat length from x = 6 m to x = 8 m. With still water depth h_c = 48.4 cm, the group velocity C_{gc} = 171.8 cm/s in constant depth portion. The deep water wave height is $H_0 = H_{ic}\sqrt{C_{gc}/C_{g0}}$ = 23.8 cm where the incident wave height $H_{ic} = 2a_{ic}$ = 21.4 cm/s. With $\tan\alpha$ = 1/30 in our experiments, the parameter B_0 obtained by (3.9) turns out to be 32.5, indicating the breaker type of spilling, in agreement with the observation of breaker type.

With a_{ic} = 10.7 cm in the constant depth region, the incident wave amplitude due to shoaling, $a_i(x)$ calculated by (3.11) and the incident wave horizontal velocity due to shoaling, $u_i(x)$ calculated by (3.12), are also shown in Figures A-1 and A-2, respectively, for comparison.

The predicted incident wave set-down/set-up, calculated using (3.13) with $H = 2a_i(x)$ before breaking and (3.14) after breaking with β = 0.8, agrees well with measurements as seen in Figure A-1.

The predicted incident wave return current calculated using (3.2) with $H = 2a_i(x)$ is in general agreement with the measurements up to the start of the slope where the two values begin to deviate. The undertow created by breaking waves is clearly seen in the region from x = 13.3 m to x = 16.0 m. There is a transition from x = 13.3 m to x = 14.65 m over which the undertow strengthens to reach its maximum value of about 21.8 cm/s in the seaward direction. Beyond this point the undertow decreases in strength as a result of the decreased wave height.

The incident wave amplitude, A_{i1}, obtained from the temporal analysis (Section 2.2.1) of the first harmonic component, is shown in Figure A-3. For comparison the total first harmonic amplitude A_1 and the wave record amplitude A_{wr} are also presented in Figure A-3. The A_{i1} curve is very close to A_1, which shows that the reflected waves are indeed very small.

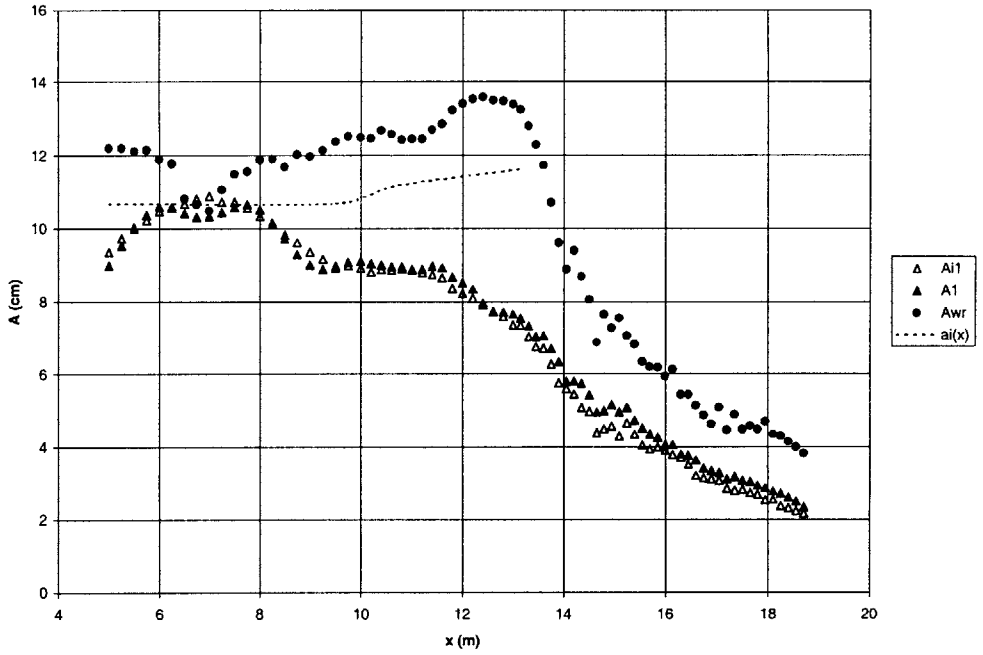

Figure A-3 Cross-shore variation of incident wave amplitude

As seen in Figure A-3, the incident wave amplitude decay rapidly after breaking up to x = 15.0 m, beyond which this decrease is more gentle. This behavior is very similar to the behavior of incident wave amplitude shown in Figure 3-7.

Figures A-4 and A-5 depict the variation of the reflected wave amplitude and the reflection coefficient obtained from the temporal analysis (Section 2.2.1). Again, the organized waviness from the constant depth region to the break point shows up (see dotted lines) as in Figures 3-8 and 3-9. The amplitude of A_{r1} is roughly 0.4 cm, so with $A_{i1} \cong 11$ cm, the reflection coefficient $R \cong 3.6\%$, in reasonable agreement with the value (2.3%) obtained from the raw data of A_e. The small reflection coefficient in constant depth region fluctuates by ± 0.03 around the mean value of 0.04, while this

average goes up to 0.12 after wave breaking, largely due to the decrease in incident wave amplitude and the near-constancy of the reflected wave amplitude.

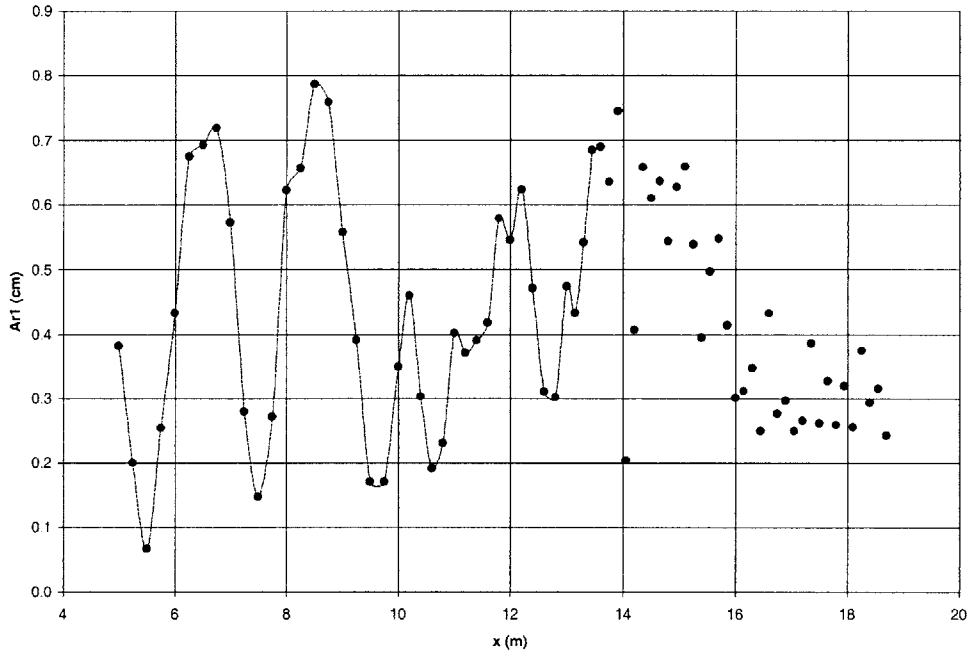

Figure A-4 Cross-shore variation of reflected wave amplitude

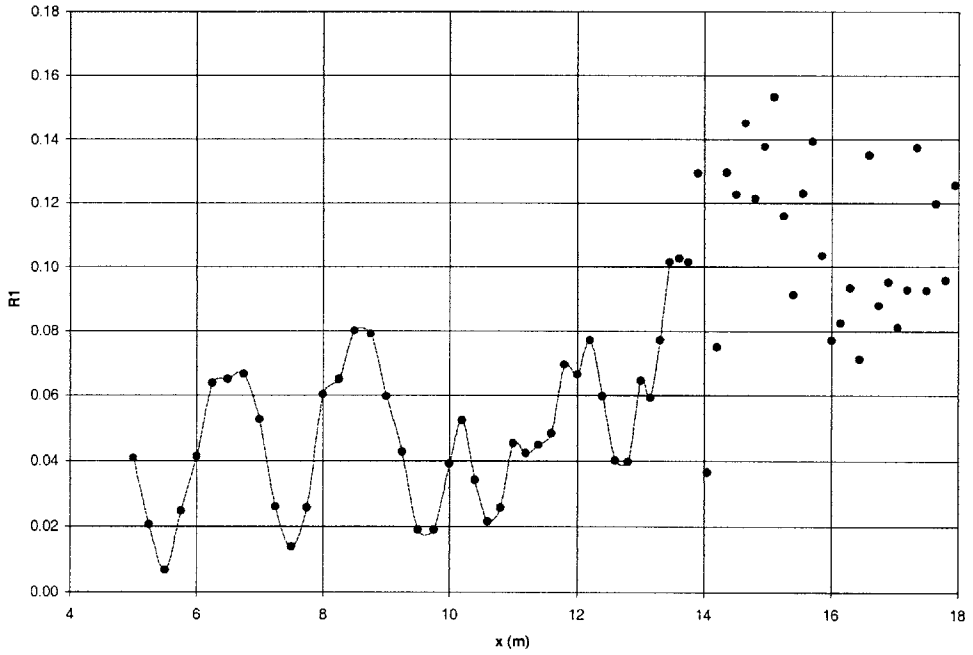

Figure A-5 Cross-shore variation of reflection coefficient

Figure A-6 shows the variation of the still water depth h (squares), the total water depth $h_+ = h + A_0$ (triangles) and the incident first harmonic wave height H_{i1} (circles). The full symbols stand for the data well beyond the break point (x > 15.1 m) and the straight lines are the linear best fit to these values. The best fit lines intersect with the beach at x = 22.05 m (R^2 = 0.998) for h, x = 23.61 m (R^2 = 0.998) for h_+ and x = 21.85 m (R^2 = 0.971). This is in general agreement with the "rule" that the ratio of wave height to the water depth H/h is constant within the surf zone.

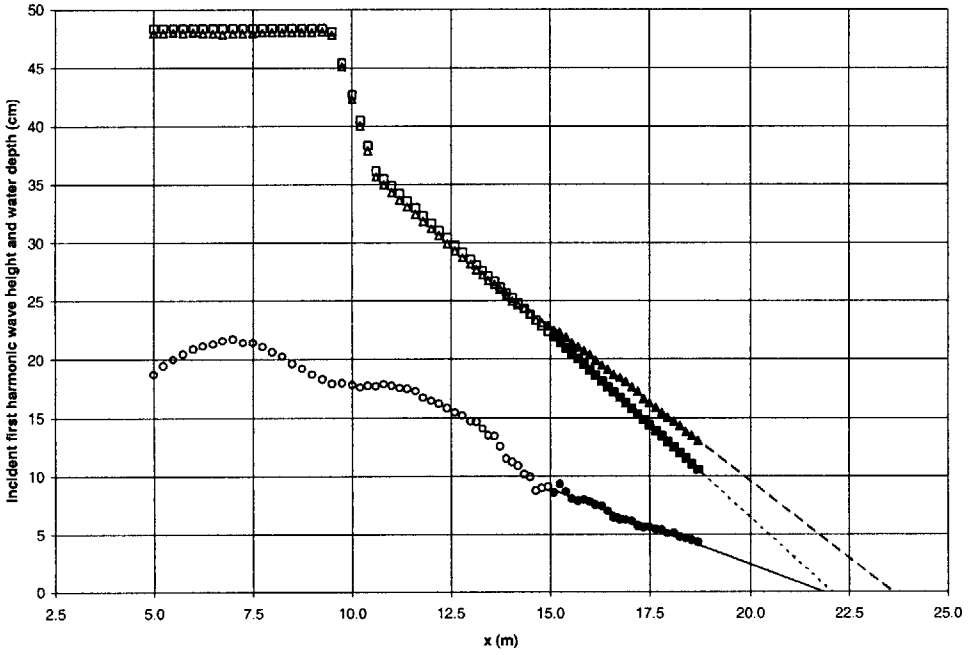

Figure A-6 Variation of water depth and incident wave height

To make this point more clearly, Figures A-7 and A-8 show the variation of non-dimensional wave height with X/X_B and h_+/h_{+B}, respectively.

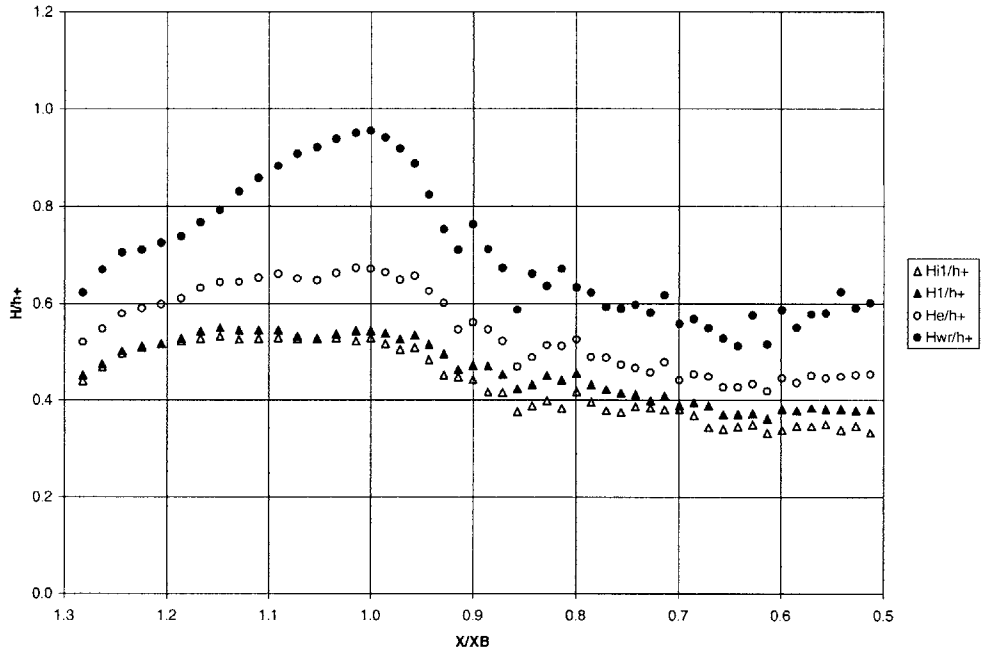

Figure A-7 Variation of wave height non-dimensionalized by total water depth h_+

In Figure A-7, we establish a horizontal axis, " X ", with zero at x = 23.61 m, the intersection of mean water level and the beach, and positive direction seaward, i.e., $X = 23.61 - x$. The X -axis is then non-dimensionalized by the position of the visually observed breaking point X_B = 10.47 m (x_B = 13.15 m). The total first harmonic wave height $H_1 = 2A_1$, the energy wave height $H_e = 2A_e$ and the wave record wave height $H_{wr} = 2A_{wr}$ normalized by the total water depth h_+, are also plotted in Figure A-7 for comparison.

It is obvious that all the H/h_+ curves climb to maxima as the visually observed break point is approached. The values of H/h_+ in the vicinity of the break point are of definite interest. If the record wave height H_{wr} is used for H, $(H/h_+)_B = 0.95$ is obtained at

breaking, denoted by the subscript "B". This value is larger than the widely used criterion of wave breaking, $(H/h_+)_B = 0.8$. However, non-dimensional energy wave height $(H_e/h_+)_B$, first harmonic total wave height $(H_1/h_+)_B$ and first harmonic incident wave height $(H_{i1}/h_+)_B$ give 0.67, 0.54 and 0.53, respectively, which all are substantially lower than the commonly used value of 0.8 and slightly bigger than the results presented in Chapter 3 where $(H_e/h_+)_B = 0.61$, $(H_1/h_+)_B = 0.49$ and $(H_{i1}/h_+)_B = 0.48$. After the break point, H_{wr}/h_+ drops dramatically and then remains approximately constant at a value of $H_{wr}/h_+ \cong 0.56$. H_e/h_+, H_1/h_+ and H_{i1}/h_+ all exhibit similar features to H_{wr}/h_+ with near-constant values of 0.45, 0.39 and 0.35, respectively following an initial drop after the break point. These values are virtually the same as the results described in Chapter 3 where $H_{wr}/h_+ \cong 0.56$, $H_e/h_+ \cong 0.44$, $H_1/h_+ \cong 0.39$, and $H_{i1}/h_+ \cong 0.36$ well beyond the break point. The behavior of the H_{i1}/h_+ after break point is in excellent agreement with our model of incident wave energy dissipation, i.e., the waves breaks when $H_{i1}/h_+ = 0.53$, decays dramatically from $X/X_B = 1$ to $X/X_B = 0.8$, and remains essentially constant at $H_{i1}/h_+ = 0.35$ (~ 0.34).

In Figure A-8, the horizontal axis is the water depth non-dimensionalized by that of the breaking point $h_{+B} = 27.72$ cm at $x_B = 13.15$ m. The solid circle on the H_{wr}/h_+ curve is plotted using the mean value of 10 successive wave heights obtained from the wave record divided by the total water depth. The error bars show the standard deviation of these 10 wave heights over total water depth. In the surf zone, the wave record is somewhat difficult to measure as we discussed in the previous Section 3.2, and this is

reflected in the relatively large variability of the H_{wr}/h_{+} values beyond breaking, i.e., when $h_{+}/h_{+B} < 1.0$.

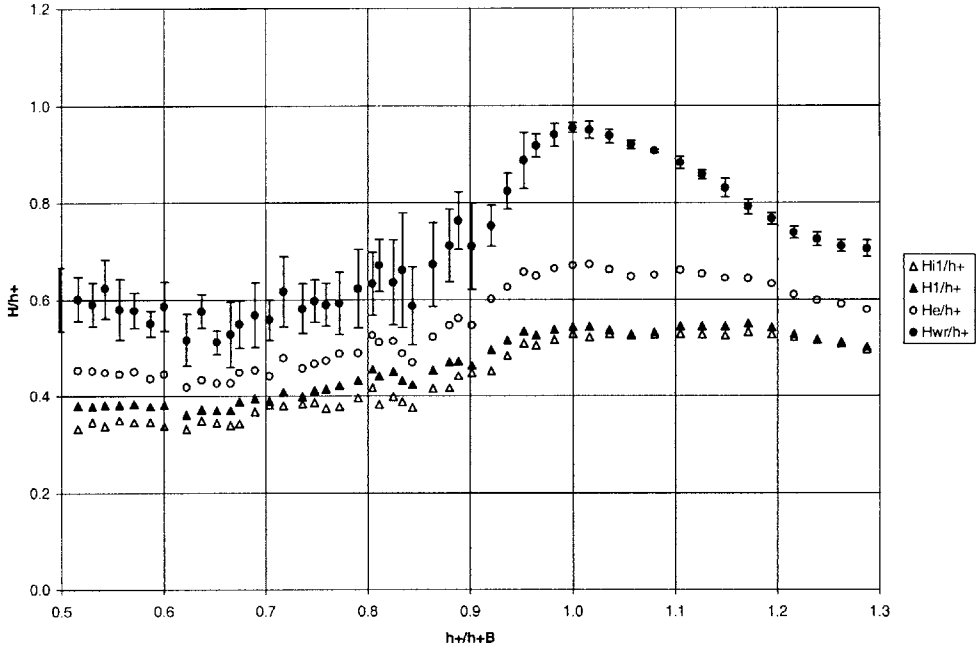

Figure A-8 Variation of non-dimensional wave height with total water depth h_{+}

Appendix B

Experimental Results with Lower Wave Height in the Presence of Vertical Seawalls

B.1 Overview of experiments

Two experiments with lower wave height (incident wave amplitude being about 8 cm) were carried out in the presence of a vertical seawall located at x = 17.8 m as mentioned in Chapter 4. In both experiments, the wave maker was run 15 minutes in order for stationarity to be established before measurements were taken. A three-minute record of both water surface displacement and velocity was taken at 77 locations from x = 5.0 to x = 17.2 m. The measuring interval in the constant depth region was 25 cm, while it shortened to 20 cm on the slope, and 15 cm near the toe of the seawall, respectively. The experimental results are presented in the following sections B.2 (experiment #1) and B.3 (experiment #2), respectively.

B.2 Experiment #1

In experiment #1, the still water depth in the constant depth region is 47.7 cm and the wave period is 2.03 seconds. The waves broke visually at x = 12 m and the breakers can

be classified as the spilling type. Figures B-1, B-2 and B-3 show the variation of incident wave amplitude, reflected wave amplitude and reflection coefficient with the same symbols used in Chapter 4, obtained from temporal (Section 2.2.1) and spatial (Section 2.2.2) analyses, respectively.

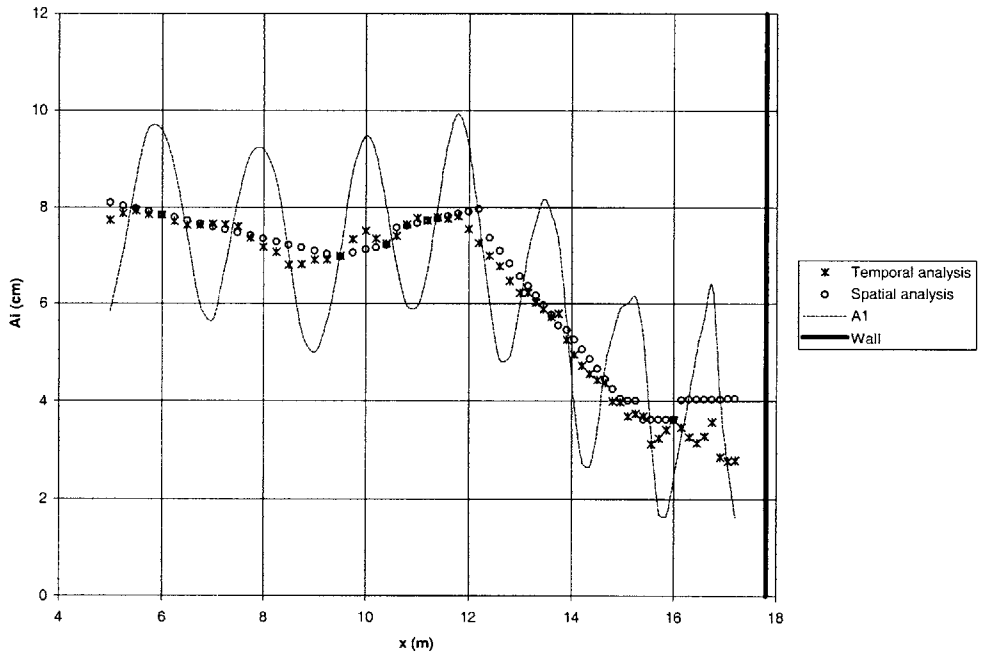

Figure B-1 Cross-shore variation of incident wave amplitude

Again, the temporal and spatial analyses give results in close agreement for A_i, A_r and R. The incident wave amplitude A_i decays in the constant depth region, then increases on the slope, drops dramatically after breaking up to x = 15 m followed by a gentle decay.

The still water depth is 16.0 cm at the last antinode of the measurement (x = 16.6 m), corresponding to a beat length of 1.32 m given the wave period of 2.03 s. The still water

depth at the seawall (x = 17.8 m) is 12.7 cm which corresponds to a beat length of 1.10 m. Therefore, the next antinode following the one at x = 16.6 m should be located between x = 17.70 m and x = 17.92 m, which is in good agreement with the anticipation that an antinode should be located at the seawall (x = 17.8 m).

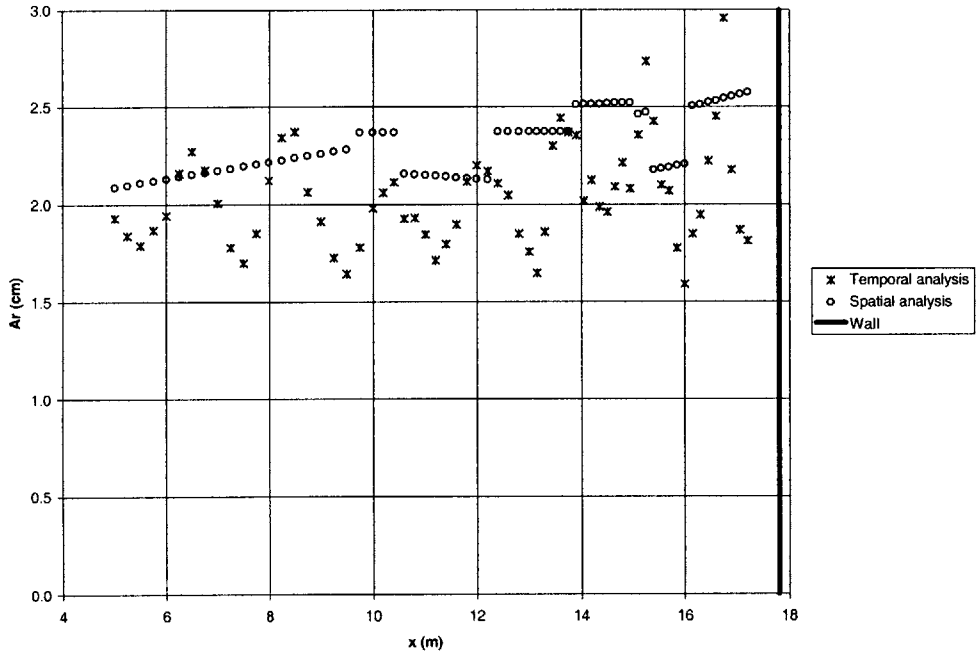

Figure B-2 Cross-shore variation of reflected wave amplitude

The reflected wave amplitude A_r varies from 1.7 cm to 2.4 cm in the constant depth region, and the average tends to increase on the slope. The reflection coefficient increases beyond the break point, reaching about 0.75 near the structure. The increase in reflection coefficient is largely due to the dramatic drop of incident wave height beyond the break point, as seen in Figure B-1, and the near-constancy of the reflected wave amplitude, shown in Figure B-2. In Figure B-2, the last antinode of the measurement is located at x

= 16.75 m, 1.05 m away from the seawall. This value is in general agreement with the beat length (1.10 m) at the seawall, as discussed previously in this section.

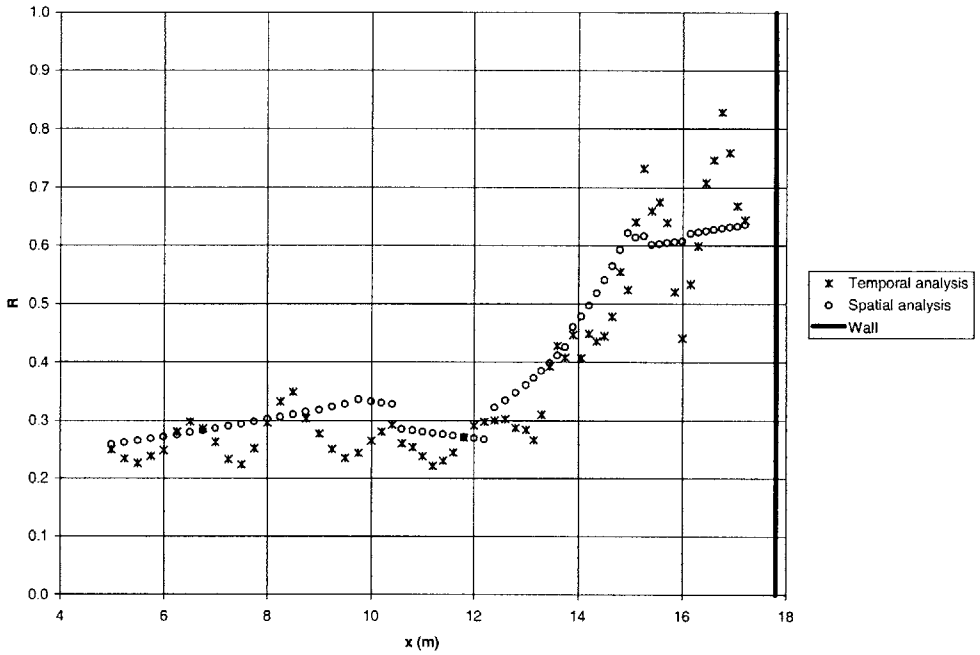

Figure B-3 Cross-shore variation of reflection coefficient

Figure B-4 shows the variation of the first harmonic incident wave height H_{i1} (denoted by circles), along with the still water depth h (denoted by squares) and still water depth plus set-up $h_+ = h + A_0$ (denoted by triangles). The full symbols are the values well beyond the break point (x > 14.95 m) and the straight lines are the linear best fit to these values. The still water level intersects the beach at x = 21.83 m with R^2 = 0.998. The intersections of the mean water level and the incident wave height with be beach are located at x = 23.30 m (R^2 = 0.982) and x = 24.50 m (R^2 = 0.629), respectively. The "rule" is still reasonable that the wave height varies linearly with water depth beyond breaking.

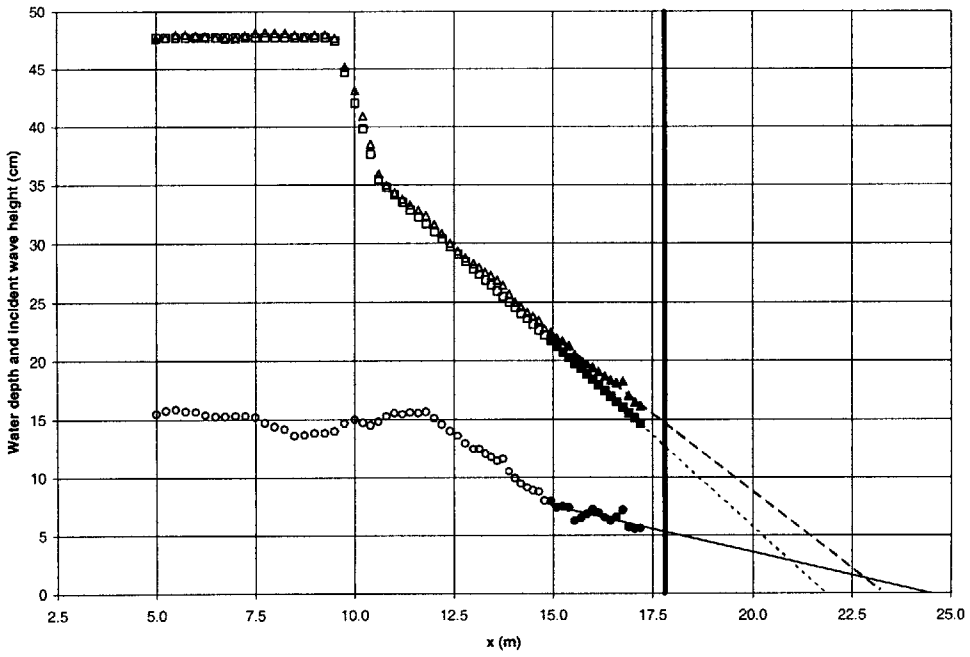

Figure B-4 Variation of water depth and incident wave height

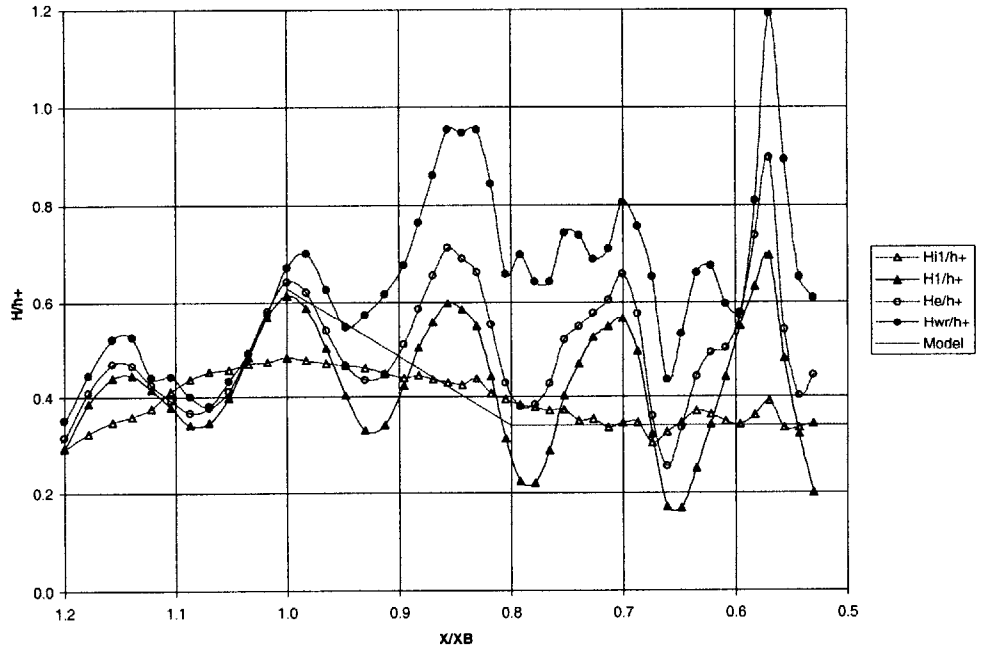

Figure B-5 Variation of wave height non-dimensionalized by total water depth h_+

In Figure B-5, we establish a horizontal axis, " X ", with zero at x = 23.30 m, the intersection of total water level and the beach, and positive direction seaward, i.e., $X = 23.30 - x$. The X -axis is then non-dimensionalized by the position of the visually observed breaking point X_B = 11.30 m. The total first harmonic wave height H_1, the energy wave height H_e and the record wave height H_{wr} normalized by total water depth are plotted in Figure B-5 for comparison.

All the H/h_+ curves exhibit organized waviness. It is noticed that the waves broke at x = 12.0 m, an antinode, which is in agreement with visual observation. At the break point, $(H_{wr}/h_+)_B$ (subscript "B" denoting breaking point) gives a maximum value of 0.67, whereas $(H_e/h_+)_B$, $(H_1/h_+)_B$ and $(H_{i1}/h_+)_B$ are 0.64, 0.61 and 0.48, respectively. However, when the average of high value at breaking and the subsequent low value is taken, $(H_{wr}/h_+)_B$, $(H_e/h_+)_B$, $(H_1/h_+)_B$ and $(H_{i1}/h_+)_B$ give 0.63, 0.54, 0.47 and 0.46, respectively, close to the results except for $(H_{wr}/h_+)_B$ obtained from the no-structure experiments in which $(H_{wr}/h_+)_B = 0.85$, $(H_e/h_+)_B = 0.61$, $(H_1/h_+)_B = 0.49$ and $(H_{i1}/h_+)_B = 0.48$. The average lines of all H/h_+ curves start to decay beyond breaking and remain essentially constant with $(H_{i1}/h_+)_{B+} = 0.35$, $(H_1/h_+)_{B+} = 0.39$, $(H_e/h_+)_{B+} =$ 0.49 and $(H_{wr}/h_+)_{B+} = 0.71$ where the subscript "B+" denotes the data well beyond breaking, i.e., $X/X_B < 0.75$. They are in good agreement with no-structure experiments (except for $(H_{wr}/h_+)_{B+}$) in which $(H_{i1}/h_+)_{B+} = 0.36$, $(H_1/h_+)_{B+} = 0.39$, $(H_e/h_+)_{B+} =$ 0.44 and $(H_{wr}/h_+)_{B+} = 0.56$.

It is noticed that the incident wave energy dissipation model presented in Chapter 6 is in agreement with the measurements.

B.3 Experiment #2

In experiment #2, the still water depth in the constant depth region is 46.1 cm and the wave period is 2.07 seconds. The waves broke visually at x = 11.8 m and the breakers can be classified as the spilling type. Figures B-6, B-7 and B-8 show the variation of incident wave amplitude, reflected wave amplitude and reflection coefficient, obtained from temporal analysis (Section 2.2.1) and spatial analysis (Section 2.2.2), respectively.

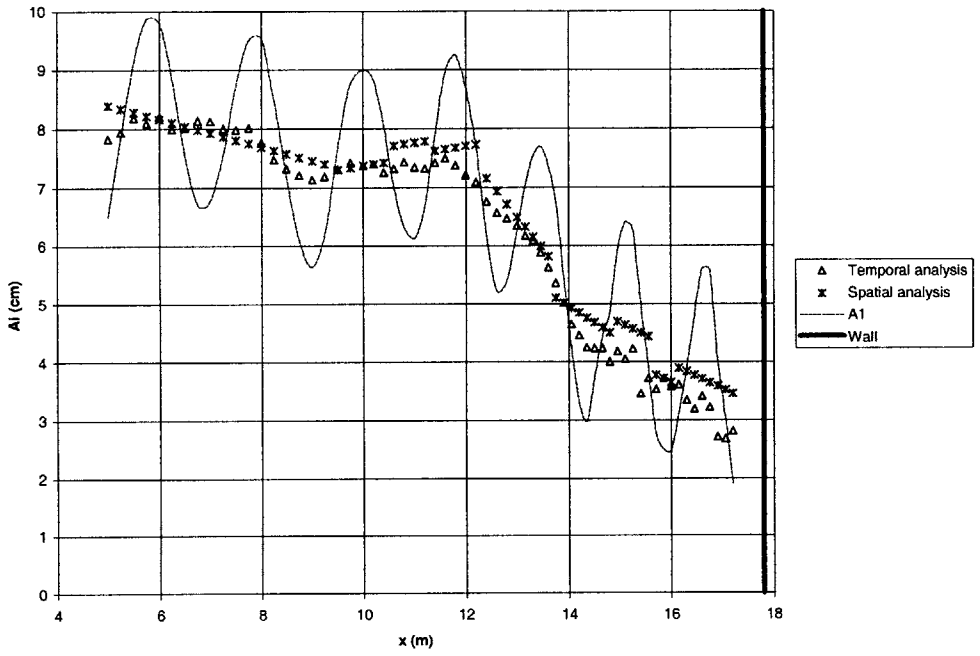

Figure B-6 Cross-shore variation of incident wave amplitude

Still, the temporal and spatial analyses give results in close agreement for A_i, A_r and R. The incident wave amplitude A_i decays in the constant depth region, then increases on

the slope, drops dramatically after breaking up to x = 14 m followed by a gentle decay. The still water depth is 14.4 cm at the last antinode of the measurement (x = 16.6 m), corresponding to a beat length of 1.28 m given the wave period of 2.07 s. The still water depth at the seawall (x = 17.8 m) is 11.1 cm which corresponds to a beat length of 0.86 m. Therefore, the next antinode following the one at x = 16.6 m should be located between x = 17.46 m and x = 17.88 m, which is in good agreement with the anticipation that an antinode should be located at the seawall (x = 17.8 m).

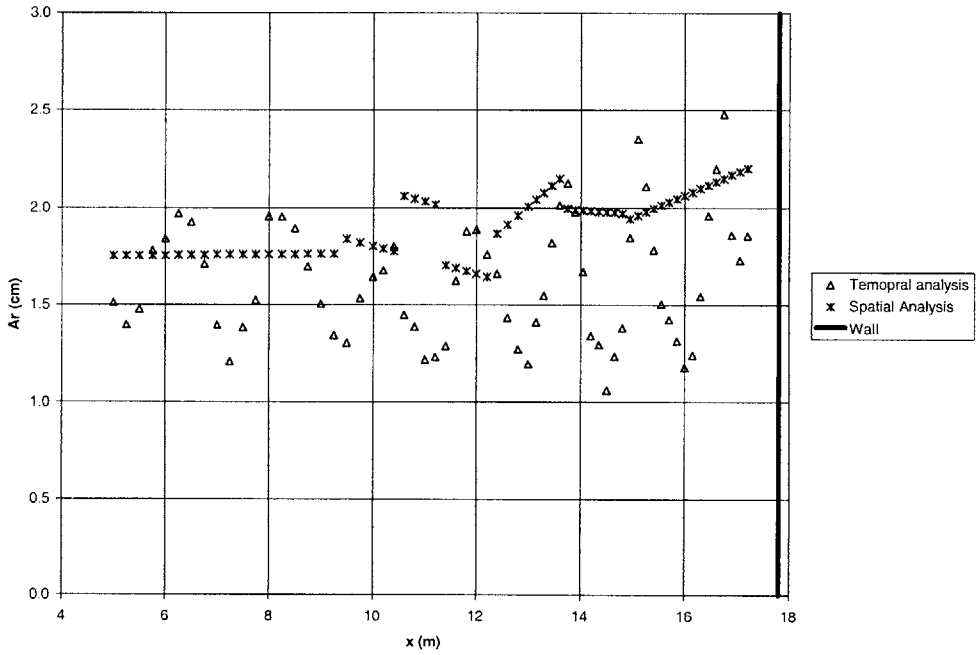

Figure B-7 Cross-shore variation of reflected wave amplitude

The reflected wave amplitude A_r varies from 1.2 cm to 2.0 cm in the constant depth region, and the average tends to increase on the slope. The reflection coefficient increases beyond the break point, reaching about 0.66 at x = 17.2 m. The increase in reflection coefficient is largely due to the dramatic drop of incident wave height beyond the break point, as seen in Figure B-1, and the near-constancy of the reflected wave amplitude,

shown in Figure B-2. In Figure B-2, the last antinode of the measurement is located at x = 16.75 m, 1.05 m away from the seawall. This value is in general agreement with the beat length (0.86 m) at the seawall, as discussed previously in this section.

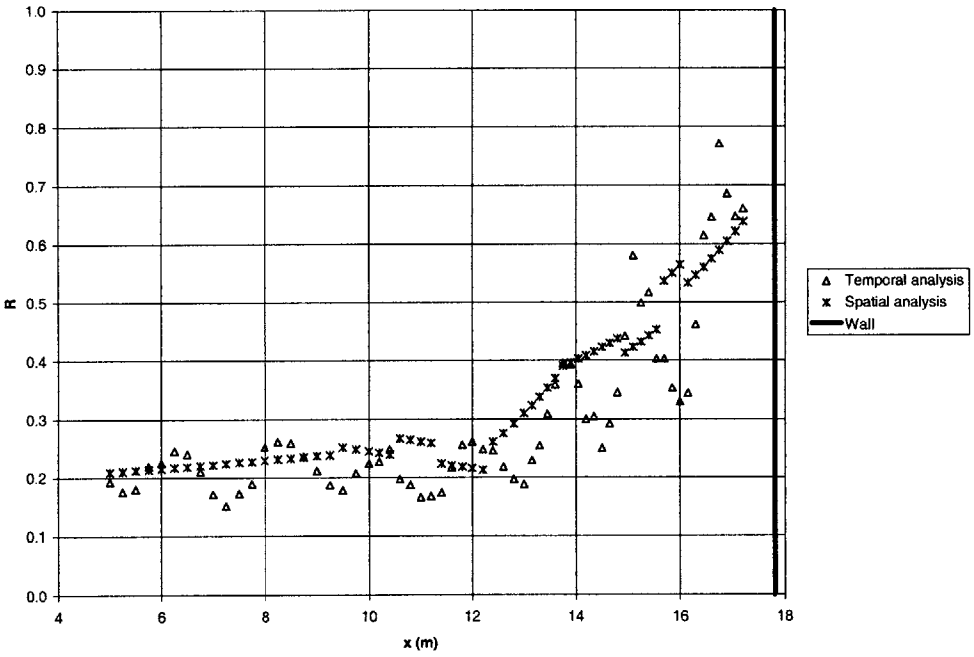

Figure B-8 Cross-shore variation of reflection coefficient

Figure B-9 shows the variation of the first harmonic incident wave height H_{i1} (denoted by circles), along with the still water depth h (denoted by squares) and still water depth plus set-up $h_+ = h + A_0$ (denoted by triangles). The full symbols are the values well beyond the break point (x > 14.5 m) and the straight lines are the linear best fit to these values. The still water level intersects the beach at x = 21.71 m with R^2 = 0.998. The intersections of the mean water level and the incident wave height with be beach are located at x = 23.06 m (R^2 = 0.992) and x = 22.21 m (R^2 = 0.872), respectively. The

"rule" is still reasonable that the wave height varies linearly with water depth beyond breaking.

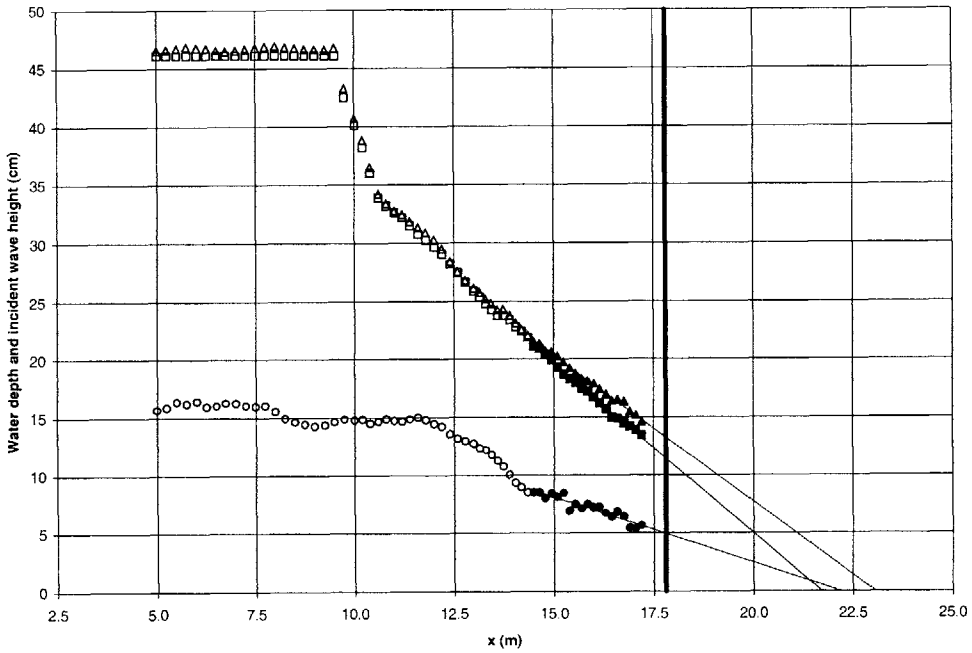

Figure B-9 Variation of water depth and incident wave height

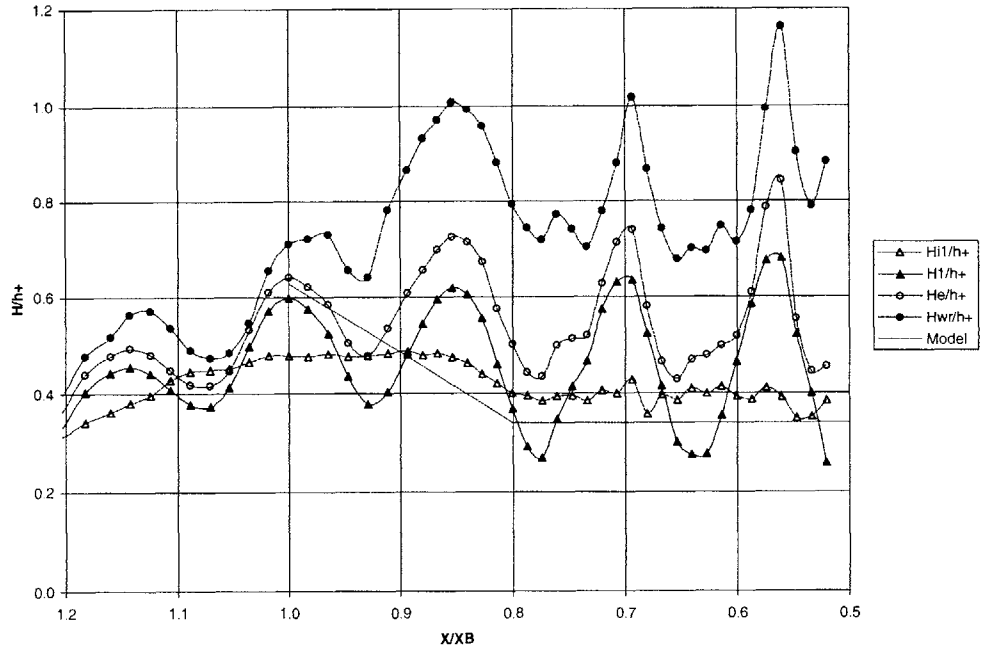

Figure B-10 Variation of wave height non-dimensionalized by total water depth h_+

In Figure B-10, we establish a horizontal axis, "X", with zero at x = 23.06 m, the intersection of total water level and the beach, and positive direction seaward, i.e., $X = 23.06 - x$. The X-axis is then non-dimensionalized by the position of the visually observed breaking point X_B = 11.26 m. The total first harmonic wave height H_1, the energy wave height H_e, the record wave height H_{wr} normalized by total water depth and the incident wave energy dissipation model are plotted in Figure B-10 for comparison.

All the H/h_+ curves exhibit organized waviness. It is noticed that the waves broke at x = 11.8 m, an antinode, which is in agreement with visual observation. At the break point, $(H_{wr}/h_+)_B$ (subscript "B" denoting breaking point) gives a maximum value of 0.71, whereas $(H_e/h_+)_B$, $(H_1/h_+)_B$ and $(H_{i1}/h_+)_B$ are 0.64, 0.60 and 0.48, respectively. However, when the average of high value at breaking and the subsequent low value is taken, $(H_{wr}/h_+)_B$, $(H_e/h_+)_B$, $(H_1/h_+)_B$ and $(H_{i1}/h_+)_B$ give 0.69, 0.56, 0.49 and 0.48, respectively, close to the results (except for $(H_{wr}/h_+)_B$) obtained from the no-structure experiments in which $(H_{wr}/h_+)_B$ = 0.85, $(H_e/h_+)_B$ = 0.61, $(H_1/h_+)_B$ = 0.49 and $(H_{i1}/h_+)_B$ = 0.48. The average lines of all H/h_+ curves start to decay beyond breaking and remain essentially constant with $(H_{i1}/h_+)_{B+}$ = 0.39, $(H_1/h_+)_{B+}$ = 0.42, $(H_e/h_+)_{B+}$ = 0.55 and $(H_{wr}/h_+)_{B+}$ = 0.80 where the subscript "B+" denotes the data well beyond breaking, i.e., $X/X_B < 0.75$. $(H_{i1}/h_+)_{B+}$ and $(H_1/h_+)_{B+}$ are close to the no-structure experimental results in which $(H_{i1}/h_+)_{B+}$ = 0.36 and $(H_1/h_+)_{B+}$ = 0.44, whereas

$(H_e / h_+)_{B+}$ and $(H_{wr} / h_+)_{B+}$ appear to be higher with $(H_e / h_+)_{B+}$ = 0.44 and $(H_{wr} / h_+)_{B+}$ = 0.56 in the no-structure experiments.

Again, the incident wave energy dissipation model is in general agreement with the measurements.

Appendix C

Sloping-wall Experimental Results with Shallower Water Depth in the Constant Depth Region

C.1 Overview of experiments

A sloping-wall experiment with shallower water depth (38.6 cm) in the constant depth region was conducted. The wave maker was run 10 minutes in order for stationarity to be established before measurements were taken. The wave period was 2.05 seconds and the waves broke visually at x = 10.8 m and the breakers can be classified as the spilling type. A three-minute record of both water surface displacement and velocity was taken at 67 locations from x = 5.0 to x = 17.65 m. The measuring interval in the constant depth region was 25 cm, while it shortened to 20 cm on the slope, and 15 cm near the toe of the seawall, respectively. The experimental results are shown in the following section.

C.2 Experimental results

Figure C-1 shows the wave records and frequency spectra from x = 12.0 m, within breaking zone. It is noticed that the surface displacement and horizontal records are still periodic even after breaking and the first harmonic is dominant over higher harmonics.

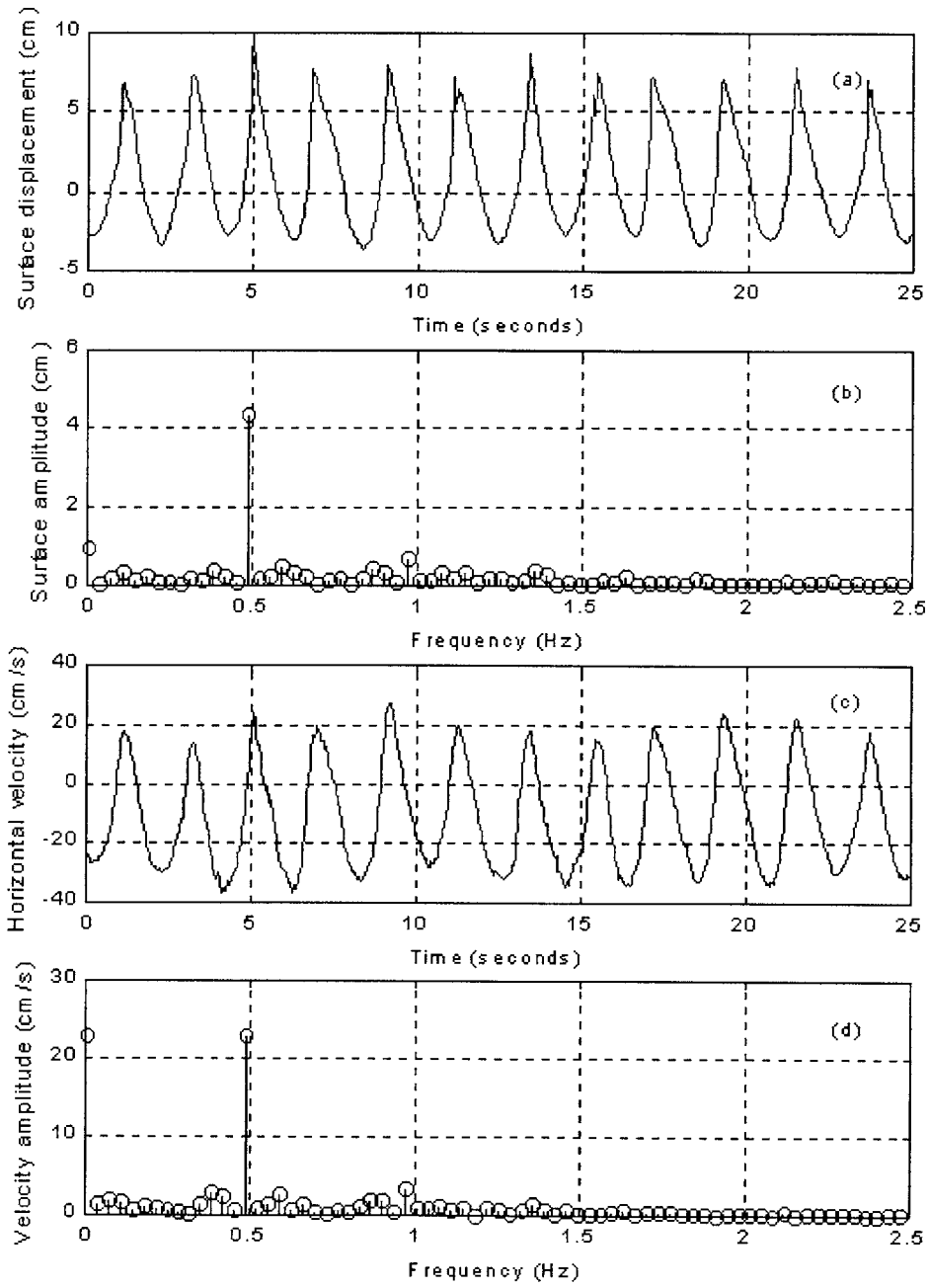

Figure C-1 Wave records and frequency spectra at x = 12.0 m; (a) surface displacement record; (b) surface displacement spectra; (c) horizontal velocity record; (d) horizontal velocity spectra. Note: only first 72 points are shown in the frequency spectra.

Figure C-2 shows the variation of first harmonic total wave amplitude and first harmonic incident wave amplitude obtained from temporal analysis (Section 2.2.1). For comparison the predicted incident wave amplitude accounting for shoaling with a_{ic} = 7.13 cm (average of resolved incident wave amplitude within the beat length from x = 7.25 m to x = 8.75 m) in the constant depth region is also shown in Figure C-2. Note that the sloping line (denoted by "Wall") does not signify the actual sloping wall and only the starting point at x = 17.8 m signifies the toe of the sloping wall. Because the shallower water depth in the surf zone reached the measuring limit of ADV, only surface displacement was measured beyond x = 12.0 m, where A_{i1} ends in Figure C-2. As the seawall is located well beyond the surf zone, a small reflection is expected.

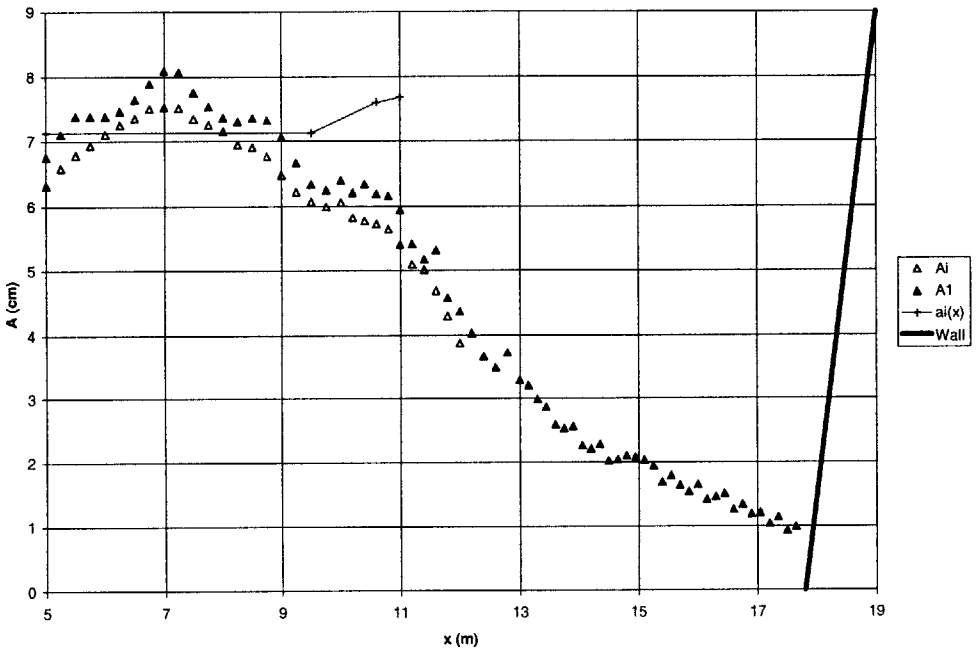

Figure C-2 Variation of first harmonic total and incident wave amplitudes

A_{i1} is very close to A_1, indicating that the reflected waves are small. It is noticed that there is a sharp decay around x = 11.0 m, in agreement with the visually observed break point. Again, a gentle decay (x > 13.0 m) follows the sharp decay (from x = 11.0 m to x = 13.0 m).

The first harmonic reflected wave amplitude and reflection coefficient obtained from the temporal analysis (Section 2.2.1) are shown in Figures C-3 and C-4, respectively.

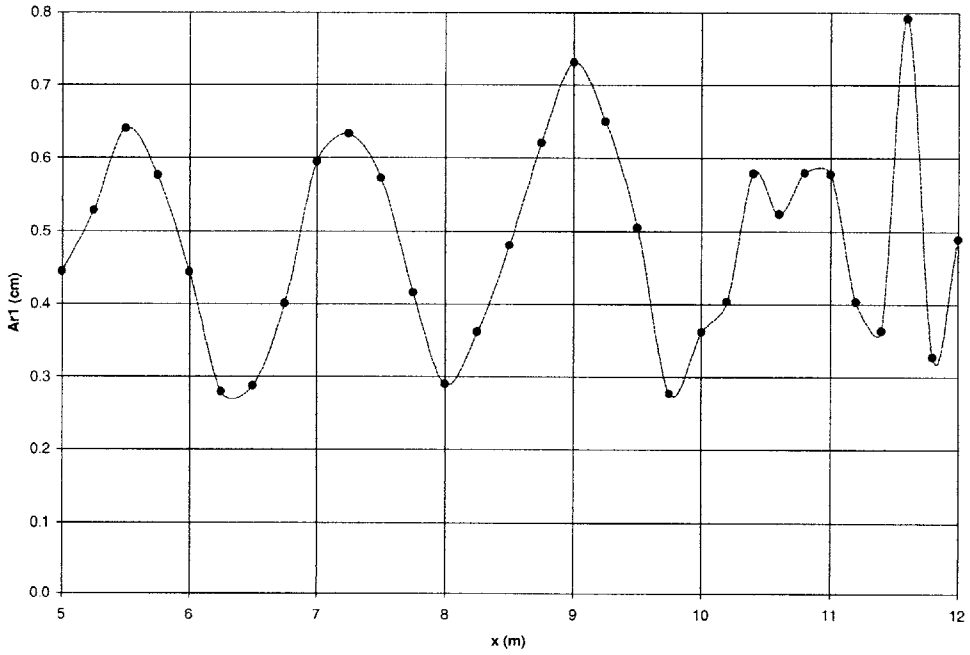

Figure C-3 Variation of reflected wave amplitude

The reflected wave amplitude and reflection coefficient show organized waviness (see dotted lines) from the constant depth region to the break up. The reflected wave amplitude is about 0.45 cm in the constant depth region, so with the incident wave amplitude of about 7 cm, the reflection coefficient is about 0.64, which as anticipated is

very small. Seen from Figure C-4, the constant depth region's reflection coefficient is about 0.06, in agreement with the estimation.

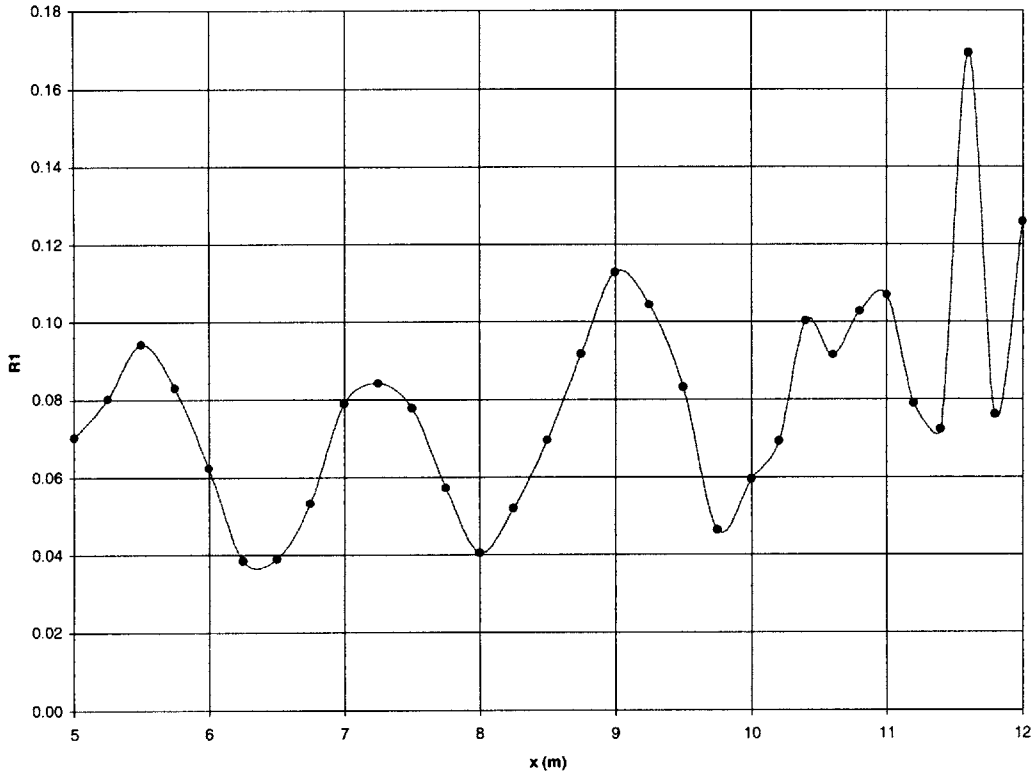

Figure C-4 Variation of reflection coefficient

Figure C-5 shows the variation of still water depth h (squares), total water depth h_+ (triangles) and first harmonic total wave height H_1. The full symbols in the figure stand for the data well beyond the surf zone, i.e., $x > 13$ m and the straight lines are the linear best fit to these values. The incident wave height H_{i1} (total wave height H_1 used instead) is not presented in the figure as in the previous chapters since the incident wave height measurement ends at 12.0 m and H_1 is fairly close to H_{i1}.

The still water level intersects the beach at x = 18.95 m with R^2 = 0.998. The intersections of the mean water level and the total wave height with be beach are located at x = 20.49 m (R^2 = 0.995) and x = 19.53 m (R^2 = 0.954), respectively. The "rule" is still reasonable that the wave height varies linearly with water depth beyond breaking.

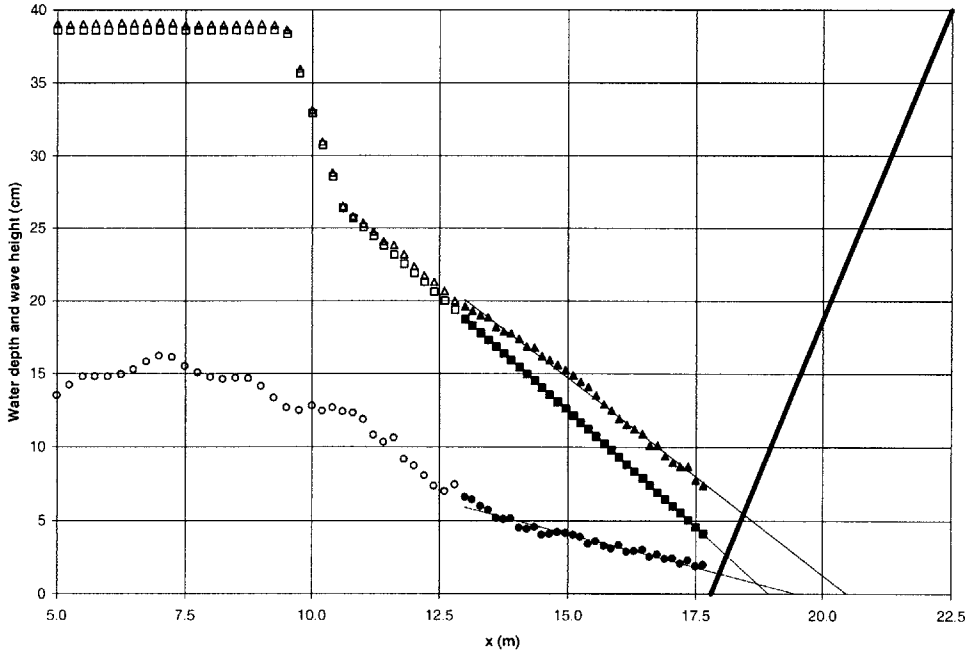

Figure C-5 Variation of water depth and first harmonic total wave amplitude. Note: the slope of the wall is not scaled.

In Figure C-6, we establish a horizontal axis, "X", with zero at x = 20.49 m, the intersection of mean water level and the beach, and positive direction seaward, i.e., $X = 20.49 - x$. The X-axis is then non-dimensionalized by the position of the visually observed breaking point X_B = 9.69 m (x_B = 10.8 m). The total first harmonic wave height $H_1 = 2A_1$ and the first harmonic incident wave height $H_{i1} = 2A_{i1}$ normalized by

the total water depth h_+, and the incident wave energy dissipation model are plotted in Figure C-6 for comparison.

It is obvious that both H_1/h_+ and H_{i1}/h_+ climb to maxima as the visually observed break point is approached. The values of H/h_+ in the vicinity of the break point are of definite interest. $(H_1/h_+)_B$ and $(H_{i1}/h_+)_B$ (subscript "B" denoting the break point) give 0.48 and 0.44, respectively. After the break point, H_1/h_+ drops dramatically and then remains approximately constant at a value of $H_1/h_+ \cong 0.26$. The behavior of the H_1/h_+ after break point is similar to our model of incident wave energy dissipation, but the initial decay distance and the constant well beyond the surf zone are not in agreement, which needs further investigation.

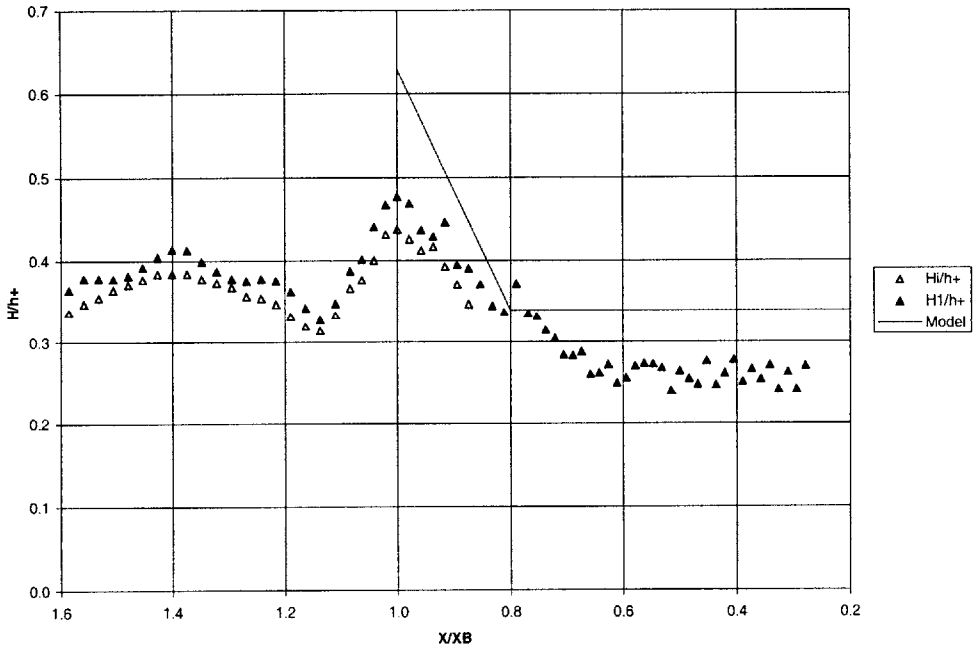

Figure C-6 Variation of wave height non-dimensionalized by total water depth h_+

Appendix D

Application of the Model

The model proposed in Chapter 6 is applied to the five experiments presented in the Chapters 4, 5, Appendices B and C, respectively, and the results are presented in the following sections.

D.1 Vertical-wall experiment with higher wave height

In the vertical-wall experiment discussed in Chapter 4, the still water depth in the constant depth region is 46 cm, wave period is 2.03 seconds and the incident wave height is about 19 cm. Given these initial conditions, the break point is predicted to be located at x = 11.2 m, in fair agreement with the observed break point (x = 11.8 m). The gentle decay of the incident wave height is predicted to start from x = 13.1 m. The predicted incident wave height at the wall (x = 17.8 m) is 4.98 cm so the reflected wave height at the structure is 0.7×4.98 = 3.49 cm. The wave number k is taken as the average within a beat length. Figure D-1 shows the variation of the predicted wave amplitude. For comparison, the measured first harmonic total wave amplitude A_1, the energy amplitude A_e and the record wave amplitude A_{wr} are also shown in the figure. Figure D-2 shows the variation of predicted near-bottom orbital velocity. For comparison, the measured first

harmonic total horizontal velocity U_{1bm}, the energy horizontal velocity amplitude U_{ebm} and the record horizontal velocity U_{wrbm} are also shown in the figure.

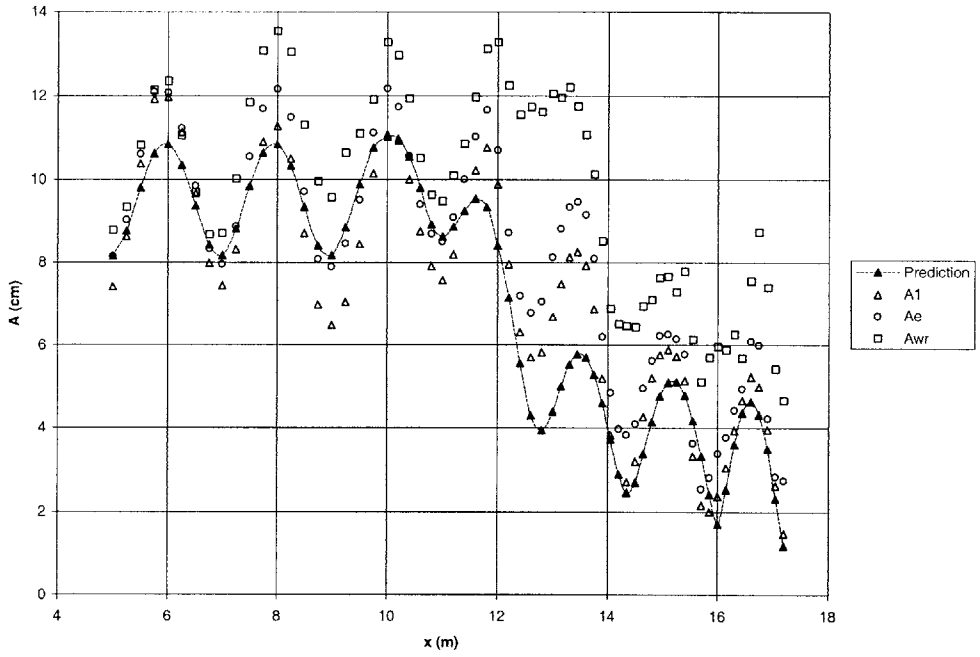

Figure D-1 Predicted wave amplitude

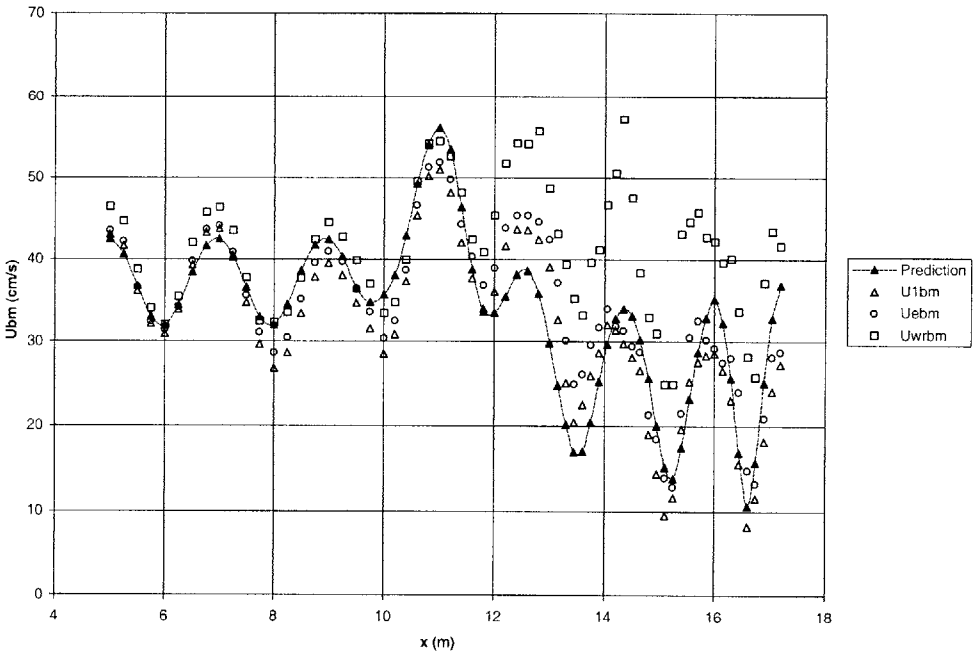

Figure D-2 Predicted near-bottom orbital horizontal velocity

Seen from Figures D-1 and D-2, the predicted wave amplitude and the near-bottom orbital velocity are in reasonably close agreement with the measurements, in particular the locations of the nodes and the antinodes.

D.2 Vertical-wall experiment #1 with lower wave height

In the vertical-wall experiment #1 presented in the Appendix B, the still water depth in the constant depth region is 47.7 cm, wave period is 2.03 s and the incident wave height is about 14.7 cm. Given these initial conditions, the break point is predicted to be located at x = 13.7 m, which is somewhat different than the observed break point (x = 12 m). The gentle decay of the incident wave height is predicted to start from x = 15.2 m. The predicted incident wave height at the wall (x = 17.8 m) is 5.05 cm so the reflected wave height at the structure is 0.7×5.05 = 3.54 cm.

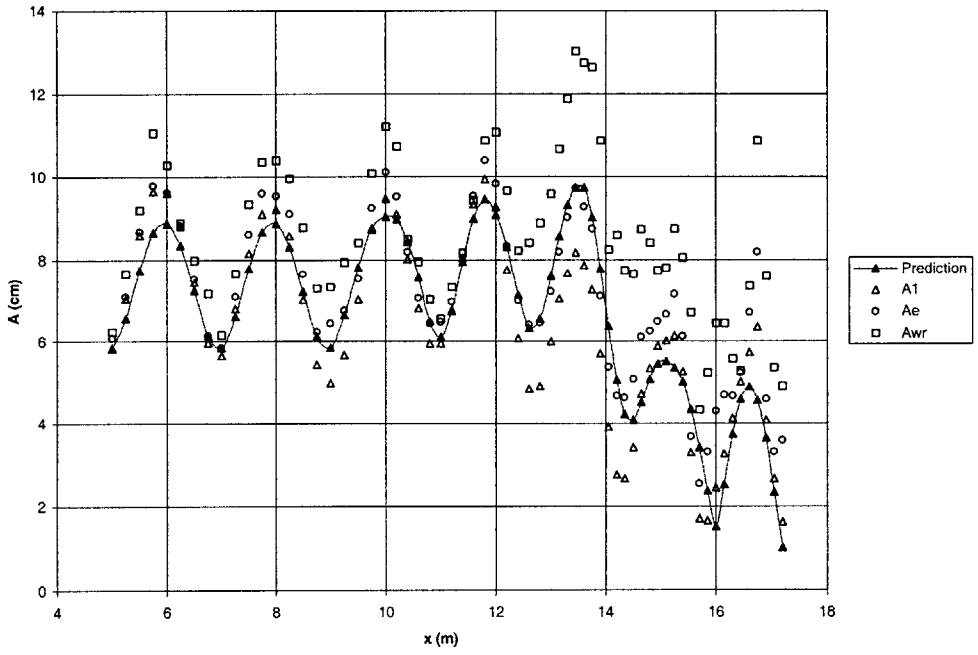

Figure D-3 Predicted wave amplitude

Figures D-3 and D-4 show the variation of the predicted wave amplitude and the predicted near-bottom orbital velocity, respectively, with the same symbols used in section D.1.

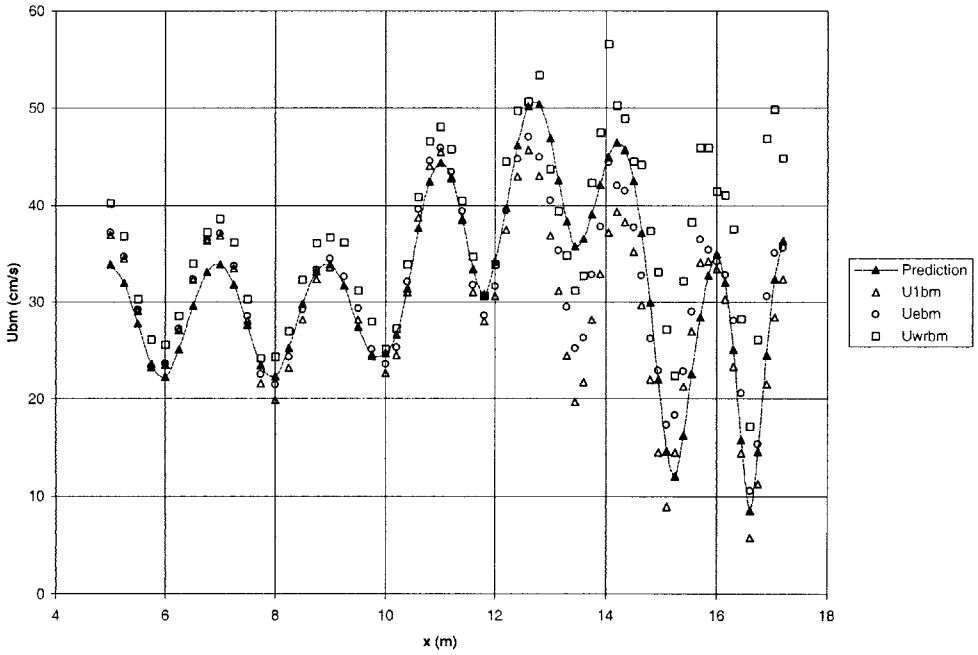

Figure D-4 Predicted near-bottom orbital horizontal velocity

Again, the predicted wave amplitude and the near-bottom orbital velocity are in reasonably close agreement with the measurements, in particular the locations of the nodes and the antinodes.

D.3 Vertical-wall experiment #2 with lower wave height

In the vertical-wall experiment #2 presented in the Appendix B, the still water depth in the constant depth region is 46.1 cm, wave period is 2.07 s and the incident wave height is about 16 cm. Given these initial conditions, the break point is predicted to be located at

x = 12.6 m, in fair agreement with the observed break point (x = 11.8 m). The gentle decay of the incident wave height is predicted to start from x = 14.2 m. The predicted incident wave height at the wall (x = 17.8 m) is 4.73 cm so the reflection coefficient of the structure is 0.7×4.73 = 3.31 cm.

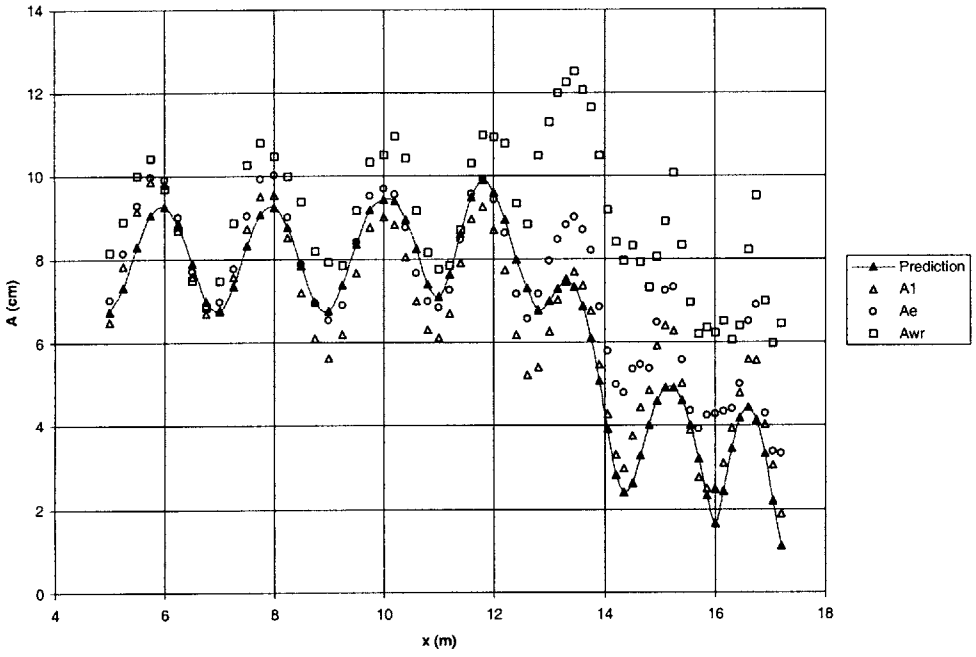

Figure D-5 Predicted wave amplitude

Figures D-5 and D-6 show the variation of the predicted wave amplitude and the predicted near-bottom orbital velocity, respectively, with the same symbols used in section D.1. Still, the predicted wave amplitude and the near-bottom orbital velocity are in reasonably close agreement with the measurements, in particular the locations of the nodes and the antinodes.

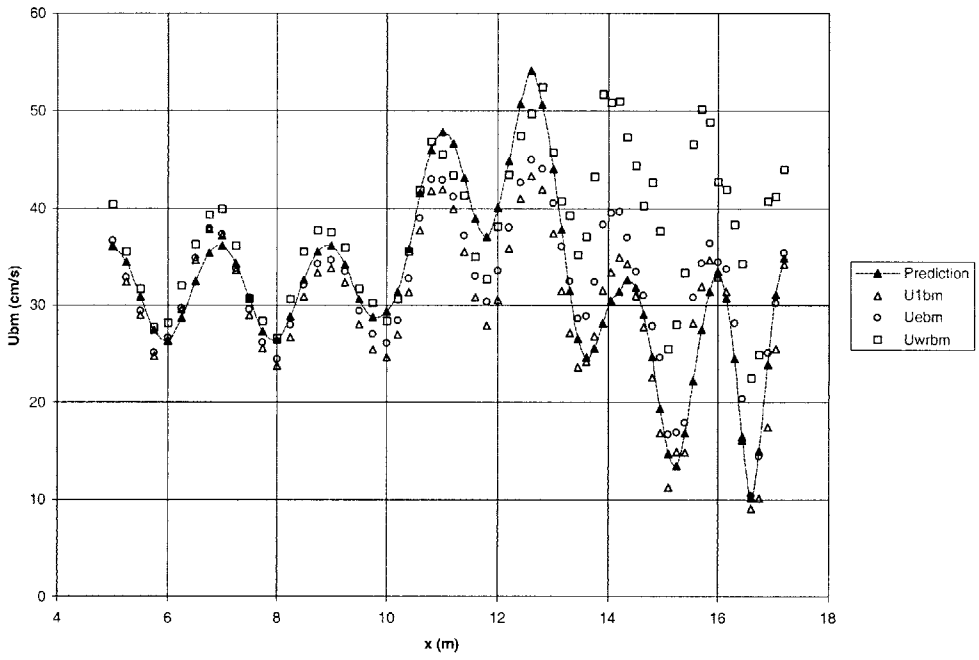

Figure D-6 Predicted near-bottom orbital horizontal velocity

D.4 Sloping-wall experiment with deeper water depth

In the sloping-wall experiment presented in Chapter 5, the still water depth in the constant depth region is 50 cm, wave period is 2.05 s and the incident wave height is about 18.6 cm. Given these initial conditions, the break point is predicted to be located at x = 12.5 m, in fair agreement with the observed break point (x = 11.8 m). The gentle decay of the incident wave height is predicted to start from x = 14.4 m. The predicted incident wave height at the wall (x = 17.8 m) is 6.1 cm so the reflection coefficient of the structure is 0.8×6.1 = 4.88 cm. Figures D-7 and D-8 show the variation of the predicted wave amplitude and the predicted near-bottom orbital velocity, respectively, with the same symbols used in section D.1.

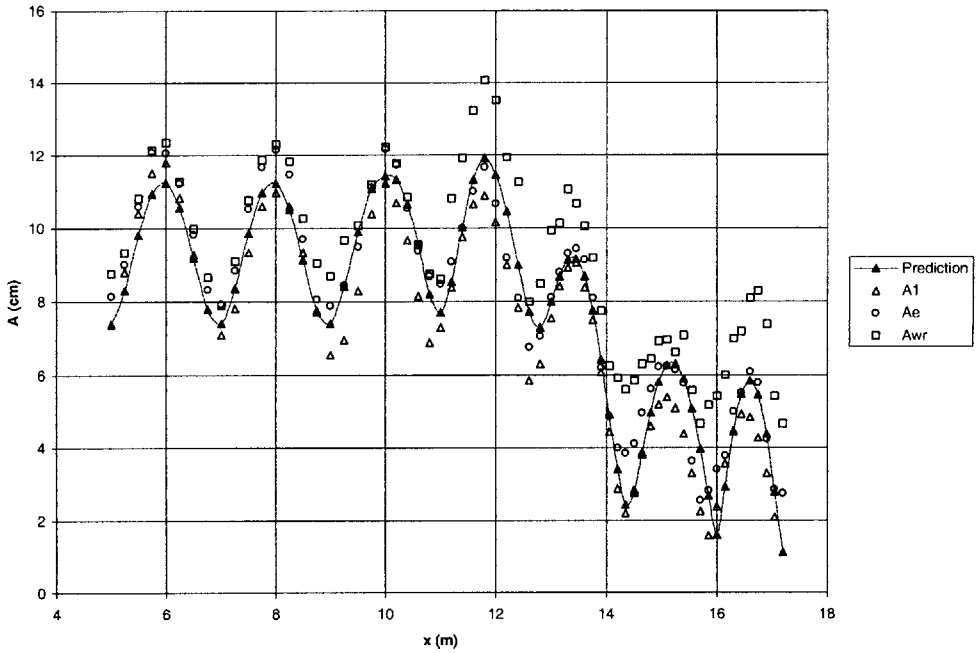

Figure D-7 Predicted wave amplitude

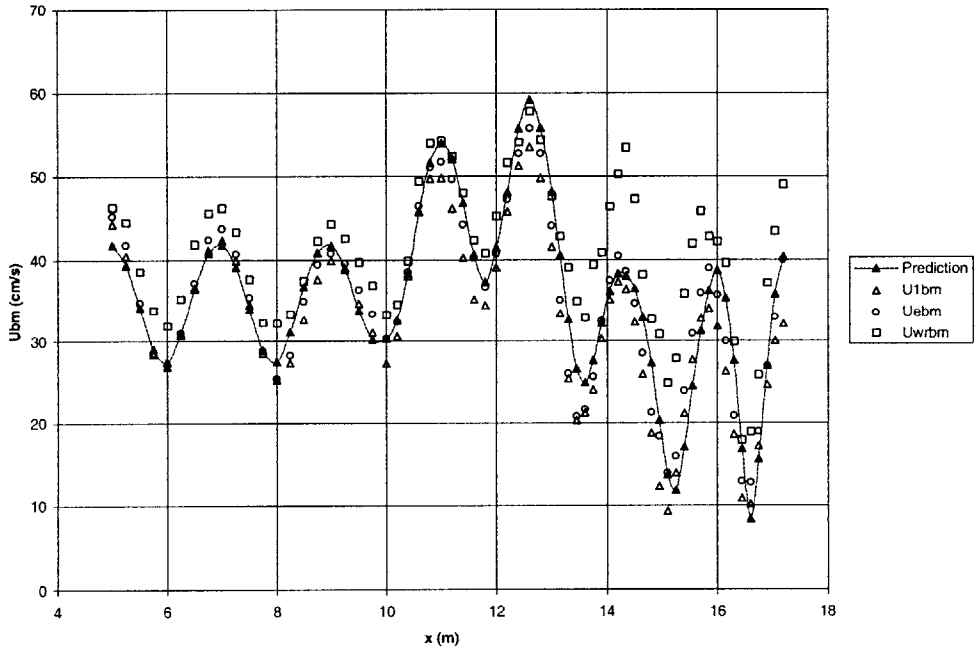

Figure D-8 Predicted near-bottom orbital horizontal velocity

Still, the predicted wave amplitude and the near-bottom orbital velocity are in close agreement with the measurements, in particular the locations of the nodes and the antinodes.

D.5 Sloping-wall experiment with shallower water depth

In the sloping-wall experiment presented in Appendix C, the still water depth in the constant depth region is 38.6 cm, wave period is 2.03 s and the incident wave height is about 14.3 cm. Given these initial conditions, the break point is predicted to be located at x = 11.2 m, in fair agreement with the observed break point (x = 10.8 m). The gentle decay of the incident wave height is predicted to start from x = 12.6 m. The predicted incident wave height at the wall (x = 17.8 m) is 2.5 cm so the reflection coefficient of the structure is 0.8×2.5 = 2.0 cm.

Figure D-9 shows the variation of the predicted wave amplitude with the same symbols used in section D.1. The orbital velocity is not shown as in previous sections because the velocity measurement ended right after the breakpoint due to the shallow water depth. The predicted wave amplitude does not agree well with the measurements, especially when we get well into the surf zone. Within the surf zone, the predicted wave amplitude shows clear waviness whereas this is not seen in the measurements. It is noticed that the predicted wave height is 3.3 cm when it is close to the structure, whereas measurements suggest an energy wave height of 1.1 cm at x = 17.65 m, immediately in front of the seawall. It is therefore likely that this difference is caused by the extremely small wave height of the incident waves when they reach the structure.

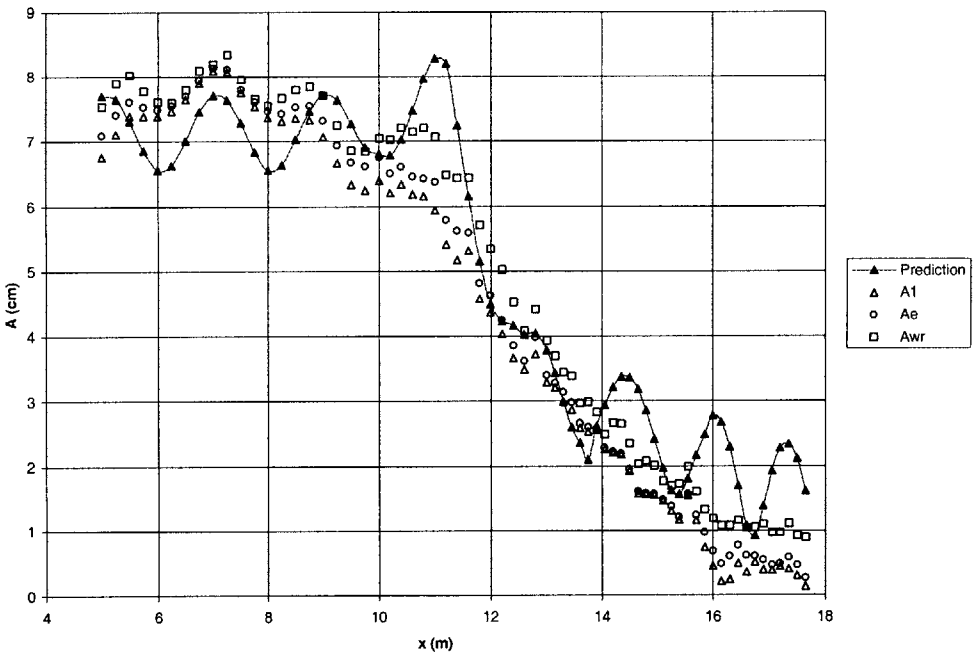

Figure D-9 Predicted wave amplitude